UNIVERSITÉ PAUL VERLAINE-METZ   NORTHEASTERN UNIVERSITY

DISSERTATION

To be presented at
University of Paul Verlaine-Metz and Northeastern University

LI Song

To obtain the doctor's degree of

University of Paul Verlaine-Metz and Northeastern University

SPECIAL FIELD: Materials Science
OPTION: Physics

Structural Design, Characterization, and Property Investigation of Iron Oxide

Nanoparticles with Visible Light Photoactivity

To be defended on August 14th, 2009 in front of the jury:

P. Raveendran	Professor	Indian Institute of Technology, India	Reviewer
C. Esling	Professor	University of Paul Verlaine-Metz	Supervisor
L. Zuo	Professor	Northeastern University, Shenyang	Supervisor
G. W. Qin	Professor	Northeastern University, Shenyang	Co-Supervisor
Y. Zhang	Doctor Phil	University of Paul Verlaine-Metz	Co-Supervisor
I. Morelon	Doctor Phil	Science and technology Attaché French Embassy in China, Beijing	Jury member
X. D. Sun	Professor	Northeastern University, Shenyang	Reviewer, Jury member
X. Zhao	Professor	Northeastern University, Shenyang	Jury member

Abstract

Global environmental pollution and energy issue are considered as two greatest challenges that human society is facing now. Semiconductor photocatalysis is expected as a highly promising strategy for both harvesting solar energy and decomposing unwanted organics in water and air by solar light irradiation. The main problem of TiO_2, the most widely studied photocatalyst material by now, is that its band gap is as wide as 3.1 eV, making it absorb only the UV part of the incident solar irradiation. Iron oxide has a proper band gap of about 2.1 eV which lies in the visible region of solar spectrum and allows utilization of 45% of the solar radiation. Together with the environmental compatibility and low cost, iron oxide is considered as a good candidate for visible light photocatalyst. For the purpose of exploiting iron oxide as effective photocatalyst, we have prepared iron oxide nanoparticles of various shapes and investigated their photocatalytic activities.

The objective of the present dissertation is to develop and characterize iron oxide photocatalyst which is highly responsive to visible light. Nanostructured iron oxide and oxyhydroxide nanoparticles with various morphologies were designed and synthesized *via* hydrothermal route. Stabilizer molecules with different capping groups were applied in the reaction system to control the morphology of the final products. The effects attributed to the interaction between capping groups of stabilizer molecules and iron oxide surfaces. To elucidate the growth mechanism of iron oxide particles, a TEM based trace method was proposed to characterize the crystalline planes and directions of a faceted nanoparticle, and therefore its shape. The Miller indices of surface planes can be determined through coordinate transformation after the determination of the edge vectors in the TEM screen coordinate system.

Methyl orange, a representative azo dye pollutant in textile industry, was chosen as the model contaminant molecule to evaluate the photocatalytic performance of the obtained powders. A systematic study, including the influence of the reaction conditions, the kinetics and the route of the oxidation of the methyl orange molecules, was carried out to explore the mechanism of photocatalytic degradation of organic molecules over iron oxide under visible light irradiation. It was found that the photodegradation of methyl orange over iron oxide was more like a semiconductor photocatalysis process, rather than a surface reaction process of ligands to metal charge transfer. Moreover, the visible light photocatalytic activities of iron oxide can be tuned by controlling the morphologies, especially the crystallographic facet of the iron oxide nanoparticles.

I

Post-treatment techniques were adopted to enhance the ability of iron oxide photocatalyst to decompose organic pollutant molecules. The iron oxide nanopowders were modified by loading noble metals, such as Ag and Au nanoparticles. Photocatalytic experimental results showed that the abilities of loaded metal particles to inhibit the electron-hole pair recombination depend on the relative positions between their work functions and conductive band position of the iron oxide. To overcome the problem caused by the short free distance of charge carriers inside iron oxide, nanorod arrays of iron oxide were prepared. The results show that the photocatalytic activity of iron oxides can be improved by microstructure optimization and surface modification.

Keywords: iron oxide nanostructures; morphology control; TEM characterization; photocatalysis

Résumé

La pollution de l'environnement et l'insuffisance des ressources énergétiques dans le monde constituent deux défis majeurs auxquels l'humanité est confrontée aujourd'hui. La photocatalyse hétérogène de semiconducteur est considérée comme une stratégie prometteuse pour la collecte de l'énergie solaire et la décomposition de contaminants organique dans l'eau et l'air. TiO_2 est aujourd'hui le photocatalyseur le plus largement utilisé. Cependant, TiO_2 est un semi-conducteur avec une bande interdite d'environ 3.1eV. Donc, il n'absorbe pas la lumière visible. L'oxyde de fer est un bon candidat potentiel pour la photocatalyse: ce matériau est stable, moins cher, respecte l'environnement et il a une bande interdite suffisamment petite (2.1 eV) pour absorber 45% de la radiation solaire incidente. Afin de développer un photocatalyseur efficace de l'oxyde de fer, nous avons préparé des nanoparticules d'oxyde de fer de formes différentes et étudié l'influence des différents paramètres expérimentaux.

L'objectif cette thèse est de développer et de caractériser un photocatalyseur à base d'oxyde de fer et hautement photoréactive capable de décomposer les molécules des polluants organiques. Des nanoparticules d'oxydes et d'oxyhydroxyde de fer avec différentes morphologies ont été conçues et synthétisées par la méthode hydrothermale. Dans le système de réaction, des agents de surface avec différents groupes fonctionnels ont été utilisés pour la contrôle de la morphologie. Les effets ont été attribués à l'interaction entre les groupes fonctionnels des agents de surface et des surfaces d'oxyde de fer. Pour élucider les mécanismes de croissance de nanoparticules d'oxyde de fer, une technique en MET basée sur une méthode de trace a été proposée afin de caractériser les plans cristallins et l'orientation de nanoparticules facetteés, et donc leurs formes. Les indices de Miller de plans de surface peuvent être déterminé par la transformation de coordonnées après la détermination du vecteur des bords dans les systèmes de coordonnées de l'écran du MET.

Dans ce travail, l'orange de méthyl, un représentant colorant azoïque de l'industrie textile, a été pris comme molécule modèle pour les contaminants organiques pour évaluer les capacités photocatalytiques des poudres obtenues. Une étude systématique, y compris l'influence des conditions de réaction et la cinétique, a été effectuée pour étudier le mécanisme de la dégradation photocatalytique de méthylorange à l'oxyde de fer sous irradiation de lumière visible. Il a été constaté que la photodégradation de l'orange de méthyle à l'oxyde de fer est un procédé de photocatalyse de semiconducteur. De plus, les activités photocatalytiques des

lumières visibles d'oxyde de fer peuvent être harmonisées par le contrôle des morphologies, surtout les indices des facettes des nanoparticules d'oxyde de fer.

Les techniques de traitement postérieur ont été utilisées à améliorer la capacité photocatalytique de l'oxyde de fer pour décomposer les molécules des contaminants organiques. Les nanopoudres d'oxyde de fer ont été modifiées par intégration de métaux nobles, par exemple les nanoparticules d'Ag et d'Au. Les résultats des exprimentations photocatalytiques montrent que la capacité des particules métalliques intégrées d'inhiber la récombination de la paire de trou électrique dépendent de la position relative entre fonctions travail et la position de la bande de conduction de l'oxyde de fer. Pour surmonter ce problème causé par la courte distance libre des charge dans l'oxyde de fer, des nanobâtonnets ont été préparés. Les résultats indiquent que l'activité photocatalytique de l'oxyde de fer peut être améliorée par l'optimisation microstructurale et la modification surfacique.

Mots-clés: nanostructures d'oxyde de fer; contrôle de la morphologie; caractérisation par MET; photocatalyse

摘　要

环境污染治理和能源短缺是人类社会当前面临的两大挑战。半导体光催化技术可利用太阳能将有机污染物矿化为无机小分子，是一种极具潜力的环境深度修复技术。当前研究最为充分的光催化剂 TiO_2 的瓶颈问题在于禁带宽度宽(3.1 eV)，只能利用太阳辐射中能量不到 4%的紫外光。开发能够利用可见光的催化剂对于环境修复、太阳能制氢、DSSC 电池开发等具有重要意义。窄禁带半导体氧化铁的带隙在 2.1 eV 左右，能吸收利用占太阳辐射能量 45%左右的紫外-可见光。加上具有环境友好、廉价、在碱性环境中化学稳定性好等优点，是一种有广泛应用前景的光催化剂材料。

本论文的目的是开发和表征基于氧化铁半导体的高活性可见光光催化剂，并通过研究氧化铁催化降解偶氮染料分子的机理，利用一系列物理化学手段延长氧化铁光生载流子的寿命，提高光催化活性。首先采用水热法制备了不同形貌的氧化铁纳米粒子，考察了带有不同官能团的包裹剂分子对氧化铁在溶液中生长过程和形貌的影响。基于 TEM 衍射和图像系统，提出了规则截面形貌粒子外表面晶体学指数的表征方法，并利用该方法研究了制备氧化铁的形貌。并基于表征结果提出了截面规则形貌氧化铁纳米粒子的台阶生长机制。

以偶氮染料分子甲基橙为模型研究了氧化铁光催化降解有机分子的反应路径、动力学特征、影响因素。通过对氧化铁光催化机理的研究发现其降解有机物机理基于半导体光催化，而不是争议中的表面配体反应过程。另外还发现通过控制形貌制备不同外表面晶体学指数的氧化铁，可以改进其光量子效率。

基于对氧化铁光催化机理的认识，提出了提高其光催化效率的改性手段。通过不同贵金属纳米粒子负载对氧化铁光催化活性的影响，发现贵金属影响与金属的功函数与氧化铁导带边缘位置有关，贵金属功函数越大，对催化活性的提高越有利。另外还为解决光催化剂的回收问题，还开发了一种可以在玻璃基板上氧化铁纳米棒阵列结构的溶液方法，通过有机盐分解在基板上制备种晶层可以诱导氧化铁在溶液中的各向异性生长。

关键词：氧化铁纳米结构；形貌控制；TEM 表征；光催化

Contents

Chapter 1   Introduction

1.1   History and Current Status of Photocatalysis

Environmental pollution and energy shortage, being regarded as the top two challenges facing mankind in the next 50 years, have attracted much attention from both government agencies and scientific communities. Semiconductor based heterogeneous photocatalytic technology was developed as a promising solution to the two challenges. The utilization of semiconductors as photocatalyst started from the first report by Fujishima and Honda in 1972.[1] At that time, the energy crisis was spreading around the world, the reported water splitting into hydrogen and oxygen under ultraviolet (UV) irradiation by using TiO_2 photoanode inspired extensive research concerning solar energy conversion and created a new era in the field of photocatalysts. In 1977, Bard reported that CN^- was photocatalytically oxidized into OCN^- on TiO_2,[2] and the applications of photocatalysis were extended into the field of waste water treatment and environmental remediation. Since the beginning of the 1990s, environmental pollutants have aroused increased public concern. Heterogeneous photocatalytic reactions on *n*-type semiconductors are now recognized as an ideal technology for decomposing organic pollutants both in water and air.

TiO_2 has been the earliest and most extensively investigated material for photocatalytic and photoelectrochemical applications because of its excellent chemical stability and low cost.[3] It has been proven very effective in photodegradation of many contaminants in aqueous and gaseous phases, including dyes, surfactants, chlorinated hydrocarbons, nitro compounds, and aromatic hydrocarbons such as trichloroethylene, chloroform, and chlorophenol. Some other candidates as photocatalyst include ZnO and titanate. However, the common problem of these materials is that their band gaps are so wide that only the UV part of the solar spectrum can be absorbed. This means that only approximately 5% of the terrestrial solar energy [4] can be utilized for photocatalytic reactions. In addition, the size of photocatalyst particles is often on the nanoscale to increase the surface to volume ratio. In this case, blue-shift resulting from size reduction further reduces the solar light adsorption.

Attempts to shift light response region of TiO_2 and some other wide band gap semiconductors towards visible part of solar spectrum have been made to increase the light adsorption. Various strategies, such as ion doping, noble metal loading, dye sensitization and semicon-

ductor coupling, have been proposed to modify the band structure of TiO_2. Although the photocatalytic performance of TiO_2 has been improved to some extent by applying the above techniques, the photo quantum efficiency is still low and sometimes detrimental effects might be caused by the modification. For instance, N-doped TiO_2 photocatalysts are less stable though doping could possibly make TiO_2 respond to visible light.[5] Another example, although noble metal loading is regarded to be effective in separating the electron-hole pair, Kamat proved that the improvement only works in the initial several hours. The deposited metal clusters (Au, Pt, etc.) could be oxidized under irradiation and the photoresponse improvement of noble metals may get reduced.

An alternative approach to develop photocatalyst with high visible-light response is to start with a material that has an intrinsically small band gap. Two oxides, WO_3 and Fe_2O_3 are promising and have attracted much attention since they have proper band gap of 2.5 eV and 2.1 eV,[6] respectively, both lies in the visible region of solar spectrum. However, the disadvantages of WO_3 rely on its toxicity and low abundance in earth.

1.2   Principles of Semiconductor Photocatalysis

Many organic pollutants in waste water can be decomposed into simple molecules such as carbon dioxide and water by irradiation of sunlight. However, this natural purification process is normally so slow that a heavy burden may be caused for the earth environment. Colloidal semiconductors were used to accelerate the photo-decomposition process of pollutants. By custom, the process and the corresponding semiconductors used are called photocatalysis and photocatalysts, respectively.

1.2.1 Mechanism of Photodegradation of Organics by Semiconductor

Contact between a semiconductor and another phase (electrolyte, gas, or metal) generally leads to a redistribution of charge carriers and the formation of a double layer. Taking the *n*-type semiconductor immersed in electrolyte solution as an example, since the Fermi energy of *n*-type semiconductor is normally higher than the redox potential level of electrolyte, electrons will flow from the semiconductor until the equilibrium $E_F = E_{\text{redox}}$ is established.[7] As a consequence, the equalized-electron-energies charged layers are formed at the semiconductor-electrolyte interface, as shown in Figure 1.1. The electrical double layers positioned between the electrolyte and the surface of semiconductor with high electric field may trap the carrier and bend the band structure of semiconductor. Similar charged layers on the electrolyte side called *Helmholtz layer* and *Gouy-Chapman layer* are formed.
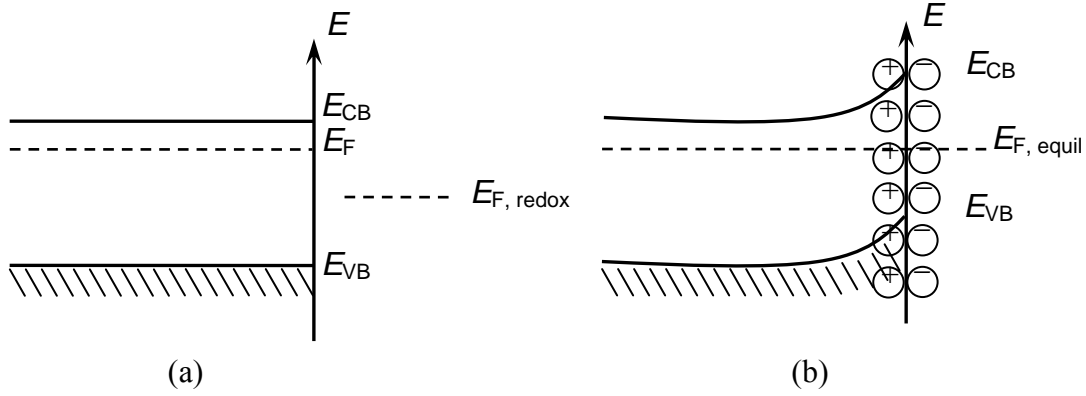
Figure 1.1 The *n*-type semiconductor-electrolyte interface (a) before and (b) after equilibration.[7]

When the semiconductor immersed in electrolyte absorbs impinging photons with energy equal to or higher than its band gap energy ($h\nu \geq E_g$), electrons are promoted into the semi-conductor conduction band and holes are consequently generated in its valence band. Due to the discrete band structure of semiconductor, the photo-induced electron-hole pair will not re-combine immediately. Driven by the electronic field caused by space charge layer, the photo-generated charge carriers migrate toward the surface of the catalyst, and their fate may take different paths, as shown in Figure 1.2.[8]

First, during the diffusion inside the catalyst, the electron or hole may encounter their counterparts and recombine with them, producing thermal energy. Or they migrate to the par-ticle surface and recombine there. If the electron-hole pairs are not recombined, they might get trapped, either in shallow traps or in deep traps. Driven by the electric field formed in the space charge region on the semiconductor-electrolyte interface, electrons can react with acceptors (A) adsorbed on catalyst surface:

$$e^- + A \rightarrow A^- \tag{1.1}$$
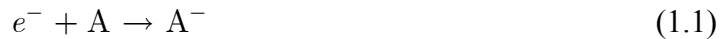
Simultaneously, the photo-induced holes immigrate to the surface of the semiconductor photocatalyst and oxidize the adsorbed electron donors (D):

$$h^+ + D \rightarrow D^+ \tag{1.2}$$

The competition between electron-hole pair recombination and charge carrier trapping deter-mines the overall quantum efficiency for that the interfacial charges is the major factor. Surface modification, doping and semiconductor coupling can reduce the possibility of electron-hole pair recombination and thus can be used to enhance the photoactivity.

Although the roles that photo-induced charge carriers play in photocatalytic redox reactions have been widely accepted, detailed chemical processes on the semiconductor-electrolyte in-terface are yet unclear. By now, two principal pathways have been proposed in the oxidation of
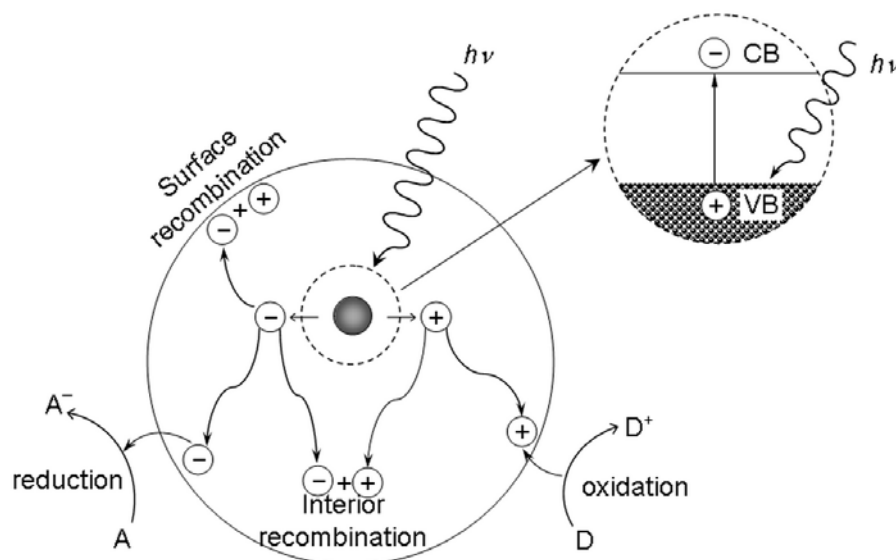
Figure 1.2 Overview of the steps in the conversion of light to the reactions on surface of semi-conductor. (1) charge carrier recombination at solid surface to liberate heat; (2) interior recombination; (3) electrons migrate to the catalyst surface and initiate a reduction reaction; (4) initiation of an oxidation reaction by valence band hole. (Diagram after Ref [12].)

organic molecules. Taking the photocatalytic process by TiO_2 as an example, the surface chemisorbed OH^- group and/or physisorbed H_2O on catalyst trap the photogenerated holes and yield $OH^\bullet$ radicals.[9] It is widely accepted that these $OH^\bullet$ radicals are the principal reactive oxidant in the photocatalytic reaction system based on the observation of the detected intermediates during the photodegradation of some organics.[10] Some other researchers argue that the organic molecules can be oxidized directly by photogenerated holes (see Table 1.1) since they failed to detect any of the expected $OH^\bullet$ intermediates. The conduction band electron can also be trapped by dissolved O_2 molecules to form superoxide ions. In both pathways, the interface charge transfer efficiency can be improved if the target molecules are pre-adsorbed on the surface of semiconductor.[8]

Once generated *via* reactions with charge carriers, the active species ($OH^\bullet$ or $H_3O^\bullet$) could be involved in reactions as follows[10]: 1) chemical reactions between activated species and adsorbed organics or species themselves; 2) the activated species leave the surface of semiconductor to initiate reactions with organics in solution. In kinetics, the formation of $D^{\cdot+}$ and the back transfer of the electrons are two competitive processes. In terms of solar energy utilization, the complete electrolytic decomposition of organic pollutant molecules is possible if the conduction energy is as least positive (*i.e.* lower in the diagram) as that required to oxidize the organics, and vice versa.
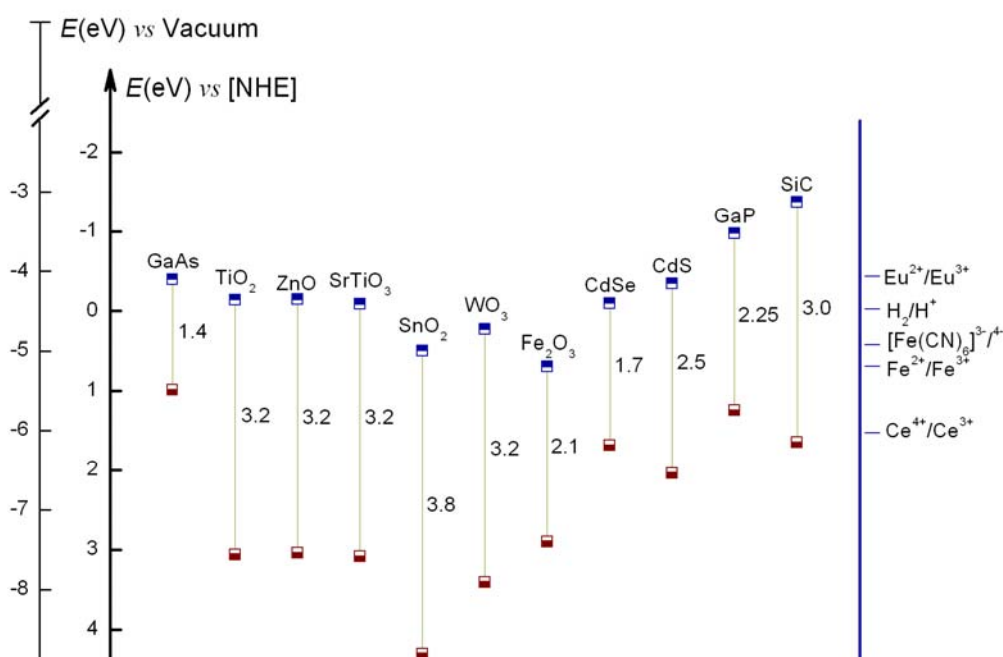
Figure 1.3 Energy band positions for various selected semiconductors at pH=1.[23]

For successful reactions with high efficiency of photocatalyst, efficient hole transport inside the catalyst and efficient hole transfer at the interface of semiconductor-electrolyte must be achieved. This requires sufficient lifetime of the charge carriers so that the holes can reach the interface before they recombine. When at the interface, the holes must react quickly with electron donor. Therefore a high reaction is expected if the organics molecules are pre-adsorbed on the surface of the catalyst.

In photocatalytic reactions, the band edge positions of semiconductor photocatalyst are of significance because they determine the thermodynamics limitation for the photoreactions that can be initiated by the charge carriers. In addition, the band edge positions influence the migration inside the catalyst crystals and their interaction with adsorbed surface molecules.[11] The energy band diagram for several common semiconductors in pH=1 solution are given in Figure 1.3. As shown, the redox potential for photogenerated holes is as high as comparable with that of various strong oxidant such as $HClO_4$, Cl_2 and O_2. And the redox potential for conduction band electrons is in principle negative enough to evolve many reduction reactions. Thus the organic pollutant molecules in aqueous or gaseous phases can be deeply mineralized into small inorganic molecules:

$$C_nH_mN_xO_yCl_z \xrightarrow[semiconductor]{h\nu} nCO_2 + xHNO_3 + zHCl + \omega H_2O \qquad 1.3$$
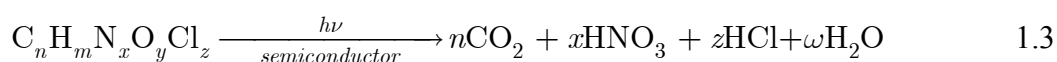
Table 1.1 The mechanism of photocatalytic reactions on TiO_2 and characteristic step time.[12]

	Primary Reaction Process	Characteristic Time
Charge carrier generation	$TiO_2 + h\nu \rightarrow h_{vb}^+ + e_{cb}^-$	very fast (ps)
Charge carrier trapping	$h_{vb}^+ + > Ti^{IV}OH \rightarrow \{> Ti^{IV}OH\cdot\}^+$	fast (10 ns)
	$e_{cb}^- + > Ti^{IV}OH \leftrightarrow \{> Ti^{III}OH\}$	shallow trap (100 ps)
	$e_{cb}^- + Ti^{IV} \rightarrow > Ti^{III}$	deep trap (10 ns)
Charge carrier recombination	$e_{cb}^- + \{> Ti^{IV}OH\cdot\}^+ \rightarrow > Ti^{IV}OH$	slow (100 ns)
	$h_{vb}^+ + \{> Ti^{III}OH\} \rightarrow Ti^{IV}OH$	fast (10 ns)
Charge carrier transfer	$\{> Ti^{IV}OH\cdot\}^+ + Red \rightarrow > Ti^{IV}OH + Red^{\cdot+}$	slow (100 ns)
	$e_{tr}^- + Ox \rightarrow > Ti^{IV}OH + Ox^{\cdot-}$	very slow (ms)

1.2.2 Parameters Influencing the Photocatalytic Process

Photocatalytic reactions are a highly complex process with many affecting factors. Competition between capture of the photoinduced charge carriers and recombination is crucial to the photocatalytic reaction rate and determines the quantum efficiency of the photocatalyst. To develop high efficient photocatalyst, it is essential to understand the reaction process. Hoffmann proposed a mechanism for heterogeneous photocatalysis of organic molecules on TiO_2 surface based on laser flash photolysis measurements.[12] Characteristic times for various steps in the mechanism were measured and are given in Table 1.1.

The characteristic time of each step listed in Table 1.1 indicates that the overall quantum efficiency for interfacial charge transfer is determined by two critical processes, namely, the competition between charge carrier recombination and trapping followed by the recombination and interfacial charge transfer. In order to improve the quantum efficiency of photocatalytic process, an increase in either the recombination lifetime of charge carriers or the interfacial electron transfer rate constant is required. One point should be mentioned is that the photocatalytic reaction mechanism proposed by Hoffmann is based on the assumption that the substrate does not undergo direct hole transfer and oxidative electron transfer occurs exclusively through a surface-bound hydroxyl radical, $\{> TiOH^\cdot\}^+$ or equivalent hole species.[12] However, there are many reports on direct oxidation by the valence band holes before it is trapped by the hole species.[13, 14]

From the discussion above, a typical degradation reaction of organics over illuminated photocatalyst is highly complex with many factors influencing the reaction process. Generally, these parameters can be divided into intrinsic and extrinsic ones that are related to the properties of the photocatalyst itself and external factors such as operating conditions, etc.

1. Particle size and crystalline structure

It has been reported that the particle size plays an important role in photocatalysis mostly through influencing the dynamics of electron-hole pair recombination.[15] Assuming the diffusion of photogenerated charge carriers obey the random walk model, the average time needed for charge carriers to migrate from interior to the surface of the photocatalyst particle can be expressed as follows[16]:

$$\tau_d = r^2 / \pi^2 D_e \qquad\qquad 1.4$$

where r is the particle radius and D_e is the carrier diffusion coefficient which is the intrinsic property of one photocatalyst. The formula shows that reducing the particle size r is favorable for the transport of charge carriers, and therefore photon quantum efficiency can be benefited. On the other hand, decreasing the particle size will increase the surface-to-volume ratio of the catalyst, and hence generally leads to a greater concentration of active site and a higher reactivity. However, once the particle size falls below certain critical value, quantum effects may occur and light response region may be reduced.[17]

Impurities, crystal defects and surface status of semiconductors also influence the quantum efficiency of photocatalytic properties because they can form energy level in forbidden band of semiconductors. For example, the active oxygen vacancies can easily combine with other atoms or groups and result in the increase of the amount of the surface hydroxyl oxygen, favoring the improvement in photoactivity of oxide semiconductors.[18] The formation of energy level of crystal surface defects could reduce the recombination lifetime of the charge carriers. Generally, the defects of photocatalyst crystals mainly come from the preparation process. Nakamura *et al.*[19] introduced surface oxygen vacancies on surface of TiO_2 by H_2 plasma treatment. Electron spin resonance (ESR) measurement demonstrated that more electrons have been trapped since oxygen vacancy state is formed between the conduction and valence band of TiO_2.

High crystallinity of semiconductor nanoparticles or films was also found to account for the improvement of photoactivity.[20, 21] Catalytic decomposition of H_2O_2 was recently investigated on illuminated iron oxide of different crystallinity.[22] The results showed that the catalytic efficiency of iron oxide nanoparticles was strongly determined by the crystallinity of the particles other than their surface area.
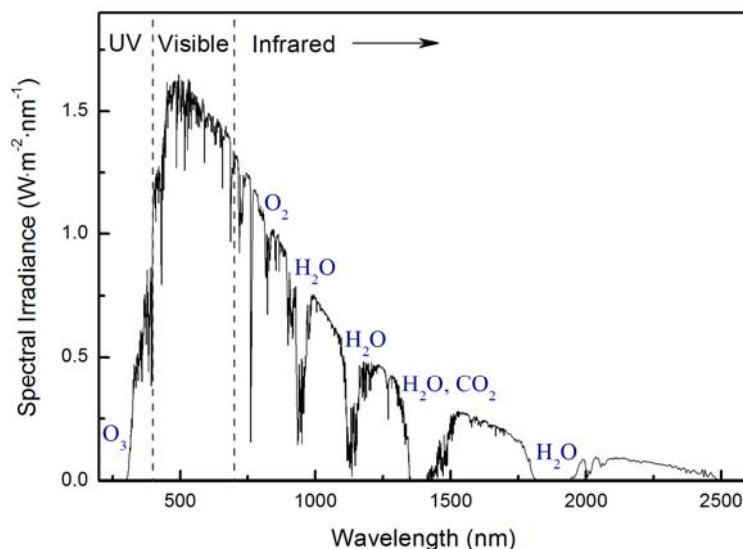
Figure 1.4 The earth's light irradiation environment (solar spectrum).[4]

2. Band edge positions

The band gap energy of a semiconductor is defined as the difference in energy between the conduction band edge and the valence band edge. The band edge positions of semiconductors indicate the thermodynamic limitations for the photoreactions that can be carried out by the photo-induced charge carries. If the oxidation reaction is desired by the photocatalyst, the valence band edge of the semiconductor must be positioned favorably relative to the oxidation potential of the absorbed molecule. On the contrary, if the reduction reaction is required, the conduction band edge of the semiconductor must be positioned higher than the reduction potential of the target molecule. The flat band potentials of several semiconductors are listed in Figure 1.3.[23]

In case that the nanoparticle radius is smaller than the Bohr radius of the bulk exciton, the quantization energy of both electrons and holes is larger than the binding energy of an exciton due to the strong confinement effect,[17, 24] causing the change of band gap and band edge positions. As a nanoparticle's radius decreases, its band gap increases primarily with an increase in conduction band energy levels and also a slight decrease of the valence band energy levels.

Actually, many photocatalytic reactions occur in aqueous solutions, with some process parameters influencing the quantum efficiency of the reaction:

1. Light intensity and wavelength

The incident irradiation provides the energy source for the photocatalytic reactions. Degradation rate has been found to have a linear dependence on the photon flux for TiO_2.[9] It has also

been reported that the light intensity affects the optimal catalyst dosage. The higher the light intensity is, the higher the optimal catalyst dosage.[25] Tabata proposed that the water splitting rate over $K_4Nb_6O_{17}$ photocatalyst is proportional to the square root of the light intensity and proportional to the intensity at low intensity.[26] On the other hand, the photocatalytic performance of *n*-type semiconductors originates from their band structure. Only photons with energy higher than band energy gap can be absorbed by semiconductors to initiate the reactions, meaning that there exists a critical wavelength for the photocatalyst. For instance, the characteristic absorbance wavelength for TiO_2 and α-Fe_2O_3 are 400 and 560 nm, respectively.

2. The solution pH

The pH of the photocatalyst slurry has been found to have a significant influence on the photocatalytic process. For example, Bahnemann reported that the photodegradation rate of $CHCl_3$ at pH 8-9 is about 10 times higher than that at pH 3.8.[27] Similar observation on many photocatalytic reactions proves that there is an optimal pH for the highest photocatalytic reaction rate.[28-30] The photoactivity dependence on pH can be interpreted in four aspects:

(1) electrostatic interaction between charged semiconductor nanoparticles and the contaminants. The surfaces of most oxide semiconductors are amphoteric, *i.e.*, they carry positive net surface charge at low pH, and vice versa. The adsorption of electroactive species is governed by the Langmuir adsorption equilibrium equation, and thus the adsorption isotherm of organic contaminants can be changed by solution pH. The zero charge point (ZCP) for TiO_2 and α-Fe_2O_3 are 6.25 and 6.5,[31] respectively. In addition, the dispersion of nanoparticles may get improved when the pH of the solution departure from the ZCP of the photocatalyst, resulting in an increase of the irradiated area of the semiconductors.

(2) the semiconductor flat-band potential variation. It is reported that flatband potential of the semiconductor in electrolyte is a function of pH, causing the variation of absorption of irradiated photons and redox potentials of photo-induced charge carriers. The surface flatband potential follows a Nernstian pH dependence over a pH range around the ZCP.[32]

(3) completing between trapping of charge carriers by H_2O and OH^-;

(4) structure state of organics in solution. Due to the complex structure of organic molecules, solution pH value may change the state of the contaminant, resulting in an ultimate change in the electrostatic interaction between the molecule and the catalyst surface.

It should be noted that the literature report on the effect of pH on the degradation of the organics is disperse and contradictory. Some researchers stated that pH has small effect on photocatalytic reactions.[11]

3. Surface hydroxyls

Surface hydroxyls have been proposed to scavenge valance holes to ultimately produce the hydroxyl radicals ($OH^\bullet$, see Table 1.1) which are known as the primary oxidizing species in photocatalytic reactions.[9, 29, 33-35] Due to this, the adsorbed surface hydroxyls are regarded identical as trapped surface holes, although they suffer different pathways in detailed reaction mechanisms.

Hoffmann proposed that the surface hydroxyl groups are the principal reactive sites on hematite surface and the oxidation of S(IV) were preceded *via* rapid formation of Fe(III)-S(IV) surface complexes formed by ligand exchange with surface hydroxyl groups.[36]

4. Dissolved oxygen in water

Much research supports that the dissolved O_2 plays an important role in photodegradation of organics in aqueous solutions. Experiments have demonstrated the dependence of the initial reaction rates of the pollutant photodegradation on O_2 concentrations (partial pressure was used according to Henry's law).[37] It was found that the conversion rate of 2-chlorobiphenyl into CO_2 increased from 16% to 94% with the oxygen partial pressure increasing from 0.5 kPa to 186 kPa. In photocatalytic reaction process, the dissolved oxygen readily adsorbs on the TiO_2 surface and can be reduced by conduction electron, producing superoxide radical ion, $O_2^{-\bullet}$, or the protonated form, perhydroxyl radical, $HO_2^\bullet$ [38, 39]:

$$O_2 + e_{cb}^- \rightarrow O_2^{-\bullet} \ \text{or} \ O_2 + 2H^+ + 2e_{cb}^- \rightarrow 2HO_2^\bullet \qquad\qquad 1.5$$
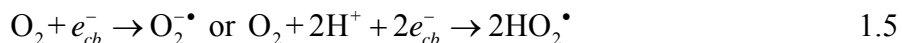
Two $HO_2^\bullet$ radicals can be recombined to yield H_2O_2 and O_2, allowing H_2O_2 scavenges an electron from the conduction band where $OH^\bullet$ radicals are generated:

$$H_2O_2 + e_{cb}^- \rightarrow HO^\bullet + HO^- \qquad\qquad 1.6$$

Depending on the degradation mechanism of the pollutant, oxygen molecules may promote or hinder the reactions under different reaction conditions.

5. Organic additive

Electron-hole recombination is a major cause that reduces the activity of photocatalyst. In photocatalytic process, electron donors are often applied to react irreversibly with the photo-generated holes to enhance the electron-hole separation. Addition of some organic additives with different hydroxyl groups, such as methanol, propanol, glycerol and ethylene glycol[40] was reported to be helpful in the reduction of electron-hole recombination losses in TiO_2 photocatalysis due to the binding interaction between groups of OH and titanol (TiOH). Effects of addition of EDTA (Ethylene Diamine Tetraacetic Acid) and oxalate on decomposition of H_2O_2 over α-FeOOH were investigated.[29] Due to the strong chelating and high stability of Fe(III)-EDTA, adding EDTA is more effective than oxalate.

An admicelle mechanism on enhancement of photocatalytic efficiency of iron oxide by addition of organics was proposed based on effects of a strong oxidation resistance surfactant, trimethylstearylammonium chloride (C_{18}-TAC).[41] The admicelle on α-Fe_2O_3 surface formed by adsorption bilayer of amphiphilic molecules assisted both the transfer of contaminants from the aqueous phase to the photocatalyst surface and the transfer of oxidized products in the opposite direction.

6. Ions in solution

Depending on the pathways, the adding of ions into the photocatalytic slurry could inhibit or promote the degradation of contaminants over photocatalysts. Experiments[42] demonstrated that the rate of chlorophenol degradation by photocatalysis could be accelerated in presence of Mn^{2+}. This is because that the Mn^{2+} ion decreases the e-h recombination by involving the surface reaction.

Abdullah *et al.* investigated the effects of common inorganic anions on rate of photocatalytic oxidation of organic carbon over illuminated TiO_2 and reported the rate dependence on type of anions.[43] By measuring the yielding rate of CO_2, it was found that the anions of ClO_4^- and NO_3^- does not influence the photoactivity of TiO_2 while SO_4^-, Cl^- and PO_4^{3-} have disadvantageous effect.

1.3   State-of-art of Modification of Photocatalysts

Based on the recognition on photocatalytic reaction mechanism, much effort has been made to promote the photocatalytic activity and enhance the visible light response of oxide type photocatalysts. Metal ion doping, anion doping, composite semiconductors, noble metal loading, dye sensitization, and addition of hole scavengers etc., were studied and some of them have been proven to be effective to improve the photocatalytic performance.

1. Ion doping

The energy level of dopant ions could hybridize with that of semiconductors. The band gap of semiconductors can thus be changed, resulting in expanding in photo-response. When metal ions are incorporated into the TiO_2 lattice, impurity energy levels are formed in the band gap of TiO_2. The doping metal ions, serving as the charge scavenger, could inhibit the recombination of electron-hole pairs and thus improve the photocatalytic activity. Many metal ions, including transition metal ions and rare earth metal ions have been extensively investigated for enhancing the TiO_2 photocatalytic activities. Grätzel *et al.* studied the photoresponse of aqueous colloidal TiO_2 doped with Fe, V and Mo using electron paramagnetic resonance technique.[44] An increase in Ti^{3+} signal was found during irradiation of aqueous doped TiO_2 colloids The increase

was attributed to inhibition of hole-electron recombination by metal ion dopants. The hole or electron trapping caused a fading in V^{4+} signals on irradiation of V-doped TiO_2 powders at 77 K. By systematic investigations to study the effects of ion categories, dopant concentration, structures of d electrons of dopants, etc., it was found that the doping of some metal ions is in favor of the photocatalytic activities of photocatalyst, while some others are not.[39, 45-47] This is because that the doping ions can not only prolong the lifetime of the hole-electron pair by trapping the photoinduced charges, but also shorten the pair lifetime by serving as the recombination center.

Compared with metal cations, anions are more effective to enhance the photoactivity of photocatalyst because they have little propensity to form recombination centers. In 2001, Asahi *et al.* reported the visible-light induced photocatalytic activity of N-doped TiO_2 powders by sputtering in a N_2/Ar gas mixture and treating anatase in an NH_3 atmosphere, respectively.[5] XPS analysis and first principle calculation showed that the hybridization between the $2p$ energy levels of O and N narrows the band gap of TiO_2 and leads to a red-shift in its spectrum response region.[5, 48] After that, the doping effects of non-metallic anions, such as N,[48, 49] F,[50] B,[51-53] S and C,[54] on photoactivities and photoelectrochemical properties of TiO_2 have been investigated. However, the best results for anion doping by far is obtained by N-doping.

In recent years, the ion doping of hematite has been extensively investigated. In contrast to changing the band structure of TiO_2 by doping, the aim of hematite doping is to improve its charge transport characteristics. In 2008, it was reported by McFarland's group[45] in UC Santa Barbara that Cr or Mo doped $\alpha\text{-}Fe_2O_3$ photoanode could be prepared by electrodeposition on FTO conducting glass substrate. By changing the molar ratio of Cr (or Mo) precursors in electrolyte, the dopant concentration varies from 0% to 20 % in the final product. It was found that when $\alpha\text{-}Fe_2O_3$ was doped with Cr, the substitution of Fe^{3+} by Cr^{3+} increases the electronic conductivity of doped film by providing an extra $3d$ electron. Since the low photoactivity of hematite is mainly caused by low electron mobility in hematite crystal,[55] increasing the conductivity could improve the photoelectrochemical performance. Therefore, a large increase in photocurrent for Cr-doped hematite was observed at an applied bias over 0.2 V. The similar improvement was observed for Mo doped hematite film even without the application of the bias. Also an improvement in efficiency for photoelectrochemical water splitting was observed on Pt-doped hematite by the same group.[46]
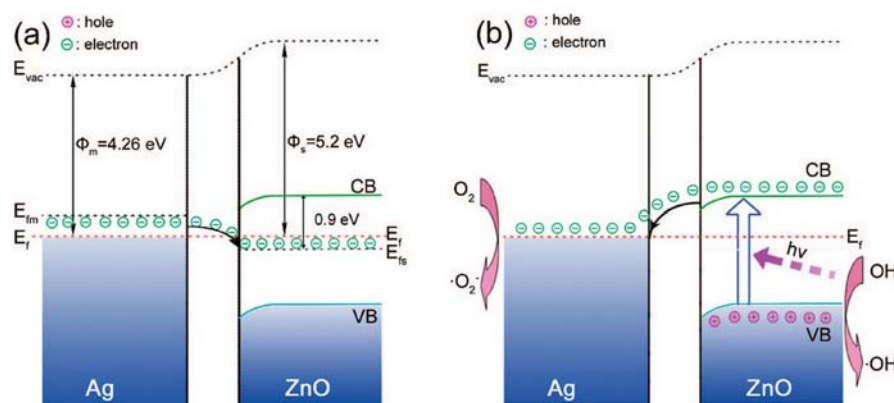
Figure 1.5 (a) The band structures of Ag/ZnO junction and Fermi energy level equilibrium without UV irradiation. (b) Charge separation process of Ag/ZnO junction under UV irradiation.[61]

After studied the enhanced photoelectrochemical response of Zn-doped hematite, Kumari *et al.* pointed out that enhancement could originate from the wide bandgap ZnO clusters on the hematite surface which were converted from the surface Zn-dotted islands when annealed.[47]

Additionally, there are some reports in literature on non-metallic ion doping of hematite to improve the photoelectrochemical properties.[56-59] Cesar reported the preparation of iron oxide photoanodes by ultrasonic spray pyrolysis and thermal decomposition of iron-organic salts.[59] It was found that the photoresponse was increased by a factor of 16 when silicone tubing, instead of Tygon tubing, was used to pump the precursor solutions. Further research confirmed that an uptake of a silicon compound by the deposition solution from the silicone tubing caused the morphology change, i.e., forming a film of stacked sheets oriented perpendicularly to the substrate. Since the electrical resistivity of hematite in the basal plane is four orders of magnitude higher than that along the trigonal axis,[60] the preferred orientation of the (001) plane normal to the substrate caused by silicon doping significantly improves the photoresponse of the films.

2. Modification by noble metal loading

Similar to the interface of semiconductor-electrolyte, Schottky energy barrier can form on the metal-semiconductor interface if the Fermi level of the metal is lower than that of semiconductor. In this case, photo-induced electrons may transfer from semiconductor to metal nanoparticles until the two system attain equilibrium and form the new Fermi energy. Noble metal deposition can thus improve the photocatalytic activity of photocatalysts by increasing electron-hole separation. For example, small silver nanoparticles deposited on the surface of ZnO have been shown to efficiently overcome the electron-hole recombination reaction, favoring hole trapping and successive oxidation process.[61, 62] This effect was attributed to elec-

tron capture by Ag^0, i.e. the noble metal deposit can act as a sink for photo-induced electrons. As shown in Figure 1.5, the Fermi level of ZnO is lower than that of Ag, resulting in the transfer of electrons from Ag to ZnO until the two systems attain equilibrium and form the new Fermi energy (E_f). However, the bottom energy level of the CB of ZnO is higher than the new equilibrium Fermi energy level of Ag/ZnO, and the photoexcited electrons on the CB under UV irradiation can transfer from ZnO to Ag nanoparticles. The lifetime of the electron-hole pair has thus been prolonged and the photocatalytic activity of semiconductor can be improved.

Usually, the deposited noble metal on the surface of semiconductor does not cover the whole area of the semiconductor but form atomic clusters on the surface. Noble metals including Pt,[46] Pd, Au,[63, 64] Ag[65] and Rh are often used and have been proven very effective for enhancing ZnO or TiO_2 photocatalysis.

Although the loading of noble metal can reduce recombination to enhance the photocatalytic activity, stability of semiconductor-metal interfaces during photoelctrochemical operation is a concern. Kamat *et al.* measured the photocurrent of Au(Pt, or Ir) loaded TiO_2 and found that the photocurrent benefits from metal deposition at the initial stage of illumination as a result of charge separation promoting.[66] However, the photocurrent enhancement decays with UV irradiation time over a long period, which is caused by the formation of Au^+ ion as recombination center.

3. Semiconductor coupling

The natural difference in energy band level of different semiconductors can be utilized to separate the electron-hole pairs and enlarge the light response region. The typical semiconductor coupling system employing photosensitization is CdS-TiO_2 nanocomposite. Figure 1.6 schematically illustrates the mechanism of charge separation at the CdS-TiO_2 interface.[67] CdS with a band gap of 2.5 eV is used as the synthesizer for TiO_2 with a large band gap of 3.2 eV because of the ideal position of its conduction and valence band edges. The electrons in CdS that are excited by irradiations with wavelength larger than 387 nm which, however, can not generate charge pairs in TiO_2, can be transferred to the conduction band of the couple TiO_2 particles. The electron-hole pair is thus separated at two phases as a result of interparticle charge transfer that occurs from CdS particle to TiO_2. The positive holes are left on CdS to participate oxidization reaction. The charge carrier recombination possibilities can be reduced, since the transferred electrons have no holes to recombine with and they can only participate in the reduction reactions according to the conduction band energy level of TiO_2 since the electrons have already lost part of their initial energy in transferring from CdS.
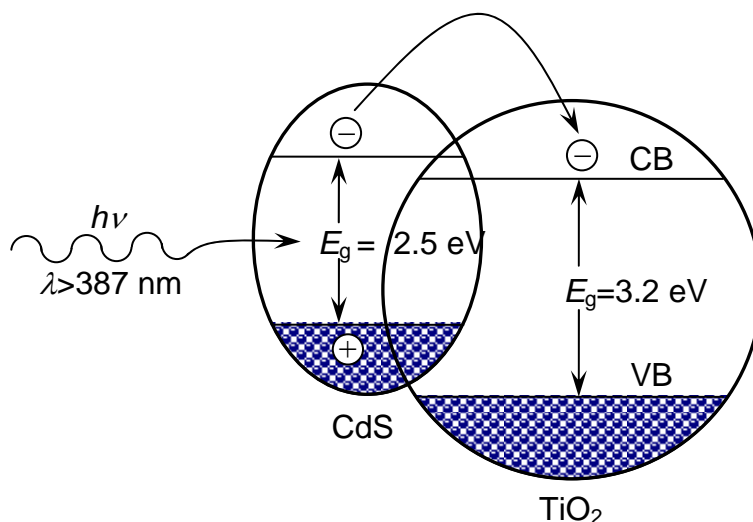
Figure 1.6 Diagram of charge transfer and separation at the interface of CdS-TiO$_2$ composite after illumination by light (λ>387 nm).[67]

In comparison with other modification techniques, the advantage of composition lies in that the band energy and light adsorption region can be easily altered, especially for TiO$_2$ based photocatalysts. However, the toxicity and chemical instability of CdS constrict the wide applications of CdS-TiO$_2$ nanocomposite. Finding the new photocatalyst still remains as a challenge and many research efforts are currently underway to develop new semiconductor composite based on some other promising semiconductors.

Due to nonradiative recombination and trapping mediated by the d states in the band gap, the excited-state lifetimes of hematite is much lower than that of TiO$_2$. To improve the catalytic activity of hematite through carrier charge separation, $\alpha-Cr_2O_3 / \alpha-Fe_2O_3$ type-II heterojunction was prepared *via* a solution method by using $\alpha-Fe_2O_3$ nanoparticles as seeds. The charge carrier lifetimes and dynamics were investigated using femtosecond transient absorption spectroscopy. Joly *et al.* reported that no solid evidence was observed to support the premise that the $\alpha-Cr_2O_3 / \alpha-Fe_2O_3$ interface significantly alters the excited carrier lifetimes. The limitation of band-offset engineering was attributed to the *d-d* transitions and defect states in these materials.[68]

In the research on photocatalytic performance of iron oxide dependence on sintering temperature, Xu's group found that the dispersion of $\alpha-Fe_2O_3$ in SiO$_2$ can not only pin the growth of hematite nanocrystals, but also enhances the photocatalytic activity towards the degradation of azo dye molecules. As shown in Figure 1.7, the photocatalytic performance of $\alpha-Fe_2O_3$ is deteriorated by sintering at high temperature. However, when dispersed in SiO$_2$,
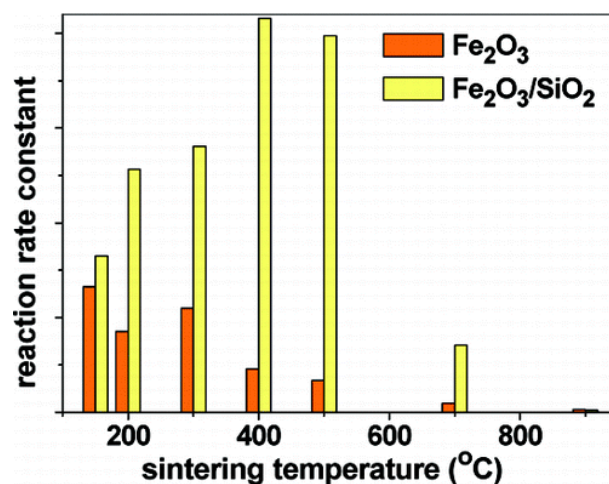
Figure 1.7 The comparison between the apparent rate constant of dye photodegradation over Fe_2O_3 and Fe_2O_3/SiO_2 after sintered at different temperature[21].

sintering at high temperature has a positive effect on photocatalytic activity. This is because the growth of hematite was inhibited by SiO_2 in the process of improving the crystallinity.[21]

    4.   Surface dye-sensitization

    Dye sensitization is widely used to harvest visible light. This strategy was first proposed by Prof. Grätzel in 1991 to increase the photon to current conversion efficiency of solar cells.[69] After physical or chemical adsorption onto the surface of semiconductor, the surface chelating dye molecules can influence the band structure of semiconductors, Under illumination of visible light, the excited dyes can inject electrons to conductance band of semiconductors to initiate the catalytic reactions. The sensitization requires that the excited state of sensitizer is higher than conductance band of semiconductors, such that the excited electrons can be transferred into the semiconductors. Many different compounds have been investigated for semiconductor sensitization, such as Ru-bipyridine complex, porphyrine, phthalocyanines, coumarin and carboxylated derivatives of anthracene.[70, 71] Among the photosensitizers investigated, transition metal complex have been confirmed to be the best so far.

    Besides molecule energy level, the binding state between dye and semiconductor surface is also an important parameter that affects the photon to current conversion efficiency. Because the chemical bond between dye and semiconductor can induce a solid adsorption of the dye and could change the surface energy state. However, people have not achieved agreement about the charge transfer mechanism between sensitizer and semiconductors. A hopping type mechanism has been proposed to explain the charge transport process which states that the process involves the hole injection from substrate and hopping of electrons in single molecule layer.[72, 73]

Up to date, three aspects of dye sensitization to modify semiconductor photocatalyst have been investigated: 1) inhibiting recombination rate by increasing the charge separation and therefore the efficiency of the photocatalytic process increased; 2) increasing the spectrum response range; 3) changing the selectivity or yield of a particular product. Although much work has been done, the quantum efficiency is still low because the electrons which are injected into the solid from dye are easily to transfer back to the dye molecules to recombine with holes. It should be noted that the competition between the adsorptions of dye and contaminant molecules on the surface of semiconductor also limit the enhancement of the photocatalytic activity.

5. External field assistance

Several external fields,[56, 74, 75] such as microwave, electric field, and plasma, have been combined with photocatalytic reactions to improve the quantum efficiency. Synergistic effects of the external fields have been reported. The application of an electric field could provide a positive potential across the photocatalyst electrode, producing a potential gradient inside the film that forces the photoexcited holes and electrons to move in opposite directions, thus the photocatalytic efficiency can be improved as a result of lower charge carrier recombination rate.

The polarization effect of microwave field creates many unsaturated bonds on the surface and forms charge carrier sinks inside the photocatalyst. These defects could provide energy levels to serve as the charges sink to reduce the possibility of recombination. On the other hand, microwave field can promote the conversion of surface hydroxyl into free radicals, which have been proven to be essential in photocatalytic reactions of organics degradation.

1.4 Structure and Optoeletrochemical Properties of Iron Oxide

In the above, we have outlined the main requirements of photocatalyst based on the analysis of the working principles of photodegradation of contaminants over illuminated semiconductors. Several semiconductors with band-gap energies sufficient for photodecomposing a wide range of organic pollutant molecules have been suggested as photocatalysts, including TiO_2, WO_3, ZnO, $\alpha\text{-}Fe_2O_3$ and CdS, the band edge positions of which are schematically shown in Figure 1.3. The ideal photocatalyst should meet the requirement of:

(1) Strong adsorption in visible light region;

(2) Stability in dark and under irradiation;

(3) Proper band gap and flat band position;

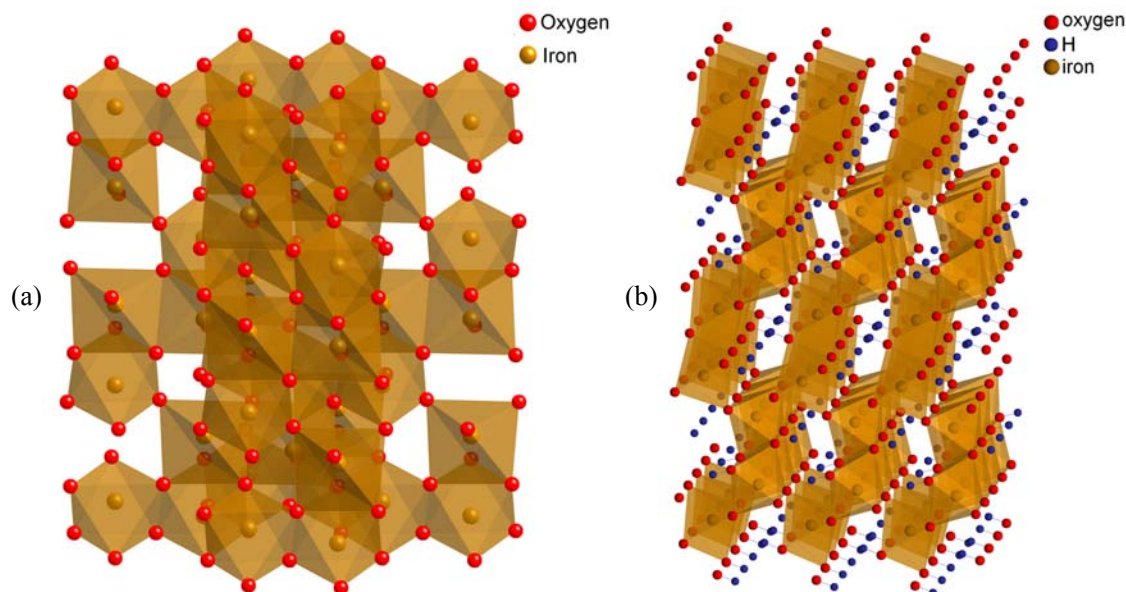(4) Environmentally friendly, cost-effective, etc.

Figure 1.8 Crystal structure of (a) hematite and (b) goethite. The iron atoms are in the oxygen octahedra or in the tetrahedra.

TiO_2 has so far dominated the research activity on photocatalysis in terms of synthesis, characterization and applications. The popularity comes from the moderate band gap, non-toxicity, high surface area, high photo-activity and excellent chemical stability under irradiation. However, the disadvantage of TiO_2 as a photocatalyst lies in its wide band gap (about 3.2 eV at room temperature), which makes that TiO_2 can only utilize solar light below 385 nm. Although many scientific efforts have been devoted to explore the materials with high photo-activity, material that fulfills all the requirements are still lacking. Recently researches point out that iron oxide based materials are highly promising if crystal structure and morphologies are well controlled.[22, 38, 60, 76, 77]

There are various ferric iron oxide or oxyhydroxide in nature, including α-Fe_2O_3, Fe_3O_4, γ-Fe_2O_3, α-FeOOH, β-FeOOH, γ-FeOOH. Among these, α-Fe_2O_3 and α-FeOOH are the most stable from the view point of thermodynamics and have a large abundance in earth crust. Being isostructural with corundum, a hematite crystal consists of layers of $Fe(O)_6$ octahedra that are connected by edge- and face sharing stacked along c-direction. Two thirds of the octahedral sites are occupied by Fe^{3+} ions (Figure 1.8a). Goethite crystals can be described as a three-dimensional structure built up with $FeO_3(OH)_3$ octahedra which form large tunnels along the direction [010]. The $FeO_3(OH)_3$ octahedron is formed by one Fe^{3+} cation which is surrounded by three O^{2-} and three OH^-. Each octahedron is linked to eight neighboring octahedra through four edges and three vertices (Figure 1.8b). In comparison to the structure of goethite,
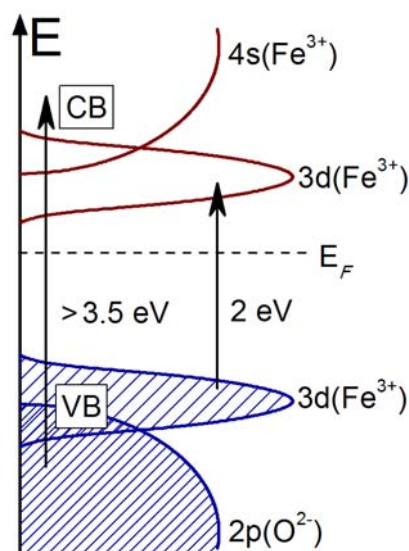
Figure 1.9 Band structure of hematite.[79]

the absence of hydrogen bonds in hematite crystal results in a compact structure with high density and crystallinity. The structure of goethite can transform topologically into hematite as a result of thermal dehydration since the two structures can both be described as slightly distorted *hcp* stacking of anions (O^{2-} or OH^-).[78]

Band structure of semiconductors, including band gap and band edge positions, plays a crucial role in photoelectrochemical and photocatalytic applications. Figure 1.9 illustrates the band structure of α-Fe_2O_3 crystals,[79] demonstrating that the 3*d* orbit of iron cations splits into e_g and t_{2g}. The empty e_g and 4*s* of iron cation constitute the conduction band of iron oxide. And the valence band is composed by Fe^{3+} t_{2g} and 2*p* band of O. The complex band structure suggests that there are two typical models for the band-to-band transition of iron oxide. The first is a charge transfer model between the neighboring Fe^{3+} ions, where the electron transfer occurs between orbits of e_g and t_{2g}. The other one is the transition from 3*d* or 2*p* band to the 4*s* orbit of Fe^{3+}. The band gaps result from the two models are 2.2 eV and 3.1~3.5 eV, respectively. The calculation results are in agreement with the measurement made by Duret on hematite films.[76] Accordingly, lights with their wavelength below 560 nm can excite hematite and produce electron-hole pair inside iron oxide crystal. In comparison with TiO_2, the utilization rate of solar energy can be greatly increased.

Table 1.2 Hydroxyl density on various hematite and goethite facets.

Facet	Singly coordinated (groups nm^{-2})	Doubly coordinated (groups nm^{-2})	Triply coordinated (groups nm^{-2})	Contiguous singly coordinated (group pairs nm^{-2})
α -Fe$_2$O$_3$				
{100}	5.8	2.9	-	2.9
{110}	5.0	5.0	5.0	2.5
{012}	7.3	-	7.3	3.7
{104}	5.3	5.3	5.3	-
{018}	-	6.3	3.2	-
{113}	4.1	4.1	8.3	2.1
{001}	-	13.7	-	-
α -FeOOH				
{100}	3.3	3.3	6.7	1.7
{010}	7.2	7.2	-	3.6
{110}	3.0	3.0	9.1	1.5
{021}	8.2	8.2	-	4.1

Despite of the equivalent crystal structure to Al-oxides (*e.g.*, α - Al$_2$O$_3$) and other common soil minerals, hematite is much more reactive and effective in sorbing pollutants than α - Al$_2$O$_3$. Research showed that the difference originate from the special surface structure of hematite. Extremely intense synchrotron radiation measurement of crystal truncation rod (CTR) diffraction from hematite single crystal surface in contact with water revealed difference of surface structure of hydrated hematite relative to hydrated corundum.[80] As depicted in Figure 1.10, hematite surface was found to have two surface structure domains. One is dominated by oxygen singly coordinated by Fe^{3+} and is very reactive, while the other domain is dominated by oxygen doubly coordinated by Fe^{3+} which is relatively unreactive. Density functional theory (DFT) combined with thermodynamics was also used to predict the most stable surface structure of
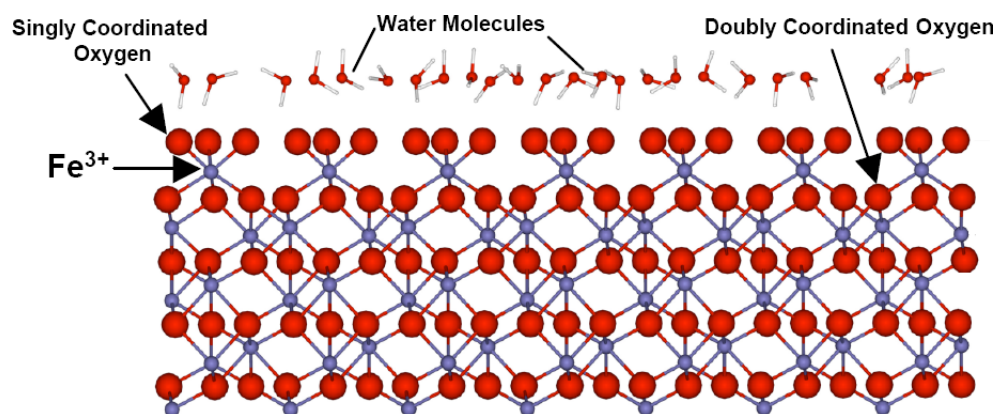
Figure 1.10 Surface structure of hematite. (viewed side-on)[80]

hematite, and the results fit well with the measurements.[80]

The hydrophilicity research on hematite surface demonstrated that the wettability can be switched from ultrahydrophobicity to superhydrophilicity and vice versa with UV (254 nm) irradiation and dark storage.[81] In tradition, the wettability conversion of inorganic materials is attributed to surface hydroxyl adsorption resulted from UV-induced charge generation. However, high-resolution XPS research ruled out the changes of surface hydroxyl radicals. Further investigation suggested that the surface Fe^{2+} defects produce the excited state $*Fe^{2+}$ after UV illumination, and the excited $*Fe^{2+}$ ions are oxidized back to Fe^{3+} with the decomposition of organic pollutants. The wettability switch comes from the above two opposite processes.[81]

1.5 Preparation of Photocatalyst

Nanostructured photocatalysts have been synthesized with a number of different compositions and phases, including TiO_2, ZnO, WO_3, α-Fe_2O_3, as well their doped form of composite. In the last few years, many scientific efforts have been devoted to the synthesis of nanostructured semiconductors for solar energy conversion. In general, there are three routes to fabricate the photocatalysts: physical vapor deposition, mechanical milling as well as wet chemical routes. These all produce photocatalysts in form of solid powders with a reasonable control of the particle size and size distribution. Physical and mechanical milling method has been industrially used due to its low cost and simple processing, but control of particle size and morphology is somewhat difficult. However, wet chemical methods, including sol-gel, micellar,[82] hydro/solvethermal, and polyol[83] method may offer potentials to obtain photocatalysts in terms of chemical homogeneity and morphological control with respect to the physical method mentioned above.

1.5.1 Nanocrystal Growth in Solutions

Figure 1.11 schematically illustrated the growth process of nanocrystals in solutions which consists of following three steps: (1) nucleation. When the monomer concentration increases as a function of time, no nucleation would occur even above the equilibrium solubility. After the supersaturation reaches a certain value above the solubility by a rapid increase in the monomer concentration, the nucleation occurs and crystal seed forms in the solution. (2) Crystal growth from seeds by aggregation of monomers on the seed, resulting in progressive decrease in the monomers concentration. (3) Surface stabilization of the resulted nanocrystals by surfactants. The formation process of nanocrystal nuclei is achieved through at least the following steps: growth unit formation resulting from dissolving of solute; transport of growth unit in reaction
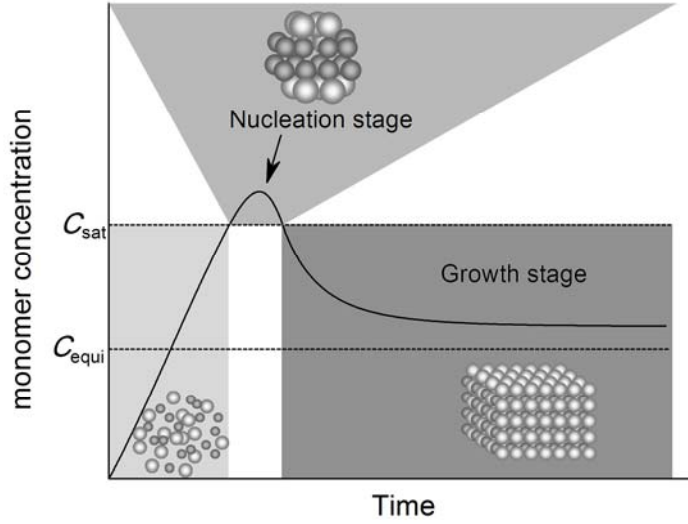
Figure 1.11 Growth diagram of nanocrystals in solution.

medium; diffusion and combination of crystal growth unit on nanocrystal surface; the forward moving of the interface between nuclei and reaction medium.

Because the growth of nanocrystal mainly occurs on the solid-solution interface, the overall regulation manipulation of the size distribution and the shape of nanoparticles can be achieved by controlling the interface energy and interfacial tension.[84, 85] The mechanisms of many effective strategies proposed for controlling the morphologies of inorganic nanoparticles are actually base on altering the interface chemistry, e.g., adding surfactants,[86-88] altering pH and temperature of the growth medium[89, 90], and changing the dielectric constant of the medium.[91]

Surfactants are often used to decrease surface tension γ of nanocrystals in solution. Such effect can be described quantitatively by the Gibbs adsorption equation:

$$\mathrm{d}\gamma = -\sum_i \Gamma_i \mathrm{d}\mu_i \qquad 1.7$$

in which Γ represents the superficial adsorption density and μ the chemical potential of the adsorbed species i. L. Vayssieres proposed a model to quantify the variation of the water-oxide interfacial tension with the chemical composition of the interface and the dispersion conditions:[92]

$$\Delta\gamma = \gamma - \gamma_0$$
$$= 25.7\sigma_{\max}\mathrm{Ln}\left[1 - I\left(\frac{0.117\sinh(1.15\Delta\mathrm{pH})}{\sigma_{\max}}\right)^2\right] - 6\sqrt{I}\left[\cosh(1.15\Delta\mathrm{pH}) - 1\right]$$

where I represents the ionic strength and σ the surface charge density. Assuming a zero interfacial tension at equilibrium, by analogy with microemulsion systems where ultralow surface tensions at equilibrium have been indentified, a quantitative treatment has been developed to

obtain the thermodynamic stability conditions of the water-oxide system for precipitation of metal ions in basic medium
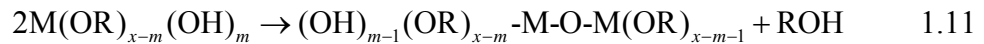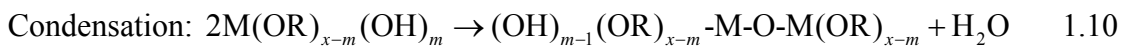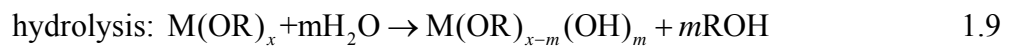
$$\mathrm{PZIT} = \mathrm{PZC} + 2.46 + 2\log\sigma_{\max} - \log I \qquad\qquad 1.8$$

where PZC and PZIT represent the point of zero charge and the point of zero interfacial tension, respectively. The surface charge does not reach its maximum if precipitation occurs between PZC and PZIT. Subsequently, the interfacial tension remains positive and the system is submitted to secondary growth and aging. As a result, the nanoparticles will evolve in solution, that is, their size will increase with time, and their crystal structure may be subjected to phase transformation. This is the unstable region of the precipitation. However, at precipitation $\mathrm{pH}{>}\mathrm{PZIT}$, the nanoparticles are thermodynamically stabilized, and no subsequent secondary growth phenomenon such as Ostwald ripening occurs.[92] The model also shows that the growth of nanoparticles is not only influenced by solute concentration, reaction temperature and period, but also is affected by pH and ion strength.

1.5.2 Sol-Gel method

Sol-gel is becoming a standard liquid route in synthesizing metal oxide nanostructures. The process is based on the hydrolysis and polycondensation of metal precursors, usually alkoxides in aqueous or alcoholic solutions. Further condensation and inorganic polymerization lead to a three-dimensional metal oxide network dominated gel. To reach the final crystalline state, thermal or hydrothermal treatments of the gel are needed. Advantages of this preparation are the production of ultrafine powders having high chemical homogeneity.

The steps of hydrolysis and condensation in sol-gel process can be expressed as

$$\text{hydrolysis: } \mathrm{M(OR)}_x + \mathrm{mH_2O} \rightarrow \mathrm{M(OR)}_{x-m}(\mathrm{OH})_m + m\mathrm{ROH} \qquad 1.9$$

$$\text{Condensation: } 2\mathrm{M(OR)}_{x-m}(\mathrm{OH})_m \rightarrow (\mathrm{OH})_{m-1}(\mathrm{OR})_{x-m}\text{-M-O-M(OR)}_{x-m} + \mathrm{H_2O} \qquad 1.10$$

$$2\mathrm{M(OR)}_{x-m}(\mathrm{OH})_m \rightarrow (\mathrm{OH})_{m-1}(\mathrm{OR})_{x-m}\text{-M-O-M(OR)}_{x-m-1} + \mathrm{ROH} \qquad 1.11$$

$\mathrm{TiO_2}^{[53,\,93,\,94]}$ and α-$\mathrm{Fe_2O_3}^{[95]}$ nanoparticles with high photocatalytic activities have been synthesized successfully with sol-gel techniques from hydrolysis of a titanium or iron precursor, normally proceeding via an acid-catalyzed hydrolysis step metal alkoxide (*e.g.* isopropoxide) followed by condensation. The size of the final products can be tuned via the solution composition, pH, temperature and catalyst. Sometimes, the chelating agents, such as diol, carboxylic acid or diketonate compounds are used to control the hydrolysis process.[94]

For applications of solar energy conversion, crystallinity of photocatalyst is an important factor. Calcination is often required to improve the crystallinity and therefore the photoactivity

of powders prepared *via* sol-gel method. However, high temperature heat treatment would result in the agglomeration of nanocrystalline particles and rapid decrease of specific surface area. Much effort has been exerted to achieve highly crystallized and narrowly dispersed photocatalyst nanoparticles using the sol-gel method with modifications.[96]

It is worthy of noting that semiconductor nanocomposite used as photocatalyst could be obtained by sol-gel method in the presence of different metal precursors. For example, by adjusting the additive amount of Sr precursors into the TiO_2 sol, the composite of TiO_2-SrO composite powders was obtained.[97]

1.5.3 Microemulsion

A microemulsion is a thermodynamically stable isotropic dispersion of two immiscible liquids, where the microdomain of either or both liquids is stabilized by an interfacial film of surfactant molecules.[82] Such microemulsion can be used as microreactors where the photocatalyst nanostructures are synthesized as a production of reaction between solved cations and a precipitating agent. In normal micelles, the aqueous phase is surrounded by a monolayer of surfactant molecules with the hydrophobic hydrocarbon chains oriented toward the interior of the micelle. Reverse micelles can be formed in nonaqueous medium with the hydrophilic head-groups oriented to the interior of the micelle. The size and the shape of (reverse) micelle, which determines the morphology of the synthesized inorganic nanostructures, can be well controlled by the molar rate of surfactant to water, as well as the geometric factors of the surfactant.[98]

1.5.4 Hydrothermal Processing

The hydrothermal process is a suitable aqueous route to the synthesis of nanostructure inorganic materials used as photocatalysts. This method was first explored by mineralogist to simulate the formation process of minerals and rocks, and then was developed into a method for materials synthesis and treatment. Under hydrothermal condition, water acts as a reactant at supercritical conditions, accelerating the kinetics of the hydrolysis process of many inorganic substances. Ostwald ripening is allowed due to the increased mobility at a lower water viscosity, increasing the formation rate of precipitates. In terms of materials synthesis, the hydrothermal route was first applied in the field of single crystal growth and new materials synthesis.

Under hydrothermal condition, a large number of nanostructured inorganic materials can be synthesized. For example, TiO_2 nanoparticles can be obtained by hydrothermal treatment of peptized precipitates of titanium hydroxide.[35] The nanogel was prepared by adding a 28% NH_3

aqueous solution into 0.3 M $TiCl_4$ solutions until the pH 12. After water washing process, the pH of the nanogel dispersion was around 9.5 and subsequently hydrothermal crystallized at 200°C for 2~16 h. By analyzing the average crystal diameter along [100], [101] and [001] directions from XRD profile, it was found that the anatase crystals grow *via* four stages in solution. Small equidimensional anatase nanocrystals form in the first stage and then grow abruptly along [001] direction. The difference in growth rate along different directions leads to faceted shape evolution of anatase. Thus the area rate between {101} facet and {001} depends on hydrothermal treatment time and has influence on photoactivity of final products due to hydroxyl radial concentration anisotropy of various facets.

Size and morphological control in hydrothermal reactions could be achieved by controlling the time and temperature. Research work by Testino *et al.* proved that the crystal structure and morphology of well-faceted TiO_2 nanoparticles can be tuned by systematically changing the temperature, the pH, and the duration of the hydrothermal treatment.[99] The selection of the suitable experimental conditions was guided by thermodynamic modeling based on the available thermochemical data of TiO_2-H_2O-HCl-NH_3 system. The decrease in surface acidity was found to have a detrimental effect on photocatalytic activity due to the correlation between particle morphology and photocatalytic activity.

Solvothermal method, identical to hydrothermal method except that the solvent used is non-aqueous, has been found to be a versatile method for the synthesis of a large variety of nanoparticles with high photoactivity. Zhu *et al.* prepared α-Fe_2O_3 hollow spheres by using microwave solvothermal method from Fe(III) precursors in ethylene glycol (EG) solutions.[100] The surfactant of sodium dodecylbenzenesulfonate (SDBS) helps the growth of hematite nanosheets in the proposed reduction, dissolution and recrystallization process, and then the nanosheets assemble into hierarchical hollow spheres. The resulting hematite spheres exhibit improved photocatalytic property in removal capacity for methyl orange and salicylic acid in water treatment.

In solvothermal reactions, solubility, reactivity, and diffusion behavior of the reactants are influenced by the solvent used with different physical and chemical properties, determining the size, morphology and crystallization behavior of the final products.[101] The presence of ethanol at a high concentration not only can cause the polarity of the solvent to change but also strongly affects the ζ potential values of the reactant particles and the increases solution viscosity.

1.5.5 Co-Precipitation

As one of the oldest techniques for the synthesis of nanoparticles, co-precipitation is a mature industrial method for the production of many oxide powders. In a precipitation reaction, the metal precursors are dissolved in a common solvent and a precipitating agent is added to form an insoluble solid. The major advantage of precipitation reactions is that large quantities of particles can be synthesized, although the tailoring of the particle size and morphology is difficult.

Most oxide nanoparticles can be obtained directly by co-precipitation. Sintering is often needed to produce highly crystallized particles, especially for use as photocatalyst because crystallinity plays an important role in photoactivity.[22] However, agglomeration of nanoparticle may occur during sintering at high temperature, resulting in lower surface area and degraded photoactivity. Therefore, the selection of sintering temperature is crucial for obtaining nanoparticles with high photoactivity using co-precipitation. The group of Xu investigated the effect of sintering temperature on the photocatalytic activities of ferric oxide and silica-supported ferric oxide for orange II degradation in water under UV light irradiation.[21] As shown in Figure 1.7, the optimized sintering temperature is $500^{\circ}C$.

1.6   Motivation and Objectives

The development of new materials for solar energy conversion in the field of hydrogen generation and contaminants degradation has aroused both social and scientific concerns. Semiconductor based photocatalytic reactions are expected to be promising for environmental remediation. Since the first report by Honda and Fujishima on water splitting, TiO_2 has been in the central status in photocatalyst materials. However, the low utilization efficiency of TiO_2 for solar energy has always been the bottleneck of its wide application. Many scientific efforts have been made to enhance the visible light response of TiO_2, but the achievement is limited so far.

Iron oxide nanostructures are suitable semiconductor oxide to serve as photocatalyst absorbing photons from the blue and ultraviolet parts of the solar emission due to its band gap of 2.2 eV. The present work explores the synthesis of iron oxide with different morphologies that exhibits photoactivity in decomposing contaminants. The correlation between the functional groups of stabilizer molecules and iron oxide nanoparticles shapes was investigated. Using methyl orange as a probe molecule, the photocatalytic activity of iron oxide nanoparticles was systematically investigated, including the effect of dosage, pH, initial MO concentration, and addition of electron donor agent.

Reference

[1] Fujishima, A.; Honda, K. *Nature* **1972**, *238*, 37–38.

[2] Frank, S. N.; Bard, A. J. *J. Phys. Chem.* **1977**, *81*, 1484–1488.

[3] Chen, X.; Mao, S. S. *Chem. Rev.* **2007**, *107*(7), 2891–2959.

[4] http://www.coseti.org/highspec.htm.

[5] Asahi, R.; Morikawa, T.; Ohwaki, T.; Aoki, K.; Taga, Y. *Science* **2001**, *293*, 269–271.

[6] van de Krol, R.; Liang, Y.; Schoonman, J. *J. Mater. Chem.* **2008**, *18*(20), 2311–2320.

[7] Bott, A. W. *Curr. Sep.* **1998**, *17*, 87–91.

[8] Linsebigler, A. L.; Lu, G.; Yates Jr., J. T. *Chem. Rev.* **1995**, *95*, 735–758.

[9] Kabra, K.; Chaudhary, R.; Sawhney, R. *Ind. Eng. Chem. Res.* **2004**, *43*(24), 7683–7696.

[10] Alfano, O. M.; Cabrera, M. I.; Cassano, A. E. *J. Catal.* **1997**, *172*(2), 370–379.

[11] Liu, S.; Liu, H. *Photocatalysis and photoelectrocatalysis: Principles and applications;* Chemical industry press: Beijing, 2006.

[12] Hoffmann, M. R.; Martin, S. T.; Choi, W.; Bahnemann, D. W. *Chem. Rev.* **1995**, *95*(1), 69–96.

[13] Houas, A.; Lachheb, H.; Ksibi, M.; Elaloui, E.; Guillard, C.; Herrmann, J.-M. *Appl. Catal. B* **2001**, *31*, 145–157.

[14] Kesselman, J. M.; Weres, O.; Lewis, N. S.; Hoffmann, M. R. *J. Phys. Chem. B* **1997**, *101*(14), 2637–2643.

[15] Zhang, Z.; Wang, C.-C.; Zakaria, R.; Ying, J. Y. *J. Phys. Chem. B* **1998**, *102*(52), 10871–10878.

[16] Grätzel, M.; Frank, A. J. *J. Phys. Chem.* **1982**, *86*(15), 2964–2967.

[17] Burda, C.; Chen, X.; Narayanan, R.; El-Sayed, M. A. *Chem. Rev.* **2005**, *105*(4), 1025–1102.

[18] Xin, B.; Ding, D.; Gao, Y.; Jin, X.; Fu, H.; Wang, P. *Appl. Surf. Sci.* **2009**, *255*(11), 5896–5901.

[19] Nakamura, I.; Negishi, N.; Kutsuna, S.; Ihara, T.; Sugihara, S.; Takeuchi, K. *J. Mol. Catal. A: Chem.* **2000**, *161*(1-2), 205–212.

[20] Wu, J.-M.; Zhang, T.-W.; Zeng, Y.-W.; Hayakawa, S.; Tsuru, K.; Osaka, A. *Langmuir* **2005**, *21*(15), 6995–7002.

[21] Wang, Y.; Du, W.; Xu, Y. *Langmuir* **2009**, *25*, 2895–2899.

[22] Hermanek, M.; Zboril, R.; Medrik, I.; Pechousek, J.; Gregor, C. *J. Am. Chem. Soc.* **2007**, *129*, 10929–10936.

[23] Grätzel, M. *Nature* **2001**, *414*(6861), 338–344.

[24] Efros, A. L.; Rosen, M. *Annu. Rev. Mater. Sci.* **2000**, *30*, 475–521.

[25] Chen, D.; Ray, A. K. *Appl. Catal. B* **1999**, *23*(2-3), 143–157.

[26] Tabata, S.; Ohnishi, H.; Yagasaki, E.; Ippommatsu, M.; Domen, K. *Catal. Lett.* **1994**, *28*, 417–422.

[27] Bahnemann, D.; Bockelmann, D.; Goslich, R. *Solar Energy Materials* **1991**, *24*(1-4), 564–583.

[28] Yao, W. F.; Xu, X. H.; Wang, H.; Zhou, J. T.; Yang, X. N.; Zhang, Y.; Shang, S. X.; Huang, B. B. *Appl. Catal. B* **2004**, *52*(2), 109–116.

[29] He, J.; Ma, W.; Song, W.; Zhao, J.; Qian, X.; Zhang, S.; Yu, J. C. *Water Res.* **2005**, *39*(1), 119–128.

[30] Al-Qaradawi, S.; Salman, S. R. *J. Photochem. Photobiol. A* **2002**, *148*(1-3), 161–168.

[31] Pan, Z.; Somasundaran, P.; Turro, N. J.; Jockusch, S. *Colloids and Surfaces A: Physicochemical and Engineering Aspects* **2004**, *238*(1-3), 123 – 126.

[32] Litter, M. I. *Appl. Catal. B* **1999**, *23*(2-3), 89–114.

[33] Henderson, M. A.; Epling, W. S.; Peden, C. H. F.; Perkins, C. L. *J. Phys. Chem. B* **2003**, *107*(2), 534–545.

[34] Arrouvel, C.; Digne, M.; Breysse, M.; Toulhoat, H.; Raybaud, P. *J. Catal.* **2004**, *222*(1), 152–166.

[35] Cho, C. H.; Han, M. H.; Kim, D. H.; Kim, D. K. *Mater. Chem. Phys.* **2005**, *92*, 104–111.

[36] Faust, B. C.; Hoffmann, M. R.; Bahnemann, D. W. *J. Phys. Chem.* **1989**, *93*, 6371–6381.

[37] Wang, Y.; Hong, C.-S. *Water Res.* **2000**, *34*(10), 2791–2797.

[38] Du, W.; Xu, Y.; Wang, Y. *Langmuir* **2008**, *24*, 175–181.

[39] Qiu, X.; Li, L.; Zheng, J.; Liu, J.; Sun, X.; Li, G. *J. Phys. Chem. C* **2008**, *112*(32), 12242–12248.

[40] Mohapatra, S. K.; Raja, K. S.; Mahajan, V. K.; Misra, M. *J. Phys. Chem. C* **2008**, *112*(29), 11007–11012.

[41] Yamada, K.-i.; Mukaihata, N.; Kawahara, T.; Tada, H. *Langmuir* **2007**, *23*, 8593–8596.

[42] Chen, J.-N.; Chan, Y.-C.; Lu, M.-C. *Water Sci. Technol.* **1999**, *39*(10-11), 225 – 230.

[43] Abdullah, M.; Low, G. K. C.; Matthews, R. W. *J. Phys. Chem.* **1990**, *94*(17), 6820–6825.

[44] Grätzel, M.; Howe, R. F. *J. Phys. Chem.* **1990**, *94*(6), 2566–2572.

[45] Kleiman-Shwarsctein, A.; Hu, Y.-S.; Forman, A. J.; Stucky, G. D.; McFarland, E. W. *J. Phys. Chem. C* **2008**, *112*, 15900–15907.

[46] Hu, Y.-S.; Kleiman-Shwarsctein, A.; Forman, A. J.; Hazen, D.; Park, J.-N.; McFarland, E. W. *Chem. Mater.* **2008**, *20*(12), 3803–3805.

[47] Kumari, S.; Singh, A. P.; Tripathi, C.; Chauhan, D.; Dass, S.; Shrivastav, R.; Gupta, V.; Sreenivas, K.; Satsangi, V. R. *Int. J. Photoenergy* **2007**, *2007*, 87467.

[48] Burda, C.; Lou, Y.; Chen, X.; Samia, A. C. S.; Stout, J.; Gole, J. L. *Nano Lett.* **2003**, *3*(8), 1049–1051.

[49] Khan, S. U. M.; Al-Shahry, M.; Ingler Jr., W. B. *Science* **2002**, *297*, 2243–2245.

[50] Yu, J. C.; Yu, J.; Ho, W.; Jiang, Z.; Zhang, L. *Chem. Mater.* **2002**, *14*, 3808–3818.

[51] Gopal, N. O.; Lo, H.-H.; Ke, S.-C. *J. Am. Chem. Soc.* **2008**, *130*(9), 2760–2761.

[52] Begum, N. S.; Ahmed, H. M. F.; Hussain, O. M. *Bull. Mater. Sci.* **2008**, *31*(5), 741–745.

[53] Zaleska, A.; Sobczak, J. W.; Grabowska, E.; Hupka, J. *Appl. Catal. B* **2008**, *78*(1-2), 92–100.

[54] Goldstein, S.; Behar, D.; Rabani, J. *J. Phys. Chem. C* **2008**, *112*(39), 15134–15139.

[55] Rosso, K. M.; Smith, D. M. A.; Dupuis, M. *J. Chem. Phys.* **2003**, *118*(14), 6455–6466.

[56] Glasscock, J. A.; Barnes, P. R. F.; Plumb, I. C.; Savvides, N. *J. Phys. Chem. C* **2007**, *111*(44), 16477–16488.

[57] Cesar, I.; Sivula, K.; Kay, A.; Zboril, R.; Grätzel, M. *J. Phys. Chem. C* **2009**, *113*(2), 772–782.

[58] Liang, Y.; Enache, C. S.; van de Krol, R. *Int. J. Photoenergy* **2008**, *2008*, 739864.

[59] Cesar, I.; Kay, A.; Gonzalez Martinez, J. A.; Grätzel, M. *J. Am. Chem. Soc.* **2006**, *128*(14), 4582–4583.

[60] Yanina, S. V.; Rosso, K. M. *Science* **2008**, *320*, 218–222.

[61] Lu, W.; Gao, S.; Wang, J. *J. Phys. Chem. C* **2008**, *112*(43), 16792–16800.

[62] Lu, W.; Liu, G.; Gao, S.; Xing, S.; Wang, J. *Nanotechnology* **2008**, *19*(44), 445711.

[63] Jakob, M.; Levanon, H.; Kamat, P. V. *Nano Lett.* **2003**, *3*(3), 353–358.

[64] Kamat, P. V. *J. Phys. Chem. B* **2002**, *106*(32), 7729–7744.

[65] Hirakawa, T.; Kamat, P. V. *J. Am. Chem. Soc.* **2005**, *127*(11), 3928–3934.

[66] Subramanian, V.; Wolf, E.; Kamat, P. V. *J. Phys. Chem. B* **2001**, *105*(46), 11439–11446.

[67] Carp, O.; Huisman, C. L.; Reller, A. *Prog. Solid State Chem.* **2004**, *32*(1-2), 33–177.

[68] Xiong, G.; Joly, A. G.; Holtom, G. P.; Wang, C.; McCready, D. E.; Beck, K. M.; Hess, W. P. *J. Phys. Chem. B* **2006**, *110*(34), 16937–16940.

[69] O'Regan, B.; Grätzel, M. October **1991**, *353*(6346), 737–740.

[70] Kamat, P. V. *J. Phys. Chem.* **1989**, *93*(2), 859–864.

[71] Polo, A. S.; Itokazu, M. K.; Iha, N. Y. M. *Coord. Chem. Rev.* **2004**, *248*, 1343–1361.

[72] Hagfeldt, A.; Grätzel, M. *Chem. Rev.* **1995**, *95*(1), 49–68.

[73] Koenenkamp, R.; Henninger, R.; Hoyer, P. *Journal of Physical Chemistry* **1993**, *97*(28), 7328–7330.

[74] Yang, S.; Liu, Y.; Sun, C. *Appl. Catal. A* **2006**, *301*(2), 284 – 291.

[75] Gao, Z.; Yang, S.; Ta, N.; Sun, C. *J. Hazard. Mater.* **2007**, *145*(3), 424 – 430.

[76] Duret, A.; Grätzel, M. *J. Phys. Chem. B* **2005**, *109*(36), 17184–17191.

[77] Kawahara, T.; Yamada, K.; Tada, H. *J. Colloid Interface Sci.* **2006**, *294*, 504–507.

[78] Cudennec, Y.; Lecerf, A. *Solid State Sci.* **2005**, *7*, 520–529.

[79] Matsumoto, Y. November **1996**, *126*(2), 227–234.

[80] Trainor, T. P.; Chaka, A. M.; Eng, P. J.; Newville, M.; Waychunas, G. A.; Catalano, J. G.; Brown Jr., G. E. *Surf. Sci.* **2004**, *573*, 204–224.

[81] Yan, B.; Tao, J.; Pang, C.; Zheng, Z.; Shen, Z.; Huan, C. H. A.; Yu, T. *Langmuir* **2008**, *24*(19), 10569–10571.

[82] Eastoe, J.; Hollamby, M. J.; Hudson, L. *Adv. Colloid Interface Sci.* **2006**, *128-130*, 5–15.

[83] Sun, Y.; Xia, Y. *Science* **2002**, *298*, 2176–2179.

[84] Yin, Y.; Alivisatos, A. P. *Nature* **2005**, *437*(7059), 664–670.

[85] Saponjic, Z. V.; Dimitrijevic, N. M.; Tiede, D. M.; Goshe, A. J.; Zuo, X.; Chen, L. X.; Barnard, A. S.; Zapol, P.; Curtiss, L.; Rajh, T. *Adv. Mater.* **2005**, *17*, 965–971.

[86] Jun, Y.-w.; Casula, M. F.; Sim, J.-H.; Kim, S. Y.; Cheon, J.; Alivisatos, A. P. *J. Am. Chem. Soc.* **2003**, *125*, 15981–15985.

[87] Lee, S.-M.; Cho, S.-N.; Cheon, J. *Adv. Mater.* **2003**, *15*, 441–444.

[88] Lee, S.-M.; Jun, Y.-W.; Cho, S.-N.; Cheon, J. *J. Am. Chem. Soc.* **2002**, *124*(38), 11244–11245.

[89] Chen, J.; Herricks, T.; Xia, Y. *Angew. Chem. Int. Ed.* **2005**, *44*, 2589–2592.

[90] Cha, S. I.; Mo, C. B.; Kim, K. T.; Jeong, Y. J.; Hong, S. H. *J. Mater. Res.* **2006**, *21*(9), 2371–2378.

[91] Hu, X.; Yu, J. C. *Adv. Funct. Mater.* **2008**, *18*, 880–887.

[92] Vayssieres, L. *Int. J. Nanotechnol.* **2004**, *1*(1), 1–41.

[93] Jung, C.-K.; Bae, I.-S.; Song, Y.-H.; Boo, J.-H. *Surf. Coat. Technol.* **2005**, *200*(5-6), 1320–1324.

[94] Su, C.; Hong, B.-Y.; Tseng, C.-M. *Catal. Today* **2004**, *96*(3), 119 – 126.

[95] Woo, K.; Lee, H. J.; Ahn, J.-P.; Park, Y. S. *Adv. Mater.* **2003**, *15*(20), 1761–1764.

[96] Znaidi, L.; Séraphimova, R.; Bocquet, J. F.; Colbeau-Justin, C.; Pommier, C. *Mater. Res. Bull.* **2001**, *36*(5-6), 811 – 825.

[97] Han, J.-K.; Choi, S.-M.; Lee, G.-H. *Mater. Lett.* **2007**, *61*(18), 3798–3801.

[98] Pileni, M.-P. *Nat. Mater.* **2003**, *2*, 145–150.

[99] Testino, A.; Bellobono, I. R.; Buscaglia, V.; Canevali, C.; D'Arienzo, M.; Polizzi, S.; Scotti, R.; Morazzoni, F. *J. Am. Chem. Soc.* **2007**, *129*(12), 3564–3575.

[100] Cao, S.-W.; Zhu, Y.-J. *J. Phys. Chem. C* **2008**, *112*(16), 6253–6257.

[101] Zeng, S.; Tang, K.; Li, T.; Liang, Z.; Wang, D.; Wang, Y.; Qi, Y.; Zhou, W. *J. Phys. Chem. C* **2008**, *112*(13), 4836–4843.

Chapter 2 Preparation and Growth Mechanism of Iron Oxide Nanoparticles with Different Morphologies

2.1 Introduction

The unique properties of nanoparticles, in comparison with their bulk counterparts, make them useful for applications in materials or devices, such as catalysts, sensors, and contrast agents. For many applications, the overall control on structure and morphology for regular shape and homogeneous size distribution is critical because physical and chemical properties of nanosized materials are highly sensitive to morphology, crystal structure and defects.[1-3] One well-known example for a morphology dependent property is the catalytic property of the inorganic nanoparticles. By controlling the shape at the nanometer level, the proportion of the crystallographic planes, and the number of atoms on corners and edges positions can be well tuned, which means the coordination of surface atoms could be controlled as a result. Accordingly, nanoparticles with well-defined morphologies have potential applications as catalyst.

The morphology control of iron oxide nanoparticles can be accomplished by adjusting the growing space. In hydrothermal process, controlling the size and shape is done by adjusting the ratio of the concentration of the chemical agents making the nanoparticle to that of the selected capping agents. Although the synthesis of many oxide nanoparticles have reported by using hydrothermal method, the crystal growth mechanism, especially the correlation between shape evolution and adding agents, needs further investigation. In addition, from the practical viewpoint, the exploration of a simple, easy to scale-up and soft chemical (*chimie douce*) route to fabricate nanoparticles with well-defined morphologies is still a long-term challenge.

There has been a long history on crystal research of their equilibrium morphology. Some proposed models could be used a reference to explain the shape evolution in nanoscale. The basic thermodynamic concepts of crystal growth were formulated in 1878 by Gibbs in his remarkable work 'On the Equilibrium of Heterogeneous Systems', stating that the surface energy of a crystal is minimized at its equilibrium state. Later it was revised by Currie and Wulff and became the famous 'Theorem of Gibbs-Currie-Wulff'.[4] According to that theorem, the equilibrium shape of a nanocrystal with a volume of V can be given by:

$$\frac{\Gamma_{hkl}}{d_{hkl}} = \alpha \qquad \forall \ h, k, l, \qquad\qquad 2.1$$

in which Γ_{hkl} represents the surface area of (hkl) facet, d_{hkl} represents the distance from the crystal center to the surface along normal direction of (hkl). α is a constant. In 1951, Herring proposed the thermodynamic criteria aimed at crystals of polyhedral and spherical shapes.[5] However, the growth morphologies of particles with small diameter can not be well predicted by using this criterion.

Barnard predicted the shape of nanocrystals based on Wulff's rule.[6, 7] Believing that the deference between prediction and experimental results originates from the predigesting of the expression of the crystal free energy, she suggested that the surface tension, edge energy, and corner energy should also be taken into account. Thus the Gibbs free energy of nanocrystal of material x can be expressed as:

$$G_x^0(T) = G_x^{bulk} + G_x^{surface} + G_x^{edge} + G_x^{corner}$$

$$= \Delta_f G_x^0(T) + \frac{M}{\rho_x}\left[q\sum_i f_i \gamma_{xi}(T) + p\sum_j g_j \lambda_{xj}(T) + w\sum_k h_k \varepsilon_{xk}(T) \right] \qquad 2.2$$

in which the first term $\Delta_f G_x^0(T)$ is the standard free energy of formation of x, M is the molar mass and the density of x is ρ_x, γ_x is the surface free energy, λ_x and ε_x are edge and corner free energy. f_i, g_j, and h_k are the weighting factors, respectively. Considering the pressure on particle produced by surface tension, the above formula become

$$G_x^0(T) = \Delta_f G_x^0(T) + \frac{M}{\rho_x}(1-e)\left[q\sum_i f_i \gamma_{xi}(T) + p\sum_j g_j \lambda_{xj}(T) + w\sum_k h_k \varepsilon_{xk}(T) \right] \quad 2.3$$

in which $e = \Delta V / V$ represents the volume compressive effect caused by surface tension.

In summary, the above theoretical research concludes that the morphology of inorganic nanoparticles can be determined by crystal structure, surface energy and tension. For nanoparticle obtained by wet chemical route, the surfactant with different functional groups
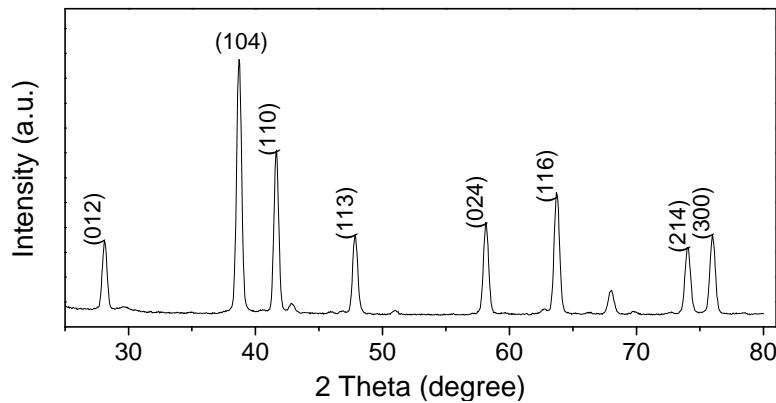

Figure 2.1 XRD spectrum of the hematite synthesized by hydrothermal method.

may serve as stabilizer of crystallographic planes during crystal growth by tailing the solid-solution interfacial energy. In this chapter, three simple capping molecules (urea, 3-aminopropanol, and polyethylene glycol) with different functional groups ($-NH_2$ for urea, $-NH_2$ and $-OH$ for 3-aminopropanol, and $-O-$ for polyethylene glycol) have been designed to prepared iron oxide particles with various shapes.

2.2   Experimental

2.2.1 Sample Preparation

Three forms of iron oxide, including $\alpha\text{-}Fe_2O_3$, Fe_3O_4, and $\alpha\text{-}FeOOH$ were synthesized using hydrothermal method. Ferric and ferrous chloride ($FeCl_3 \cdot 6H_2O$, $FeCl_2 \cdot 4H_2O$), urea, 3-aminopropanol, polyethylene glycol (PEG 4k and PEG 20k), and NaOH were used as starting chemical reagents. All chemicals (AR grade) were purchased from Shanghai Chemical Reagent Co., Ltd. and were used as received.

A typical hydrothermal synthesis for $\alpha\text{-}Fe_2O_3$ nanoparticles is as follows: (1) 1.351g analytically pure $FeCl_3 \cdot 6H_2O$ and 1.0 g urea were dissolved in 30 mL H_2O with continuous stirring. Then, 5 M NaOH solution was added dropwise to the above solution under vigorous stirring. A red precipitation appeared immediately after the NaOH was added. (2) After being stirred for another 20 min, the solution was transferred and sealed in a 120 mL Teflon-sealed autoclave. (3) The autoclave was kept at a fixed temperature for a time duration before cooled in air naturally. (4) The final products were separated from the reaction medium by centrifugation and then washed by deionized water and alcohol by three cycles before oven drying at 55°C for 20 hours.

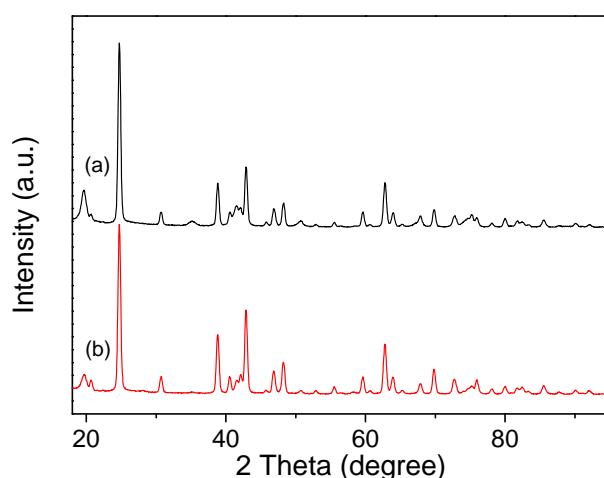Fe_3O_4 nanoparticles were synthesized by hydrothermal method in a similar procedure to that

Figure 2.2 XRD patterns of α-FeOOH nanorods fabricated from different iron sources. (a) Fe^{3+}, (b) $Fe^{2+}+Fe^{3+}$.
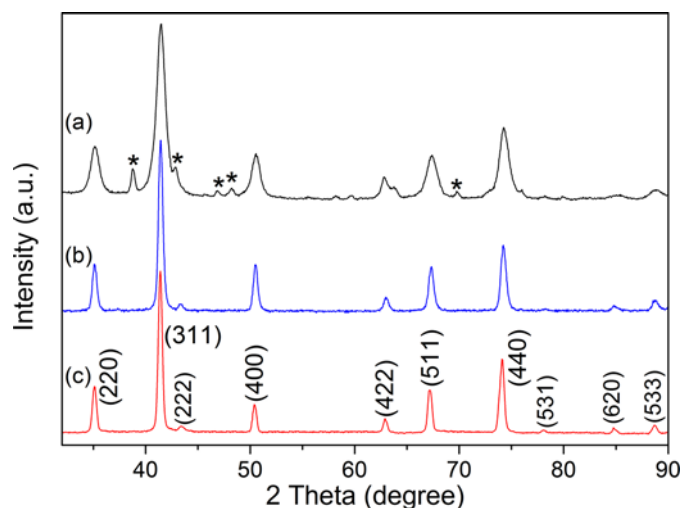
Figure 2.3 XRD patterns of magnetite synthesized with three stabilizers: (a) 3-aminopropanol; (b) PEG; (c) urea. The small peaks marked by asterisks on the curve (a) are assigned to goethite.

of α-Fe_2O_3, except that mixed solution of Fe^{2+} and Fe^{3+} in molar ratio of 1.8:1 was used as reaction precursor solution. Besides, in order to prevent the excess oxidation of Fe^{2+}, the operation was carried under N_2 flow.

Hydrothermal synthesis of α-FeOOH: First 0.01 mol $FeCl_3$ and 1.0 g PEG 4k was dissolved in 100 mL deionized water, and then was added 4.0 g NaOH under vigorous stirring. The color of the solution became dark brown and the stirring was kept for another 20 min. Subsequently, the slurry was transferred into a 120 mL autoclave and was hold at 120℃ for 10 hours. The research of Gilbert *et al.* showed that Fe^{2+} cation in solutions plays a catalytic role in the transformation process from ferrihydrite to α-FeOOH and thus could accelerate the formation rate of α-FeOOH.[8] Therefore, in this work, equimolar (0.005 mol) of $FeCl_3$ and $FeCl_2$ were used as starting materials to fabricate goethite nanorod. The precursor solution was vigorous stirred in air for 1 hour to ensure the sufficient oxidation of Fe^{2+}.

2.2.2 Characterization of Samples

The crystalline phase and structure of the products were characterized on a Philips X'Pert Pro X-ray diffractometer (XRD, the Netherlands), using Co K_α radiation (λ=0.17903 nm). The morphology of products was observed on a JEOL 6500F scanning electron microscope (SEM) and a Philips CM 200 transmission electron microscope (TEM). A small amount of nanoparticles were milled with KBr and then pressed into a disc for Fourier transform infrared (FTIR) analysis (Spectrum 100, Perkin Elmer, MA) in order to investigate the surface properties of as-synthesized samples. The magnetic properties of the magnetite nanoparticles were measured on a Lake Shore 7407 vibrating sample magnetometer (VSM) at room temperature.
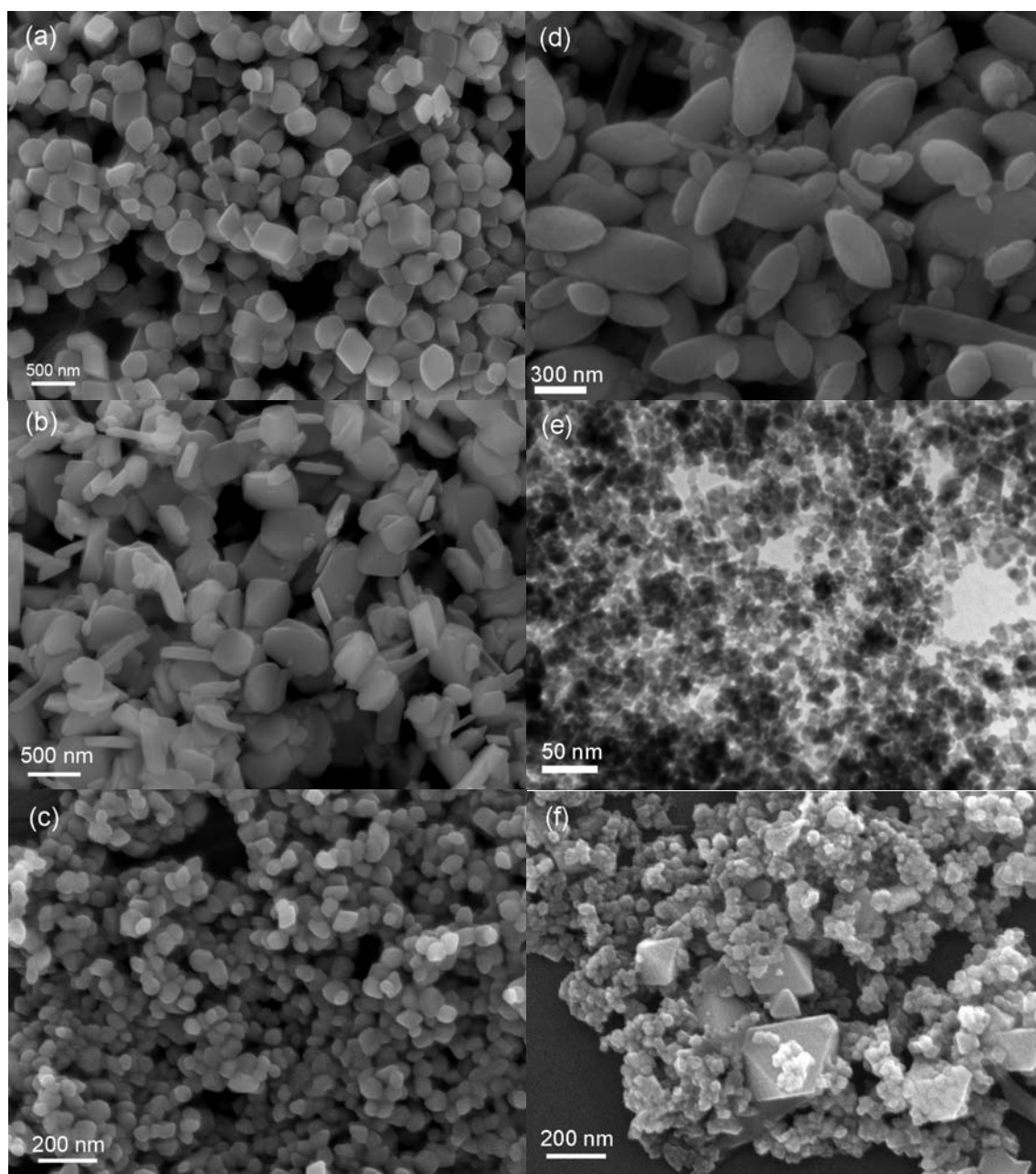
Figure 2.4 Electron microscopy images of iron oxide synthesized at 200°C for 10 hours: hematite nanoparticles synthesized with urea (a, SEM), aminopropanol (b, SEM) and PEG (c, SEM); magnetite particles synthesized with urea (d, SEM), aminopropanol (e, TEM) and PEG (f, SEM).

2.3   Results and Discussion

2.3.1 Structure and Morphology

Figures 2.1-3 show the XRD patterns of the products obtained by using hydrothermal route. All the diffraction peaks in Figure 2.1 are well indexed to a pure corundum structure of hematite (Space group $R\bar{3}c$, JCPDS No. 33-0664). No peak related to the other phases of iron compound was found in Figure 2.1, indicating that the as-obtained hematite nanoparticles have a high purity. Besides, the broadening of the peaks to some extent was found in the spectra, which may
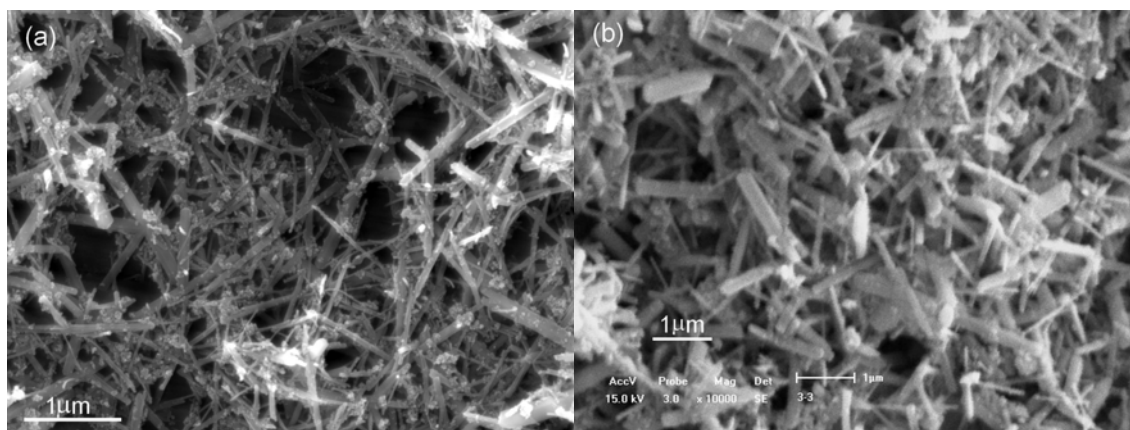
Figure 2.5 SEM images of goethite nanorods synthesized from starting reagents of (a) equimolar FeCl$_3$ and FeCl$_2$ and (b) only FeCl$_3$ as iron source. Scale bar in inset (a): 100nm.

be caused by the reduction in crystal size. The morphological information of hematite nanoparticles was investigated by SEM.

The SEM images in Figure 2.4(a-c) show the morphological characteristics of as-synthesized hematite products at 200°C for 10 hours. From the images we can conclude that the added stabilizers not only influence the size distributions of the product particles but also change the growth rates of different crystallographic facets. It is believed that the shape variation is the result of growth competition between crystallographic planes which could be greatly influenced by the interaction between the functional group of stabilizer molecules and crystal surface. For hematite synthesized with urea, the nanoparticle shape is of polyhedron with edge length about 300 nm. In contrast, the particles synthesized with aminopropanol are of polygonal nanoplates with a variable thickness of about 60 nm. The shapes of hematite nanoparticles changed into spherical when PEG was used as stabilizer while the other synthesis conditions remained the same.

Fe$_3$O$_4$ with high purity can be obtained by hydrothermal treatment by using the iron precursors with PEG and urea as stabilizer. No obvious impurity phase can be detected from spectra of magnetite obtained with PEG or urea (Figure 2.3). Small peaks attributed to goethite can be found in the XRD spectrum of nanoparticles with the aminopropanol. It may be noted that the XRD peaks in Figure 2.3(a) are broader than that in Figure 2.3(b) and (c), implying that the crystal size of particles synthesized with 3-aminopropanol are evidently smaller than that synthesized with PEG or urea as capping agent. The estimated crystal diameter from the width broadening of the XRD peaks with Scherrer's equation is 11.5 nm which is in good agreement with TEM result. It should be noted that the primary crystal size values calculated from Scherrer's equation for magnetite synthesized with urea and PEG 20K are 28.8 and 23.7 nm
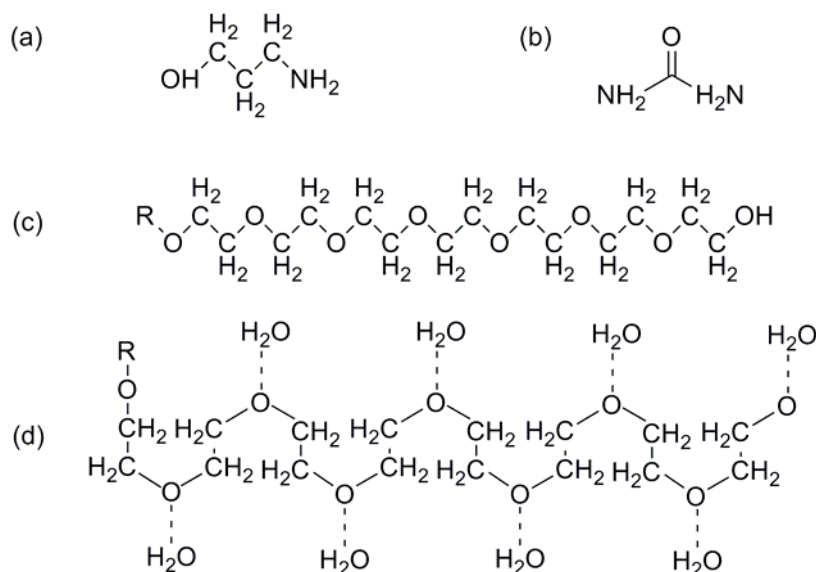
Figure 2.6 Molecular structure of stabilizers used in this thesis: (a) 3-aminiproponal; (b) urea; (c) solid state PEG; (d) PEG in water solutions.

which are obviously smaller than that shown in SEM images, implying that the particles are aggregated from primary particles.

Because the particle size of Fe_3O_4 is very small due to high polarity of 3-aminopropanol molecules, it is easy to be oxidized, causing the formation of the impurity phase α-FeOOH. From the corresponding electron microscopy images, one can see that the capping agent also influences the morphologies of magnetite, although the influencing rules are different from that in the case of hematite synthesis. Rice-shaped Fe_3O_4 with diameter less than 300 nm formed with the urea as surfactant. While 3-aminopropanol strongly hindered the growth of magnetite, leading to a great reduction in magnetite crystals size to about 10 nm which is in agreement with the above calculation from XRD. What is interesting is that when PEG 4k was used as surfactant, the product is composed of two kinds of nanoparticles with bimodal size distributions: one is nanoparticles with diameter below 75 nm; the other is tetrahedral and octahedral particles with an edge length of about 300 nm.

Figure 2.2 shows the XRD spectra of α-FeOOH nanorods synthesized from different iron cations. All diffraction peaks can be indexed to orthorhombic structure of α-FeOOH (JCPDS No. 29-0713). No other noticeable peaks induced by impurities can be observed in the XRD profiles. It has been reported[8] that goethite can form *via* the oxidation of ferrous compounds precipitated by mixing sodium hydroxide and ferrous salts solution, and the ferrous ions in reaction system may play a catalytic role to promote the formation of goethite. The representative SEM images of the as-synthesized powders are shown in Figure 2.5 which clearly reveals

that one-dimensional goethite nanorods were both obtained through the two methods. For products synthesized with equimolar ferrous and ferric ions, the products are nanorods with a width of 50-100 nm and a length of over 1 μm. In case of ferric ions used as iron source, the shape of the products remains the same except that the size of as-synthesized nanorods is larger than that in Figure 2.5(a).

2.3.2 Hydrothermal Growth Mechanism of Iron Oxide

Growth mechanism of α - Fe_2O_3 of different shapes

Figure 2.7 shows the representative TEM images of the hematite nanoplate and polyhedron, and their corresponding SAED patterns, revealing the single crystalline characteristics of the products. To further investigate the microstructure of surface facets, high-resolution TEM image was taken on the edge of the nanoparticle in Figure 2.7(a) and (b). Figure 2.7(c) illustrates the HRTEM image at the edge of hematite plate (the circled part in Figure 2.7(a)). The parallel lattice fringes spacing was measured to be about 0.421nm, corresponding to *d*-spacing of the $(0\bar{1}1)$ plane (0.4156 nm). From the HRTEM image, we can clearly see regular terrace and kinks on the outer surface of the nanocrystal. The vicinal plane that is consisted of the step edge acts the surface facet of the particle. The measured angle between the facet and $(0\bar{1}1)$ plane (19.6°) fits the one between the $(0\bar{1}1)$ and $(\overline{37}4)$ which indicate that the facet plane of the particle is $(\overline{37}4)$ plane.

The HRTEM images (Figure 2.7) on the edge of a typical hematite polyhedron synthesized with urea were give detailed structural information. The fringes spacing is 0.365 nm which is corresponding to the (012) plane. Many clusters under 3nm can be seen from the contrast of image and there are some terraces, steps and kinks existing in the image, indicating that the growth mechanism of oriented attachment on the terrace. In addition, the parallel fringes inside the crystal are perfect, supporting that the nanoclusters attached on the terrace in the same orientation, that is, oriented attachment.

Under the hydrothermal conditions, α - Fe_2O_3 formation proceeds through the following three steps:

$$Fe^{3+}+3OH^{-1} \rightarrow Fe(OH)_3 \rightarrow \beta - FeOOH \rightarrow \alpha - Fe_2O_3 \qquad 2.4$$

Fe^{3+} exists in the form of octahedral $[Fe(H_2O)_6]^{3+}$ complex in acidic environment or in the form of $[Fe(OH)_4]^-$ in basic environment. Depending on the pH of the solution, monomeric $[Fe(H_2O)_{6-n}(OH)_n]^{(3-n)+}$ form hydrolytic polymers in which Fe(III) cations are bridged by OH^- groups (olation) or O^{2-} ions (oxolation). The oxolation reaction, containing the proton transfer process which need a high active energy ($\Delta G'_0$=20 kJ·mol^{-1}), is thus considered to be
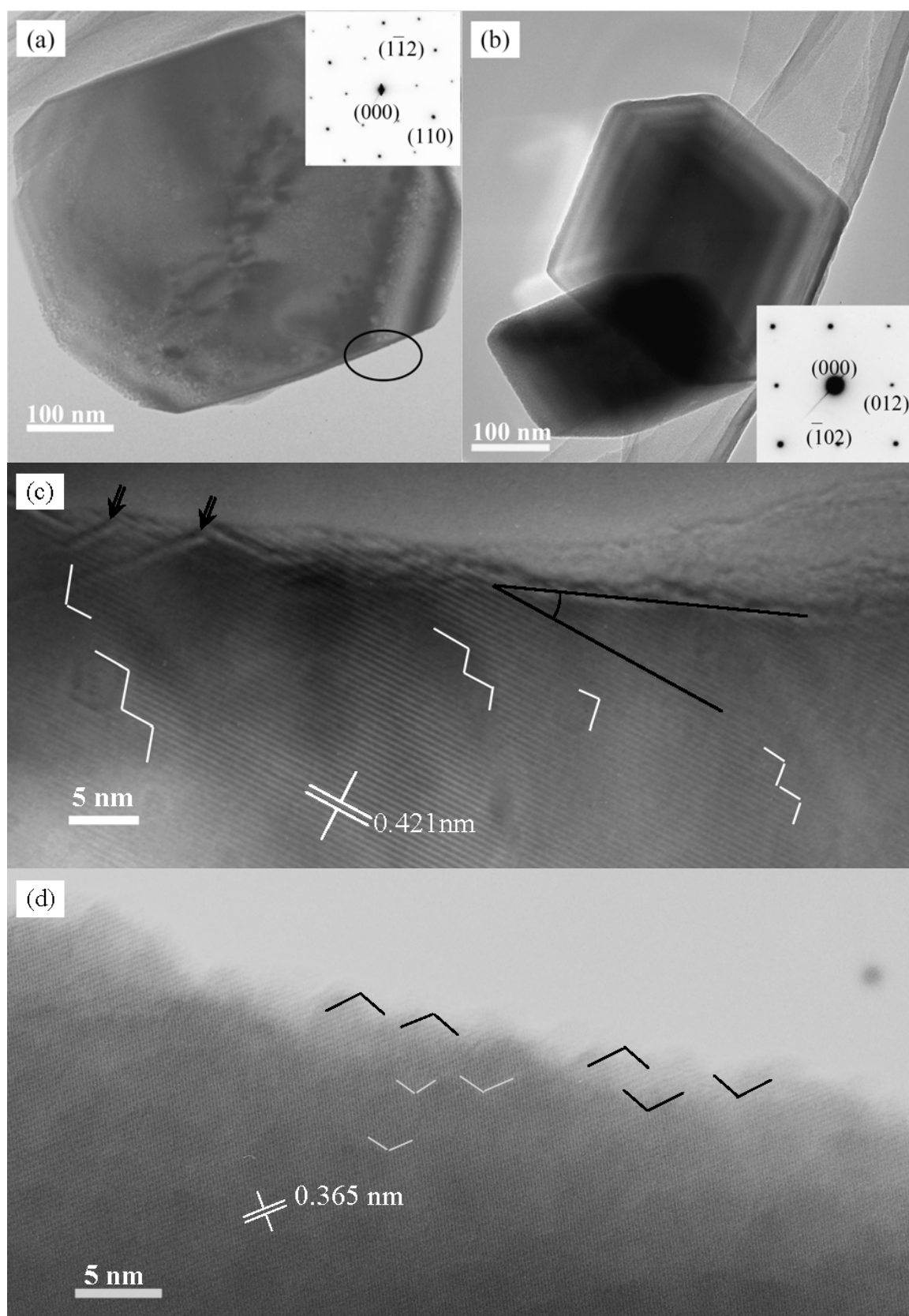
Figure 2.7 TEM images of hematite synthesized with (a) aminopropanol and (b) urea. HRTEM images on the edge of (c) plate shaped and (d) polyhedron shaped α-Fe$_2$O$_3$ nanoparticles.

much slower than the olation reaction. Therefore, Fe^{3+} ions form tetrahedral structured $[Fe_4O(OH)_{12}(OH_2)_4]^0$ mainly through olation process and form β-FeOOH through further olation process. Finally, the α-Fe$_2$O$_3$ crystals from as a result of topotactic transformation of the resulted β-FeOOH precursors.[9]

Use of organic molecules with different functional groups as stabilizers could hinder the olation process or crystal growth along a specific direction of α-Fe$_2$O$_3$ crystals by selective binding to nanocrystal facets, resulting in shape changes of hematite nanocrystals.[87, 88] In this work, three simple molecules were used as capping agents, whose structure was depicted in Figure 2.6. From the structure diagram, one can see that 3-aminopropanol molecule has an end-functional group of $-NH_2$, in witch there is a N atom containing unshared pair electrons and can chelate with Fe cations by forming AMP-Fe^{3+}. The symmetric structure of urea molecules is in favor of symmetric adsorption of urea on hematite surface.[12] As shown in Figure 1.8, α-Fe$_2$O$_3$ has a hexagonal corundum structure. Along the [0001] axis, layers of iron and oxygen stack in the order of $-Fe\text{-}Fe\text{-}O_3 - Fe\text{-}Fe\text{-}O_3 -$.[13] The dependence of hydroxyl configuration on crystals planes[14, 91] leads to changes in adsorption of capping agent on hematite surface.

The HRTEM observation in Figure 2.7 provides an explanation for the growth of faceted hematite nanocrystals by the terrace-step-kink mechanism *via* the adherence-surface diffusion-oriented attachment of each growth unit. In solvent, the hydrolyzed Fe^{3+} ions exist as $[Fe(OH_2)_6]^{3+}$ complex in acid environment or $[Fe(OH)_4]^-$ complex in basic environment through olation or oxolation. The complexes aggregate together to form nanoclusters as the growth units during the hydrothermal coarsening process of hematite particles according to the following steps [Eq. 2.5][16]: first, the Fe^{3+} complexes are combined with each other to form ferrihydrite nanoclusters, and then the resulted ferrihydrite transforms into α-Fe$_2$O$_3$ via the terrace-step-kink mechanism.

$$Fe^{3+} \rightarrow ferrihydrite \rightarrow \alpha - Fe_2O_3 \qquad\qquad 2.5$$
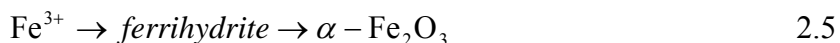
The growth process is schematically illustrated in Figure 2.8. The added surfactant molecules may be bound with the growth units and crystal facet due to electrostatic interaction. For oxide inorganic crystals, the in-plane atomic configuration and atomic layer sequence along their normal direction are different and determine their surface charging properties.[14, 80] Therefore, the surfactant molecule adsorption position and geometric configuration might differ resulting from the diversity of interacting functional groups and facet charging properties. In addition, depending on the electronic structure of functional group, the adsorbate molecules
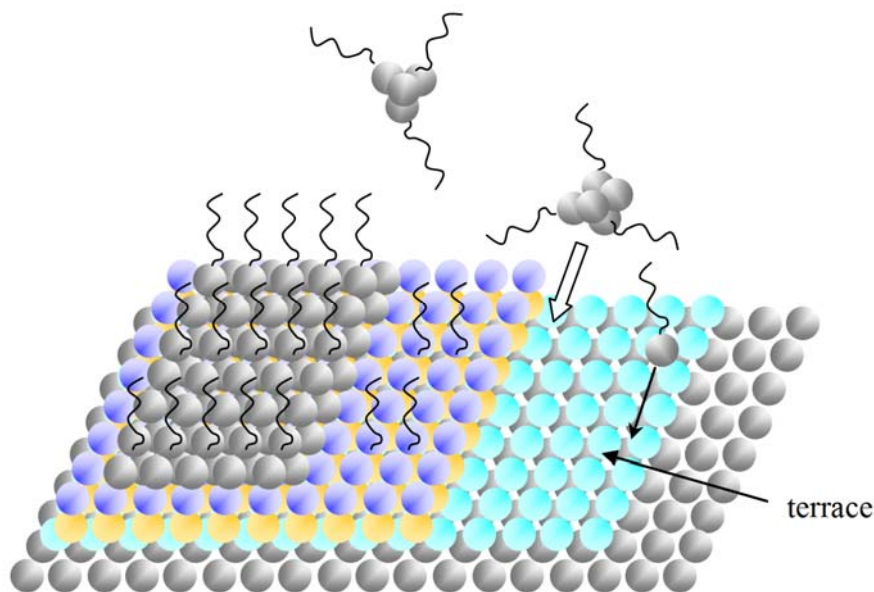
Figure 2.8 Schematic diagram of the proposed growth mechanism: exchange of stabilizer co-ordinated ions on crystal surface and surface diffusion on low-index plane.

can induce surface reconstruction by forming step edge alignment.[18] Thus a surfactant stabilized high-index facet forms on the low-index terrace planes and the kink sites can act as the active place for further growth. In this work, the amino- group of 3-aminopropanol was bound to the negative charged plane while urea was symmetrically bound to the crystal surface by C=O bond, as reported in Ref.[12]. Adsorbate capped nanoclusters of hematite can locate on these kink sites by oriented attachment driven by surface energy or magnetic energy.[19]

Hydrothermal growth mechanism of Fe₃O₄ of different morphologies

The crystallographic symmetry of Fe_3O_4, with a cubic spinel crystal structure, is higher than that of $\alpha\text{-}Fe_2O_3$ and the arrangement of Fe cations and O anions are very different. Under hydrothermal conditions, Fe_3O_4 can be obtained through reactions as follows,[20]

$$Fe[H_2O]_6^{2+} + Fe[H_2O]_6^{3+} + OH^- \rightarrow Fe(OH)_2 + Fe(OH)_3 \rightarrow Fe_3O_4 \qquad 2.6$$
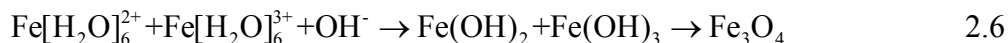
The shape evolution of nanoparticles in presence of capping agent originates from confined preferential crystal growth caused by added capping molecules and synthesis conditions. As a result of surface energy minimization, the particle shapes are closely related to the growth rate of the exposed surface planes. Capping molecules may selectively bind to different planes of a growing crystal by their end functional group when they are added into the synthesis medium.[88] The binding energy is determined by the electronic structure and spatial distribution of capping functional groups and crystallographic characteristics of crystal facets. Therefore,
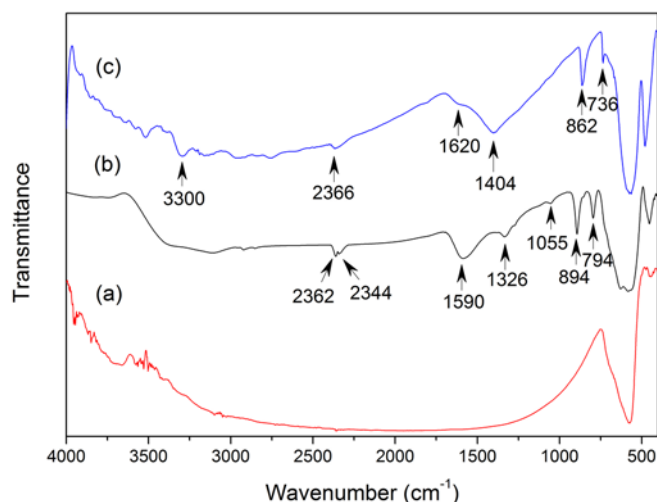
Figure 2.9 FTIR spectra of Fe_3O_4 particles synthesized with (a) PEG, (b) aminopropanol, and (c) urea. The data was normalized with respect to the minimum transmittance.

although the same capping agents were used in synthesizing α - Fe_2O_3 and Fe_3O_4, they developed into nanoparticles with different shapes, as shown in Figure 2.4.

In order to investigate the interaction between capping agent and Fe_3O_4 nanocrystals, FT-IR measurements were carried out on three type magnetite particles, as depicted in Figure 2.9. A strong absorption band at 547 cm^{-1} is due to Fe-O bond in Fe_3O_4[21]. In the spectrum of magnetite synthesized with the aminopropanol (Figure 2.9(b)), this absorption band of IR spectra shifts slightly to higher wavenumbers and splits into two subbands (580 and 632 cm^{-1}) which may be caused by the particle size reduction and split of the energy levels of the quantized magnetite particles.[22] The peaks around 1590 cm^{-1} attributed to the asymmetrical deformation vibration (δ_{as})of $-NH_2$ confirm the existence of aminopropanol on the surface of Fe_3O_4 nanoparticles. Moreover, the sharp band peaks around 894 and 796 cm^{-1} are ascribed to the deformation vibration of $-OH$ relative to the iron ions. In the case of urea used, as shown in Figure 2.9(c), the $-NH_2$ stretching band at 3300 cm^{-1} and symmetrical C=O stretching band at 1404 cm^{-1} were observed. Based on this, we conclude that in the structure of Fe–urea complex, the C=O group of urea coordinates with Fe cation, while $-NH_2$ groups are symmetrically located on the outside, similar to the discussion by Yu and Chow[12] on the two binding modes of C=O bond on the maghemite surface. No distinct absorption IR peaks related to C–O–C bond can be observed in the spectra of Fe_3O_4 synthesized with the PEG. This is because the PEG molecules have been removed during the washing step, supporting the evidence that the interaction is weak between the PEG and the magnetite crystal surface.

The 3-aminopropanol molecules used in this study are composed of one amino group and one hydroxyl group at the two ends of the molecule, as shown in Figure 2.6, inducing the
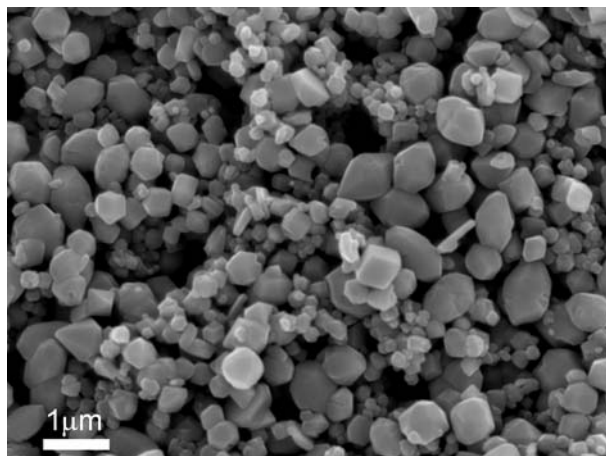
Figure 2.10 SEM image of Fe_3O_4 particles synthesized at 200^oC for 20 h with urea as stabilizer.

molecule a high polarity. The surface charge potential of Fe_3O_4 in water is associated with the pH value of the solvent. In basic solvents, the Fe_3O_4 surface shows negative charge and terminates by Fe–OH.[23] When the aminopropanol was added into the reaction medium, the amino group strongly adsorbed on the crystal surface, as proved above by the FT-IR result. The adsorbed molecule layer hindered diffusion of the iron cations through the layer, hence further nanocrystal growth were retarded. As shown in Figure 2.4, the size of particles synthesized with the aminopropanol is much smaller compared with that synthesized with the other molecules at the same synthesis conditions, providing the evidence that binding energy is higher between the aminopropanol and the magnetite surface.

Unlike 3-aminopropanol and urea molecules, PEG has a long chain structure, with hydrophilic hydroxyl radicals $(-OH)$ at the end of the chain and hydrophobic $-CH_2-CH_2$ inside the chain. As schematically shown in Figure 2.6(d), the PEG molecule forms rugged long chains when dissolved in water. And these chains interact with each other to form 'capping cages' template to confine the further growth of smaller nanoparticles.[24, 25] Some nanostructured inorganic materials have been synthesized with PEG, such as Cu_2O nanocubes,[26] Sb_2O_3 octahedrons,[27] and flower-like ZnO.[28] In this work, PEG plays a critical role in the bimodal particle size distribution with a large particle size difference, in which the surfaces of larger particles are faceted. This is because the space of the PEG 'cages' has a limit. Once the particle exceeds the critical value, the confinement effect of the PEG cage template does not work. These unconfined particles can develop the equilibrium shape with the low energy planes ($\{111\}$ for magnetite[29]) exposed. In addition, the binding of active –O– atoms of the PEG chains with the Fe_3O_4 surface is weak, so that the PEG can be removed by washing. This is consistent with the results in FTIR measurement.
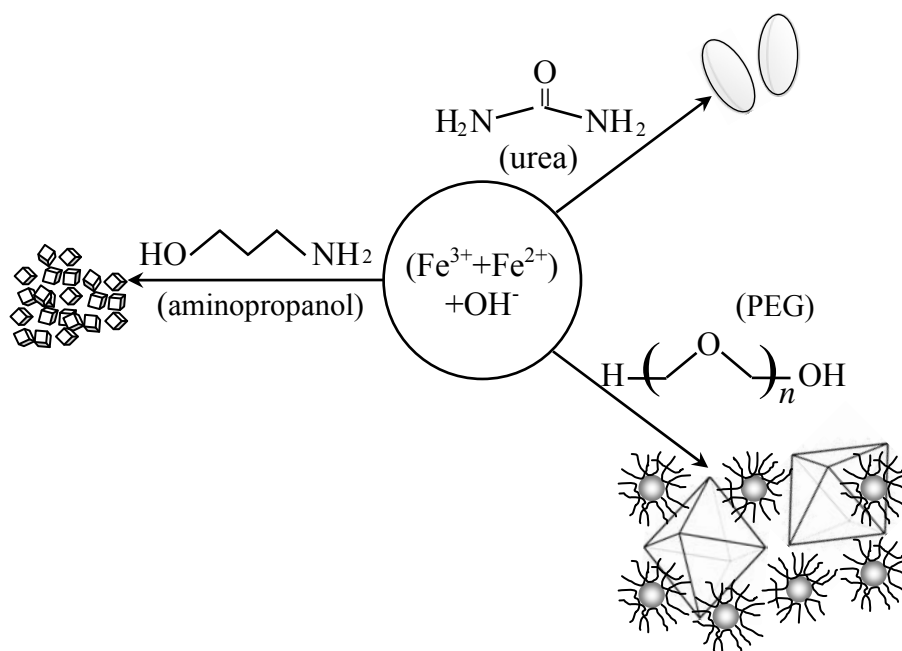
Figure 2.11 Schematic illustration of the magnetite particle formation process with different stabilizers in reaction system.

Because of the high symmetry of magnetite crystal structure, the anisotropic growth of magnetite in solution is difficult. Hu *et al.* reported the preparation of magnetite with ellipsoidal morphology by direct thermal decomposition of $FeCO_3$ with the same morphology.[30] However, the shape of Fe_3O_4 in Hu's work is inherited from that of $FeCO_3$ instead of the result of direct growth in solution. Here, in this work, the magnetite developed into ellipsoidal shape when the urea-containing reaction medium was hydrothermally treated for 10 h. When the synthesis duration was prolonged from 10 h to 20 h with urea in the reaction system, the ellipsoidal shaped magnetite developed into the faceted ones, as shown in Figure 2.10. A similar shape transformation from an ellipsoidal shape to a dodecahedron-shape has been reported in synthesizing magnetite by the surfactant of EDTA.[31] A kinetically controlled shape evolution
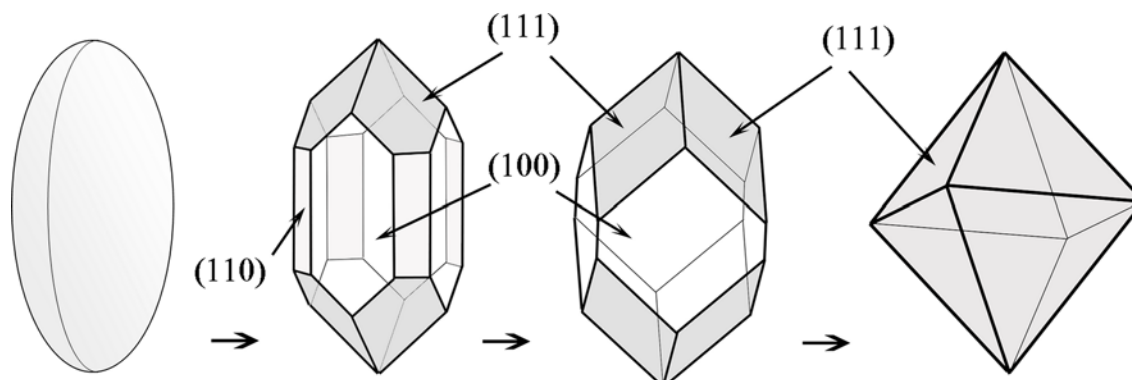

Figure 2.12 Schematic illustration of faceting process of ellipsoidal magnetite particles. Low energy density {111} planes dominate the particle surface at last to meet the surface energy requirement.

mechanism has been suggested that the growth rate of different crystallographic planes was changed by specific binding of EDTA. There are also reports on Ostwald ripening growth mechanism of octahedral magnetite nanoparticles.[32]

Figure 2.12 schematically illustrates the faceting process from the ellipsoidal shape to the octahedron. The process involves the elimination of high energy planes of {001} and {101}, resulting from the growth competition of {111}, {100}, and {101} facets. This shape transformation process implies that the binding energy between the urea molecules and the Fe_3O_4 crystalline surface planes is followed by $\sigma\{111\} > \sigma\{001\} > \sigma\{101\}$ in sequence. Under hydrothermal conditions, the urea molecules prefer to adsorb on the {111} facets of crystals, leading to more (111) planes as exposed facets, resulting from preferential addition of growth unit to the {100} facet of magnetite.[33]

Hydrothermal growth of α-FeOOH nanorods

α-FeOOH is the most thermodynamic stable phase among all iron oxide and oxyhydroxide and plays a central role in many geochemical processes.[92] Proposed goethite growth mechanisms range from dissolution of precursor ferrihydrite nanoparticles followed by precipitation of goethite[35] to oriented aggregation accompanied by phase transformation.[36] It was suggested that the dissolution and recrystallization of α-FeOOH is achieved through $FeO_3(OH)_3$ unit.[37] Recently, the oriented aggregation mechanism has received much attention, and has been successfully used to explain the growth of many nanostructures.[36, 38-41] Burleson and Penn proposed that the goethite grows by phase transformation of six-line ferrihydrite nanoparticles to goethite followed by oriented aggregation of the goethite primary particles.[36] Synchrotron radiation-based energy dispersive X-ray diffraction (ED-XRD) measurements on the phase transformation process of Ferrihydrite to α-FeOOH showed that Fe^{2+} could accelerate the transformation rate.[37] However, the influence of Fe^{2+} on morphology of final products is still not clear. In this work, Fe cations of different valence were used to investigate the formation process of goethite nanorods and the intrinsic nature of anisotropic growth of goethite was uncovered.

The representative SEM images of the as-synthesized powders are shown in Figure 2.5 which clearly reveals that one-dimensional goethite nanorods are obtained through both the two methods. Anisotropy growth of nanostructures can be explained by assuming that the system followed oriented attachment mechanism which has been successfully applied on various materials. Upon hydrothermal conditions, goethite clusters, initially converted from ferrihydrite clusters by phase transformation, aggregate to form nanorods.[36] It also should be noticed that,
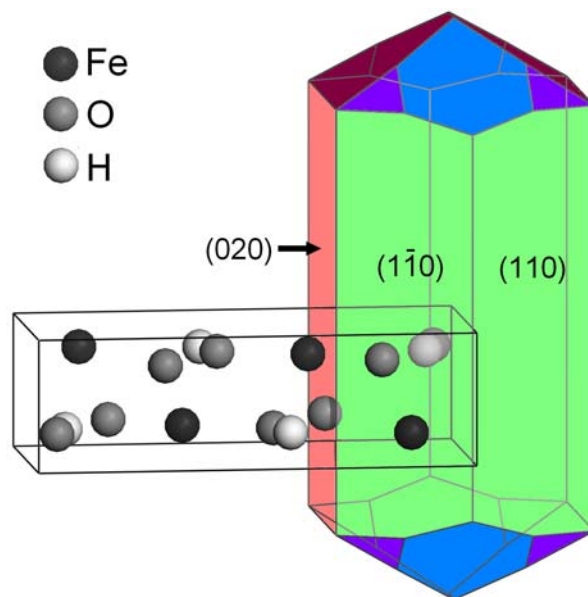
Figure 2.13 Crystal unit of goethite and corresponding predicted morphology by using BFDH method.

in contrast to powders in Figure 2.5(b), there are many small clusters left on the surface of goethite nanorods in Figure 2.5(a). As we mentioned above, the ferrous iron could shorten the transformation time from ferrihydrite to goethite. The excessive clusters which did not aggregate onto the goethite nanorod will thus be left as isolated nanoclusters, as evidenced in inset of Figure 2.5(a). From the above results, we proposed that the acceleration effect of Fe^{2+} only work in the first step during the formation process of goethite. In other words, the adding of Fe^{2+} only promotes the dissolution of ferrihydrite. Cornell *et al*. proved that Fe^{2+} cations are inclined to be adsorbed on the surface of ferrihydrite and donor electrons to surface iron cations to serve as the reducing agent.[37, 42] The role of Fe^{2+} that Cornell *et al*. proposed is in agreement with the experimental result here.

What is also can be seen from SEM images is that goethite develops into 1D nanostructures regardless of the growth route, implying that the growth characteristics are more intrinsic. To further understand the growth habit of goethite, crystal morphology was predicted by using classical BFDH model, which was originally proposed by Bravasis and Freidel, assuming that the relative growth rate of faces {*hkl*} is inversely proportional to the interplanar spacing and thus their morphological importance[43]:

$$h_{hkl} \propto r_{hkl} \propto \frac{1}{d_{hkl}} \qquad\qquad 2.7$$

Later, the model was revised by Donnay and Harker to fit the situations when there is helical symmetry axis or glide-plane of symmetry in the crystal structure.[44] The prediction of BFDH

modal is only based on the geometry structure of crystals. Therefore, the prediction results reflect the intrinsic nature of crystal growth. As given in Figure 2.13, the calculation results show that the surface weight of {020} and {110} planes are 31.5% and 39.8% separately. The equilibrium morphology constructed by Wulff's law shown in Figure 3 indicates that goethite prefers to grow along *c*-direction. Thus the prediction gives an explanation on the reason why α -FeOOH nanocrystals obtained from different routes developed into one-dimensional structure.

2.4   Conclusions

Synthesis and morphology control of iron oxide nanopowders has important implications for improving the performance of iron oxide materials, as well as provides a basis for the development of new applications. Although attentions have been paid on hydrothermal synthesis of iron oxide, the morphology control is still a challenge. This chapter focuses on the development of shape control of iron oxide nanocrystals using a capping agent-based hydrothermal method that maintains the high yields and chemical processability required for practical applications. A general growth mechanism for the iron oxide nanoparticles of different shapes prepared by the hydrothermal method is thus proposed. The main conclusions are as follows:

- The morphology of iron oxide nanomaterials synthesized *via* hydrothermal method is mainly determined by their crystallographic structures. Addition of capping agent into the reaction medium could change the growth habit of different crystal planes as a result of interaction between organics and iron oxide crystals, thus the morphologies could be tuned. The interactions are determined by type of end-functional group, chain length and crystal structure of nanoparticles.

- Chelating between N atoms and iron cations on iron oxide surface promotes the growth of hematite into plate-like and confines the growth of Fe_3O_4 in all directions.

- Urea molecules adsorb symmetrically on crystal surface leads to polyhedral shape of hematite. Magnetite grows into ellipsoidal shape in the presence of urea and evolves into faceted one with prolonging the hydrothermal duration.

- PEG molecules are inclined to interact with each other to form 'cages templates' instead of adsorbing on the surface of iron oxides. The templates can be used to confine the growth of iron oxide nanoparticles.

- A terrace-kink-step growth mechanism for growth of faceted iron oxide nanoparticles was proposed.

Reference

[1] El-Sayed, M. *Acc. Chem. Res.* **2001**, *34*(4), 257–264.

[2] Buhro, W. E.; Colvin, V. L. *Nat. Mater.* **2003**, *2*, 138–139.

[3] El-Sayed, M. A. *Acc. Chem. Res.* **2004**, *37*(5), 326–333.

[4] Wulff, G. *Z. Kristallogr.* **1901**, *34*, 449.

[5] Herring, C. *Phys. Rev.* **1951**, *82*(1), 87–93.

[6] Barnard, A. S.; Zapol, P. *J. Chem. Phys.* **2004**, *121*(9), 4276–4283.

[7] Barnard, A. S.; Curtiss, L. A. *Nano Lett.* **2005**, *5*(7), 1261–1266.

[8] Gilbert, F.; Refait, P.; Léveque, F.; Remazeille, C.; Conforto, E. *J. Phys. Chem. Solids* **2008**, *69*, 2124–2130.

[9] Pu, Z.; Cao, M.; Yang, J.; Huang, K.; Hu, C. *Nanotechnology* **2006**, *17*, 799–804.

[10] Lee, S.-M.; Cho, S.-N.; Cheon, J. *Adv. Mater.* **2003**, *15*, 441–444.

[11] Lee, S.-M.; Jun, Y.-W.; Cho, S.-N.; Cheon, J. *J. Am. Chem. Soc.* **2002**, *124*(38), 11244–11245.

[12] Yu, S.; Chow, G. M. *J. Mater. Chem.* **2004**, *14*, 2781–2786.

[13] Wang, X.-G.; Weiss, W.; Shaikhutdinov, S. K.; Ritter, M.; Petersen, M.; Wagner, F.; Schlögl, R.; Scheffler, M. Aug **1998**, *81*(5), 1038–1041.

[14] Barrón, V.; Torrent, J. *J. Colloid Interface Sci.* **1996**, *177*, 407–410.

[15] Hu, X.; Yu, J. C. *Adv. Funct. Mater.* **2008**, *18*, 880–887.

[16] Cao, M.; Liu, T.; Gao, S.; Sun, G.; Wu, X.; Hu, C.; Wang, Z. L. *Angew. Chem. Int. Ed.* **2005**, *44*(27), 4197–4201.

[17] Trainor, T. P.; Chaka, A. M.; Eng, P. J.; Newville, M.; Waychunas, G. A.; Catalano, J. G.; Brown Jr., G. E. *Surf. Sci.* **2004**, *573*, 204–224.

[18] Qiao, C.; V., R. N. *Prog. Surf. Sci.* **2003**, *73*, 59–77.

[19] Frandsen, C.; Bahl, C. R. H.; Lebech, B.; Lefmann, K.; Kuhn, L. T.; Keller, L.; Andersen, N. H.; v. Zimmermann, M.; Johnson, E.; Klausen, S. N.; Mørup, S. *Phys. Rev. B* **2005**, *72*(21), 214406.

[20] Nedkov, I.; Merodiiska, T.; Slavov, L.; Vandenberghe, R. E.; Kusano, Y.; Takada, J. *J. Magn. Magn. Mater.* **2006**, *300*, 358–367.

[21] Waldron, R. D. *Phys. Rev.* **1955**, *99*, 1727–1735.

[22] Ma, M.; Zhang, Y.; Yu, W.; Shen, H.; Zhang, H.; Gu, N. *Colloid. Surf. A* **2003**, *212*, 219–226.

[23] Jung, Y.; Choi, J.; Lee, W. *Chemosphere* **2007**, *68*, 1968–1975.

[24] Cao, M.; Wang, Y.; Guo, C.; Qi, Y.; Hu, C.; Wang, E. *J. Nanosci. Nanotechnol.* **2004**, *4*(7), 824–828.

[25] Wang, W. Z.; Poudel, B.; Wang, D. Z.; Ren, Z. F. *Adv. Mater.* **2005**, *17*, 2110–2114.

[26] Gou, L.; Murphy, C. J. *J. Mater. Chem.* **2004**, *14*, 735–738.

[27] Ma, X.; Zhang, Z.; Li, X.; Du, Y.; Xu, F.; Qian, Y. *J. Solid State Chem.* **2004**, *177*, 3824–3829.

[28] Li, X.; Duan, T.; Zhu, X.; Qian, Y. *Mater. Lett.* **2006**, *60*(28), 3350–3353.

[29] Zheng, R.; Gu, H.; Xu, B.; Fung, K. K.; Zhang, X.; Ringer, S. P. *Adv. Mater.* **2006**, *18*(18), 2418–2421.

[30] Xuan, S.; Chen, M.; Hao, L.; Jiang, W.; Gong, X.; Hu, Y.; Chen, Z. *J. Magn. Magn. Mater.* **2008**, *320*(3-4), 164–170.

[31] Chen, F.; Gao, Q.; Hong, G.; Ni, J. *J. Magn. Magn. Mater.* **2008**, *320*(11), 1775–1780.

[32] Hu, C.; Gao, Z.; Yang, X. *Chem. Phys. Lett.* **2006**, *429*, 513–517.

[33] Chen, J.; Wiley, B.; Li, Z.-Y.; Campbell, D.; Saeki, F.; Cang, H.; Au, L.; Lee, J.; Li, X.; Xia, Y. *Adv. Mater.* **2005**, *17*, 2255–2261.

[34] Vayssieres, L. *Int. J. Nanotechnol.* **2004**, *1*(1), 1–41.

[35] Schwertmann, U.; Murad, E. *Clays Clay Miner.* **1983**, *31*(4), 277–284.

[36] Burleson, D. J.; Penn, R. L. *Langmuir* **2006**, *22*(1), 402–409.

[37] Yee, N.; Shaw, S.; Benning, L. G.; Nguyen, T. H. *Am. Mineral.* **2006**, *91*(1), 92–96.

[38] Wang, X.; Xu, J. B.; Ke, N.; Yu, J.; Wang, J.; Li, Q.; Ong, H. C.; Zhang, R. *Appl. Phys. Lett.* **2006**, *88*(22), 223108.

[39] Penn, R. L. *J. Phys. Chem. B* **2004**, *108*(34), 12707–12712.

[40] Huang, F.; Zhang, H.; Banfield, J. F. *J. Phys. Chem. B* **2003**, *107*(38), 10470–10475.

[41] Ribeiro, C.; Lee, E. J. H.; Longo, E.; Leite, E. R. *ChemPhysChem* **2006**, *7*(3), 664–670.

[42] Cornell, R. M.; Schwertmann, U. *The Iron Oxide: Structure, Properties, Reactions, Occurrence and uses;* Wiley-VCH: New York, 2003.

[43] Docherty, R.; Clydesdale, G.; Roberts, K. J.; Bennema, P. *J. Phys. D: Appl. Phys.* **1991**, *24*(2), 89–99.

[44] Shi, E.; Chen, Z.; Yuan, R.; Zhen, Y. *Hydrothermal Crystallization;* Science Press of China: Beijing, 2004. (In Chinese)

Chapter 3   Determination of Surface Crystallography of Faceted Nanoparticles using TEM Imaging and Diffraction Mode

3.1   Introduction

Recently, much attention has been focused on faceted nanoparticles with various shapes, due to their unique properties and potential applications in catalysis,[1, 2] surface-enhanced Raman scattering (SERS)[3] and optoelectronics.[4] It has been demonstrated that many shape-related properties of nanoparticles can be attributed to their surface crystallographic structure. For instance, tetrahexahedral Pt nanoparticles with a high-index {730} plane exhibit enhanced catalytic activity for electro-oxidation compared with that of spherical particles.[5] As we discussed in Chapter 2, the surface crystal structure also plays a critical role in the anisotropic growth of nanocrystals. The selective binding of capping molecules on different crystal planes may alter their surface energies and thus change their growth modes.[87, 7] Therefore, the characterization of the surface crystallographic features of nanoparticles has become an important issue for the study of their surface-related properties and the investigation of their shape-evolution mechanism in growth processes.

A particle enclosed by a finite number of crystallographic planes, generally associated with different surface energies, can have a specific geometric shape. Normally, the minimization of surface energy tends to increase the portion of the low index planes, forming facets on the particle surface. Figure 3.1 shows a group of common shapes of face-centered cubic (f.c.c.) metals, enclosed by {111} and {100} facets and containing a low percentage of corner and edge sites. Benefitted from the development of chemical synthesis technique, nanocrystals enclosed by high-index planes can be easily obtained which were named "unconventional shaped" nanoparticles by Xia et al.[2]

The application of transmission electron microscopy (TEM) techniques to crystallographic analysis was suggested several years ago[8]. The surface plane indices are conventionally indexed by comparing its diffraction pattern with its in-image projection after bringing the plane to the edge-on position in TEM. Sometimes, high-resolution TEM (HRTEM) images that record the atomic spacing of the edge-on planes are used to verify the determination of the surface plane index.[9, 88] The method is particularly suitable for nanoparticles with conventional
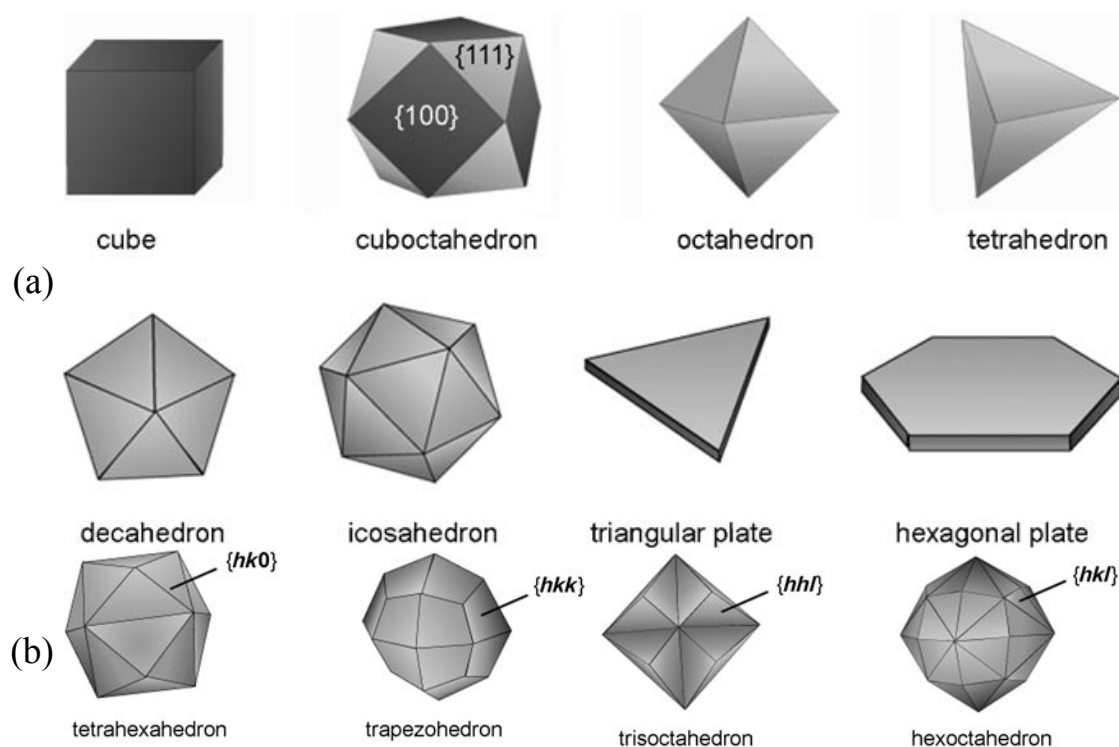
Figure 3.1 (a) Geometrical shapes of f.c.c. metals whose surface is enclosed by {100} and/or {111} facets. (b) Unconventional shapes of f.c.c. metals whose surface is enclosed by high-index facets[2].

shapes,[2] *i.e.* the particles are enclosed by symmetric low-index facets, as in most cases the low-indexed planes can easily satisfy the diffraction condition and generate diffraction spots. However, for particles with unconventional shapes,[2] *i.e.* covered with high-index facets, the method shows limitations. In such cases, it is often difficult to obtain the corresponding diffraction spots for the high-index planes. To solve this problem, an attempt has been made by measuring the angles between the surface plane projection when the planes are simultaneously on the edge-on position and comparing them with the theoretical interfacial angles to conclude the Miller indices of the facet.[5] Obviously, the method requires great effort in searching for the edge-on positions and sometimes it is not possible to obtain such a position for some planes when the shape of the particle is not favorable. Moreover, the study of unconventionally shaped nanoparticles has recently become an increasing interesting topic, due to their unique catalytic properties resulted from the high-index surface facets. Naturally, the correct indexing of such surface planes constitutes one of the important bases for the further investigation of properties and growth kinetics. Therefore, there is a great need for a general and accurate determination method. In response to such a requirement, we have developed a general calculation method that can be applied to determine any faceted surface plane indices of nanoparticles without requiring the rigorous plane-on edge condition, provided that the edges of the facets are visible

under TEM imaging mode. This technique will facilitate surface-related properties research in nanoscience.

3.2 Methodology

The basic principle of this method is to determine the edge vectors that define the surface facets of a nanoparticle in the TEM screen coordinate system, and then obtain the surface plane normal by cross product and further calculate their Miller indices in the crystal coordinate system through coordinate transformation. The full method is detailed as follows.

3.2.1 Setting of Coordinate Systems

Considering the characteristics of TEM for sample loading and imaging, it is convenient to introduce three Cartesian coordinate system in addition to the lattice base of the crystal and its reciprocal base. All the coordinate systems are of the same handedness and the Cartesian co-ordinate systems are orthonormal. In the present work, we choose the right-hand set. Of the three Cartesian coordinate systems, one is referenced to the screen of the TEM that records the image of the particle, with its z axis set in the inverse direction of the incident electron beam. The second coordinate system is set to the sample holder, also with its z axis in the inverse direction of the incident electron beam when the holder is in the non-tilt position, and the third one is set to the crystal under the convention described in *International Tables for Crystallography*.[11] The orientation relationships between the Cartesian coordinate systems are defined as a set of rotations [Euler angles in Bunge notation[12]] transforming one system into another.

3.2.2 Determination of Edge Vectors in the Screen Coordinate System

To determine the coordinates of an edge vector in the screen coordinate system, two sample positions are required. Assume that the unit edge vector in the sample-holder coordinate system is $\mathbf{v}(x, y, z)$ and let the equivalent vectors in the screen coordinate system with respect to the two sample-holder positions be $\mathbf{v}_1(x_1, y_1, z_1)$ (position 1) and $\mathbf{v}_2(x_2, y_2, z_2)$ (position 2). Under TEM imaging mode, let the orientation relationship between the screen coordinate system and the first sample position be described by the rotation $R(\varphi_1, \Phi, \varphi_2)$ and the rotation from the first sample position to the second be $\Delta R(\Delta\varphi_1, \Delta\Phi, \Delta\varphi_2)$, as shown in Figure 3.2. For simplicity, the first sample position could be taken without a tilt operation. R is then characterized by a single rotation around the z axis of the screen coordinate system caused by the electromagnetic rotation of the electron beam, which is magnification dependent. Thus, the following relations between the unit vectors $\mathbf{v}$, $\mathbf{v}_1$ and $\mathbf{v}_2$ hold for
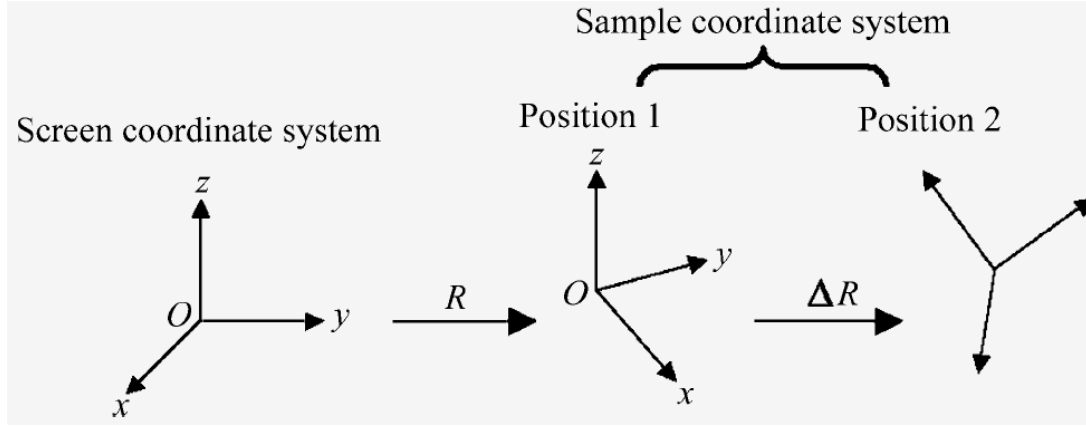
Figure 3.2 Relative positions of the screen and sample coordinate systems.

$$\mathbf{v}_1 = M_1 \cdot \mathbf{v} \qquad\qquad 3.1(a)$$

$$\mathbf{v}_2 = M_1 \cdot M_2 \cdot \mathbf{v} \qquad\qquad .1(b)$$

where M_1 and M_2 are the corresponding rotation matrices of R and ΔR, and are known. Then the relation between $\mathbf{v}_1(x_1, y_1, z_1)$ and $\mathbf{v}_2(x_2, y_2, z_2)$ can be deduced as

$$\mathbf{v}_1 = M_1 \cdot M_2^{-1} \cdot M_1^{-1} \cdot \mathbf{v}_2 \qquad\qquad 3.2$$

where M_1^{-1} and M_2^{-1} are the inverse matrices of M_1 and M_2. According to the imaging principle of TEM, the image of a nanoparticle is the rotated (around the z axis of the screen coordinate system and dependent on the magnification) and amplified projection of the particle. As the z axis of the screen coordinate system is set parallel to the incident beam, *i.e.* the z axis is parallel to the projection direction, the x and y coordinates of $\mathbf{v}_1$ and $\mathbf{v}_2$ in the screen coordinate system can be measured. Only z_1 and z_2 are known. With the three linear equation offered by equation 3.2, these two unknowns can be resolved. Thus, the coordinates of the edge vector in the screen coordinate system are determined.

It should be noted that for an over-determined system of linear equations like equation 3.2, the problem of compatibility between the equations has to be addressed. In the specific case of equation 3.2, the equations all originate from different projections of the same object, so that compatibility is ensured *de facto,* except for the uncertainties inherent in any measurement. To obtain a unique solution, one can use the classical least-squares method. However, in the present case, the determination of the intersects between the edge vectors for measuring their x and y coordinates in the screen coordinate system is not accurate. Thus, we may artificially change the length of the vectors from one sample position to another due to measurement uncertainties. Therefore, we have included a linear scalar quantity – ensuring the ratio of the vector length is equal to unity – as an additional unknown to obtain unique solutions of z_1 and z_2.
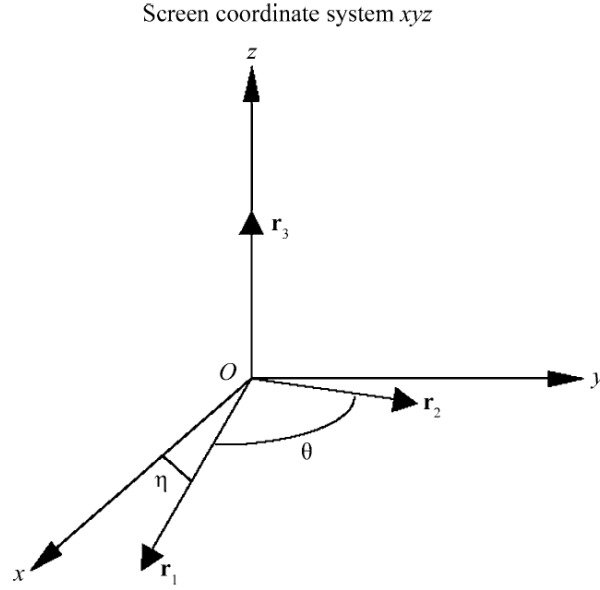
Screen coordinate system *xyz*

Figure 3.3 Illustration of the screen coordinate system and the reference base of $\mathbf{r}_1$-$\mathbf{r}_2$-$\mathbf{r}_3$. $\mathbf{r}_1$ and $\mathbf{r}_2$ are reciprocal lattice vectors determined by indexing the spot diffraction pattern. $\mathbf{r}_3$, calculated by cross product, is expressed in reciprocal space. It should be noted that $\mathbf{r}_3$ is not necessarily a reciprocal lattice vector.

3.2.3 Coordinate Transformation Matrices

Coordinate transformation from the screen coordinate system to the crystal bases can be achieved through acquiring and indexing the electron diffraction pattern of the crystal. The diffraction pattern can be either in a spot pattern or in a Kikuchi line pattern. For simple operation, one of the two sample positions used to determine the edge vectors in the screen coordinate system could be dedicated to obtaining a diffraction pattern of a low-index zone axis. There is no automatic program currently available to determine the orientation of the crystallite directly with respect to either the sample holder or the screen of the microscope by indexing the spot pattern, although such software to determine the orientation by indexing the Kikuchi pattern is available. Thus, we will treat the spot pattern and the Kikuchi pattern separately in this work.

According to the diffraction geometry, the TEM diffraction spot pattern of a crystallite is the amplified two-dimensional reciprocal plane of the crystallite, which is perpendicular to the incident beam or the z axis of the screen coordinate system. Each spot in this reciprocal plane represents one set of diffracting planes expressed with Miller indices (*hkl*). Thereciprocal vector with components (*h, k, l*) in the reciprocal base is perpendicular to the plane with Miller indices (*hkl*) in the direct lattice space. Thus, with a correctly indexed diffraction pattern, it is easy to find two vectors $\mathbf{r}_1$ and $\mathbf{r}_2$ that are coincident with two reciprocal lattice vectors (h_1, k_1,

l_1) and (h_2, k_2, l_2) in the xOy plane of the screen coordinate system. By vector cross product, one can easily obtain the third vector $\mathbf{r}_3$ in the z direction, as shown in Figure 3.3. The three vectors should be referred to the same basis, either to reciprocal space or to direct space. It should be noted that $\mathbf{r}_3$ is not necessarily a reciprocal lattice vector. The coordinate transformation of the vectors between direct space and reciprocal space can be easily realized with the direct metric tensor or the reciprocal metric tensor [equation 3.11 and 3.12 in Appendix A]. Here we refer the three vectors to reciprocal space. Therefore, the coordinate transformation matrix $M_{I \to r}$ from the screen coordinate system to the $\mathbf{r}_1$ - $\mathbf{r}_2$ - $\mathbf{r}_3$ reference base is:

$$M_{I \to r} = \begin{bmatrix} \|r_1\| \cdot \cos\eta & \|r_2\| \cdot \cos(\eta+\theta) & 0 \\ \|r_1\| \cdot \sin\eta & \|r_2\| \cdot \cos(\eta+\theta) & 0 \\ 0 & 0 & r_3 \end{bmatrix} \qquad 3.3$$

where η is the angle between the x axis and $\mathbf{r}_1$, and θ is the angle between $\mathbf{r}_1$ and $\mathbf{r}_2$. The coordinate transformation matrix $M_{r \to R}$ from the $\mathbf{r}_1$ - $\mathbf{r}_2$ - $\mathbf{r}_3$ reference base to reciprocal space is

$$M_{r \to R} = \begin{bmatrix} h_1 & h_2 & r_3^{a*} \\ k_1 & k_2 & r_3^{b*} \\ l_1 & l_2 & r_3^{c*} \end{bmatrix}^{-1} \qquad 3.4$$

where r_3^{a*}, r_3^{b*} and r_3^{c*} are the components of $\mathbf{r}_3$ referred to reciprocal space. In this way, the coordinate transformation matrix from the screen coordinate system to reciprocal space, $M_{I \to R}$, and that to direct space, $M_{I \to l}$, are

$$M_{I \to R} = M_{I \to r} \cdot M_{r \to R} \qquad 3.5$$

and

$$M_{I \to l} = M_{I \to R} \cdot G^* \qquad 3.6$$

in which G^* is the metric tensor of the reciprocal basis.

The orientation of the crystallite with respect to the sample coordinate system can be directly determined by indexing the Kikuchi line pattern using the commercial software Euclid's Phantasies (EP)[13, 14]. The orientation of the crystallite is expressed by three Euler angles, φ_1, Φ, and φ_2 (in Bunge notation), rotating the sample-holder coordinate system to the Cartesian crystal coordinate system. The orientation relationship between the Cartesian crystal coordinate system and the Bravais lattice basis is set under the convention given in *International Tables for Crystallography*[11] and is described in Appendix B. Thus, the screen-to-reciprocal lattice base transformation matrix $M_{I \to R}$ and the screen-to-crystal coordinate system transformation matrix $M_{I \to l}$ will be

$$M_{I \to R} = M_1 \cdot M_{EP} \cdot M_{C \to R} \qquad 3.7$$

Table 3.1 The rotation angles that characterize the coordinate transformation from the screen coordinate system to the first sample position, R, and that from the first sample position to the second, ΔR.

$R\,(\varphi_1,\,\Phi,\,\varphi_2)$	$\Delta R\,(\Delta\varphi_1,\,\Delta\Phi,\,\Delta\varphi_2)$
(165.84°, 0, 0)	(0, 10.26°, -5.80°)

Table 3.2 Illustration of the unit edge vectors $\mathbf{v}_i$ with respect to the two sample holder positions (positions 1 and 2) in the screen coordinate system calculated with their measured trace coordinates in the screen coordinate system.

	x_1	y_1	z_1	x_2	y_2	z_2
$\mathbf{v}_1$	-0.364	-0.685	-0.631	-0.456	-0.743	-0.490
$\mathbf{v}_2$	-0.188	0.530	-0.827	-0.171	-0.396	-0.902
$\mathbf{v}_3$	0.950	-0.163	0.267	0.940	-0.212	0.267

and

$$M_{I \to l} = M_{I \to R} \cdot G^* \tag{3.8}$$

in which M_I is the rotation matrix from the screen to one of the sample-holder positions where the Kikuchi pattern is acquired, M_{EP} is the transformation matrix from the sample-holder coordinate system to the Cartesian crystal coordinate system and $M_{C \to R}$ is the transformation matrix from the Cartesian crystal coordinate system to reciprocal space.

Therefore, for any vector obtained in the screen coordinate system $\mathbf{v}_i\,(x_i,\,y_i,\,z_i)$ that corresponds to the sample position acquiring the diffraction pattern, its components in the lattice space can be calculated as

$$M_{I \to l}^{-1} \cdot \begin{bmatrix} x_i \\ y_i \\ z_i \end{bmatrix} \tag{3.9}$$

and the reciprocal of the intercept of the plane with the lattice base vector normal to $\mathbf{v}_i\,(x_i,\,y_i,\,z_i)$ can be obtained as

$$M_{I \to R}^{-1} \cdot \begin{bmatrix} x_i \\ y_i \\ z_i \end{bmatrix} \tag{3.10}$$

In this way, the Miller indices of the edges and surface planes of the crystallite can be determined.
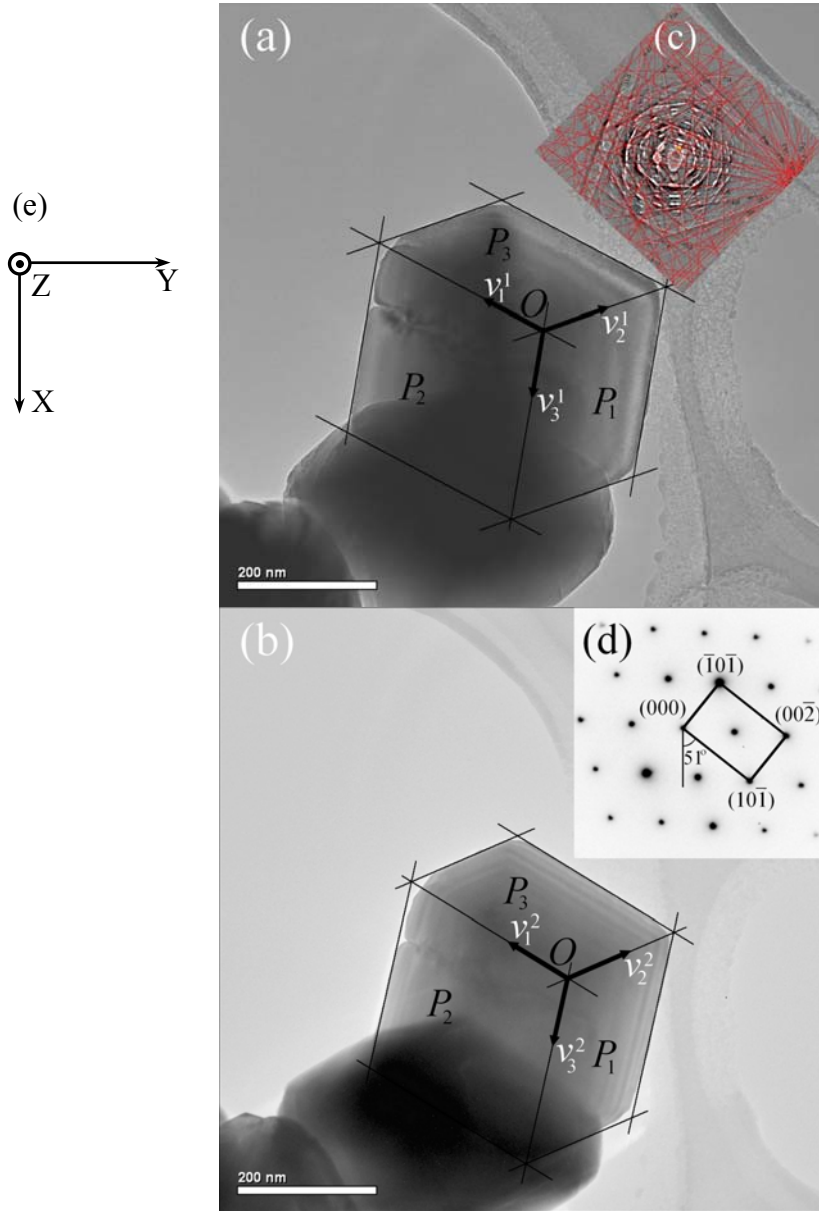
Figure 3.4 TEM images of hematite particle at (a) initial position and (b) tilted position. The insets are their corresponding (c) Kikuchi pattern and (d) spot pattern. (e) is the screen coordinate system.

3.3   Application

We now present an example to illustrate the application of the above method. The nanoparticles used in this example are hematite (α-Fe$_2$O$_3$) synthesized via a chemical route. They belong to the trigonal crystal system (space group $R\bar{3}c$) with lattice parameters a = b = c = 5.419 Å, $\alpha = \beta = \gamma = 55.36°$. Hereafter we express the Miller indices in the trigonal base. The images and diffraction patterns of the hematite nanoparticle to be determined were recorded using a Philips CM200 TEM at 200 kV. Figure 3.4 shows the TEM images of the hematite particle at the two sample positions and the corresponding diffraction patterns. The Kikuchi and

Table 3.3 Calculated Miller indices of the edge vectors $\mathbf{v}_i$ and planes P_i from indexing the corresponding diffraction pattern and Kikuchi line pattern.

		Spot index	Deviation from refined index	Kikuchi index	Deviation from re-fine index	Refined index
edge	$\mathbf{v}_1$	[-1.56 -1.08 1.87]	1.56°	[-1.47 -1.2 1.84]	2.57°	[$\bar{4}\bar{3}5$]
	$\mathbf{v}_2$	[-0.12 -1.07 -0.92]	3.58°	[0.03 1.07 -1.0]	1.23°	[$0\bar{1}\bar{1}$]
	$\mathbf{v}_3$	[2.01 -0.84 0.325]	0.87°	[2.05 -0.76 0.313]	1.18°	[$25\bar{1}0\,4$]
plane	P_1	(1.29 2.08 -2.16)	0.87°	(1.25 2.29 -2.48)	2.30°	($35\bar{6}$)
	P_2	(1.34 4.705 3,84)	0.75°	(1.12 4.54 3.864)	2.60°	(3 11 9)
	P_3	(-3.09 1.71 -1.59)	1.63°	(-3.26 1.56 -1.59)	0.89°	($\bar{2}1\bar{1}$)

spot diffraction images are inserted after correcting the additional rotation from the image of the particle. It can be seen that the particle has a polyhedral shape. The three distinct edges of the particle are denoted with the unit vectors $\mathbf{v}_1$, $\mathbf{v}_2$ and $\mathbf{v}_3$ and the three distinct surfaces defined by the edge vectors are P_1, P_2, and P_3, as shown in Figure 3.4. The rotation angles that characterize the orientation relationship between the screen coordinate system and the first sample position (position 1; no tilt), R, and from the first sample position to the second position (position 2; tilted), ΔR, are given in Table 3.1. The x and y components of vector $\mathbf{v}_i$, corresponding to the two sample positions in the screen coordinate system, were measured and their z components were calculated. The results are displayed in Table 3.2. One Kikuchi pattern (inset of Figure 3.4(a)) was taken at sample position 1 and indexed using the program EP [14]. The set of Euler angles that denotes the rotation from the sample coordinate system to the Cartesian crystal coordinate system is (182.63°, 80.11°, 33.99°). One diffraction spot pattern (inset of Figure 3.4(b)) was taken after the sample was tilted (position 2) where the [010] zone axis is on edge. The two reference vectors $\mathbf{r}_1$ and $\mathbf{r}_2$ are coincident with the $(10\bar{1})$ and $(\bar{1}0\bar{1})$ spots, respectively. The third vector $\mathbf{r}_3$, which is in the z direction and calculated by vector product, has components (0.333, 0.584, 0.333) in reciprocal space. The angle between the x axis of the screen coordinate system and $\mathbf{r}_1$ is 50.986° and that between $\mathbf{r}_1$ and $\mathbf{r}_2$ is 90°.

The Miller indices of the surface planes and the edges of the particle were calculated separately by indexing the diffraction spot pattern and the Kikuchi pattern, as given in Table 3.3. The results show that the hematite particles are enclosed by high-index facets.
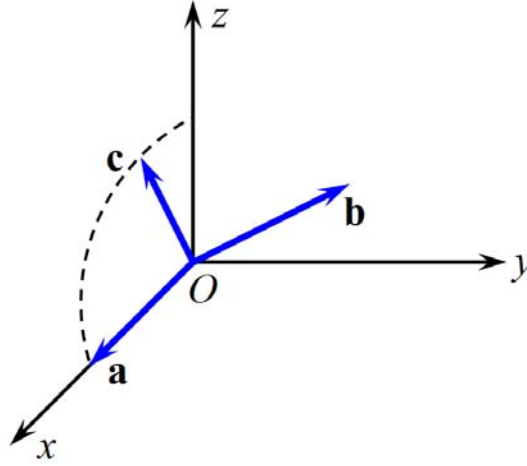
Figure 3.5 Relationship between the Cartesian system and the lattice base.

3.4   Conclusions

In conclusion, a new method for determining the crystalline planes and directions of the surface facets and edges of nanoparticles has been proposed in this paper. By determining the edge vectors and then the plane normal vector of a surface facet in TEM screen coordinate mode, their Miller indices can be calculated through coordinate transformation. The method offers a general and systematic way of characterizing the surface crystallographic features of a nanoparticle and will facilitate related studies.

Appendix

Matrix Tensors of the Direct and Reciprocal Bases

Let the crystal basis be defined by three base vectors $\mathbf{a}$, $\mathbf{b}$ and $\mathbf{c}$ with respective lengths a, b and c. The angles between each pair of base vectors are α, β and γ. Its reciprocal space is defined by the three lattice vectors $\mathbf{a^*}$, $\mathbf{b^*}$ and $\mathbf{c^*}$ with respective lengths a^*, b^* and c^*. The computational and algebraic aspects of these mutually reciprocal bases can be conveniently expressed in terms of the metric tensors of these bases. The matrix of the metric tensor of the direct basis G, or briefly the direct metric, is:

$$G = \begin{bmatrix} a^2 & ab\cos\gamma & ac\cos\beta \\ ab\cos\gamma & b^2 & bc\cos\alpha \\ ac\cos\beta & bc\cos\alpha & c^2 \end{bmatrix} \qquad 3.11$$

The corresponding reciprocal metric tensor is

$$G^* = \frac{1}{V^2} \begin{bmatrix} b^2c^2\sin^2\alpha^2 & abc^2(\cos\alpha\cos\beta - \cos\gamma) & ab^2c(\cos\alpha\cos\gamma - \cos\beta) \\ abc^2(\cos\alpha\cos\beta - \cos\gamma) & a^2c^2\sin^2\beta^2 & a^2bc(\cos\beta\cos\gamma - \cos\alpha) \\ ab^2c(\cos\alpha\cos\gamma - \cos\beta) & a^2bc(\cos\beta\cos\gamma - \cos\alpha) & a^2b^2\sin^2\gamma^2 \end{bmatrix} \quad 3.12$$

in which $V^2 = a^2b^2c^2(1 + 2\cos\alpha\cos\beta\cos\gamma - \cos^2\alpha - \cos^2\beta - \cos^2\gamma)$. With the above two

equations, the vector calculations and the coordinate transformation of the vectors between the two bases can be easily realized.

Coordinate Transformation Matrices Between the Cartesian Crystal Coordinate System and the Direct Lattice Space and its Reciprocal Space

With the automatic Kikuchi pattern-indexing software packages, such as KHL's *CHANNEL* software package, TSL's OIM software and EP, the crystallographic orientation of a crystal can be determined by indexing the Kikuchi patterns of the crystallite. The orientation of the crystallite is always expressed by a set of rotations (Euler angles) from the sample coordinate system to the Cartesian coordinate system attached to the crystal. Therefore, the coordinate transformation matrices from the Cartesian coordinate system to the Bravais lattice base and its reciprocal base are always required. The derivation of such matrices would be helpful for the associated calculations. According to *International Tables for Crystallography*[11], the Cartesian system is set at the same origin as the Bravais lattice base, with its x axis parallel to the base vector **a** and the base vector **c** in the xOz plane of the Cartesian coordinate system, as shown in Figure 3.5. Thus, the components of **a**, **b** and **c** in the Cartesian coordinate system are as follows:

$$a_x = a;\ a_y = 0;\ a_z = 0$$

$$b_x = b \cdot \cos \gamma$$

$$b_y = \frac{b}{\sin \beta}(1 + 2\cos \alpha \cos \beta \cos \gamma - \cos^2 \alpha - \cos^2 \beta - \cos^2 \gamma)^{1/2}$$

$$b_z = \frac{b}{\sin \beta}(\cos \alpha - \cos \beta \cdot \cos \gamma)$$

$$c_x = c \cdot \cos \beta;\ c_y = 0;\ c_z = c \cdot \sin \beta \qquad\qquad 3.13$$

Therefore, the transformation matrix from the Cartesian coordinate system to the lattice base is

$$\begin{bmatrix} a_x & b_x & c_x \\ 0 & b_y & 0 \\ 0 & b_z & c_z \end{bmatrix} \qquad\qquad 3.14$$

and the transformation matrix from the lattice base to the Cartesian coordinate system is

$$\begin{bmatrix} \dfrac{1}{a_x} & \dfrac{b_z c_x - b_x c_z}{a_x b_y c_z} & -\dfrac{c_x}{a_x c_z} \\ 0 & \dfrac{1}{b_y} & 0 \\ 0 & -\dfrac{b_z}{b_y c_z} & \dfrac{1}{c_z} \end{bmatrix} \qquad\qquad 3.15$$

The transformation matrix from the Cartesian coordinate system to the reciprocal base is

$$\begin{bmatrix} \dfrac{1}{a_x} & 0 & 0 \\[2ex] \dfrac{b_z c_x - b_x c_z}{a_x b_y c_z} & \dfrac{1}{b_y} & -\dfrac{b_z}{b_y c_z} \\[2ex] -\dfrac{c_x}{a_x c_z} & 0 & \dfrac{1}{c_z} \end{bmatrix}$$

3.16

and the transformation matrix from the reciprocal base to the Cartesian coordinate system is

$$\begin{bmatrix} a_x & 0 & 0 \\ b_x & b_y & b_z \\ c_x & 0 & c_z \end{bmatrix}.$$

3.17

Reference

[1] Narayanan, R.; El-Sayed, M. *Nano Lett.* **2004**, *4*, 1343–1348.

[2] Xiong, Y.; Wiley, B. J.; Xia, Y. *Angew. Chem. Int. Ed.* **2007**, *46*, 7157–7159.

[3] Orendorff, C. J.; Gole, A.; Sau, T. K.; Murphy, C. J. *Anal. Chem.* **2005**, *77*, 3261–3266.

[4] Maillard, M.; Giorgio, S.; Pileni, M.-P. *J. Phys. Chem. B* **2003**, *107*(11), 2466–2470.

[5] Tian, N.; Zhou, Z.-Y.; Sun, S.-G.; Ding, Y.; Wang, Z. L. *Science* **2007**, *316*(5825), 732–735.

[6] Lee, S.-M.; Cho, S.-N.; Cheon, J. *Adv. Mater.* **2003**, *15*, 441–444.

[7] Stekolnikov, A. A.; Bechstedt, F. *Phys. Rev. B* **2005**, *72*, 125326.

[8] Zaefferer, S. *Advances in Imaging and Electron Physics* **2002**, *125*, 356–415.

[9] Xiang, Y.; Wu, X.; Liu, D.; Jiang, X.; Chu, W.; Li, Z.; Ma, Y.; Zhou, W.; Xie, S. *Nano Lett.* **2006**, *6*, 2290–2294.

[10] Lee, S.-M.; Jun, Y.-W.; Cho, S.-N.; Cheon, J. *J. Am. Chem. Soc.* **2002**, *124*(38), 11244–11245.

[11] Hahn, T. *International Tables for Crystallography;* Dordrecht: Kluwer Academic Publishers, 4 ed., 1996.

[12] Bunge, H. J.; Esling, C.; Muller, J. *Acta Cryst. A* **1982**, *37*, 889–899.

[13] Morawiec, A. *J. Appl. Cryst.* **1999**, *32*, 788–798.

[14] Morawiec, A.; Fundenberger, J.-J.; Bouzy, E.; Lecomte, J.-S. *J. Appl. Cryst.* **2002**, *35*(2), 287.

Chapter 4   Photocatalytic Performance of Iron Oxide Nanoparticles

The degradation reactions of organic molecules over semiconductor photocatalysts mainly occur on the surface of the solid.[1] It is generally accepted that the photocatalytic efficiency is determined by surface atomic structure and surface properties of photocatalyst. For inorganic nanoparticles synthesized by chemical route, the proportion of the crystallographic planes, the atomic ratios of atoms on surface corners and edges positions can be tuned by controlling the shape of particles in nanoscale.[5, 2] That means the coordination of surface atoms and thus adsorption behavior of organic molecules on the solid surface may be altered. Considering the significant role of adsorption of organic molecules on photocatalyst surface for the degradation reactions,[38, 5] the photocatalytic properties of iron oxide could benefit from the controlling of the morphology. On the other hand, the surface hydroxyl plays a central role in the process of decomposing contaminants, since it captures the photogenerated holes and attacks the organics after it converts into hydroxyl free radicals.[36, 10] The DFT (Density Functional Theory) calculation and thermodynamic analysis on crystalline TiO_2 shows that both the concentration and types of surface hydroxyls existing on each crystallographic planes and their vibrating mode could be affected by morphology.[34] Similar morphology dependence of surface hydroxyl configuration has also been found on iron oxide.[14]

In recent years, environmental remediation by using semiconductor photocatalyst under solar radiation has attracted much attention. Among various semiconductors, TiO_2 has been the most extensive investigated material for photocatalytic applications due to high quantum efficiency under UV light irradiation and chemical stability. However, widespread utilization of TiO_2 is impaired by its wide bandgap of 3.1 eV which lies in the UV region of solar spectrum and making TiO_2 can only utilize 4% of the incident solar radiation. Although many efforts have been made to extend it to the visible light responsive region, the improvement in photocatalytic activity is still limited. And in some cases, the improvement in photocatalytic activity is at the expense of chemical stability. For instance, the doped TiO_2 which can respond to visible light is less stable than the undoped one.[10, 5] Therefore, with respect to both applied and fundamental points of views, it is important to develop non-TiO_2 photocatalysts with high response to visible light. Iron oxide is expected as a promising candidate for visible light

photocatalyst due to its low cost, large abundance in earth crust, environmental compatibility, as well as proper band gap of 2.2 eV which lies in the visible region of solar spectrum and allows absorption of 45% of the solar energy. The main drawback for iron oxide to be used as photocatalyst is that hole diffusion length in iron oxide is low compared with that in TiO_2. However, recently studies showed that this problem can be avoided by controlling the particle morphology.[12, 13] Rosso *et al.* investigated the anisotropy of electrical resistivity and concluded that there is a surface electric potential gradient across a crystal when there are two or more structurally distinct facets exposed to solution.[60] This finding was reviewed as a 'new route to improve the photocatalytic performance of hematite.'[15] The mobility characteristics of charge carries in iron oxide nanoparticles can be well tuned by controlling the shape of the particles, and its photocatalytic activity can thus be improved as a result of prolonging the existing time of electron-hole pairs.

In this chapter, methyl orange (MO), a representative azo dye contaminant molecule in textile industry, was chosen as a probe molecule to investigate the photocatalytic activity of iron oxide nanoparticles synthesized in Chapter 2.

4.1   Materials and Facilities

The following chemicals with AR purity were used for hydrothermal synthesis of iron oxide nanostructures. All reagents were used as received without any further purification.

ferric chloride ($FeCl_3 \cdot 4H_2O$), AR, SinoPharm, Shanghai

3-aminopropanol

urea (CON_2H_4), AR, SinoPharm

polyethylene glycol (PEG, M=20 k), AR

methyl orange (MO), AR, Shenyang Reagents Co., Ltd.

anhydrous ethanol, AR, Shenyang Reagents Co., Ltd.

sodium hydroxide (NaOH), AR, SinoPharm

4.2   Preparation of Iron Oxide Photocatalysts

Based on the mechanism investigation on the growth of iron oxide in constrained environments, iron oxide nanoparticles of different morphologies were synthesized by controlling the synthesis conditions, including temperature, pH, stabilizers, etc.

In a typical process for synthesizing hematite, it was prepared by mixing the variable amounts of sodium hydroxide into aqueous solution of iron salts followed by addition of surfactant solution. A red precipitation occurs immediately in the solution. The surfactants were solvent of 1 wt.% 3-aminopropanol, PEG and urea, respectively. The overall concentration of
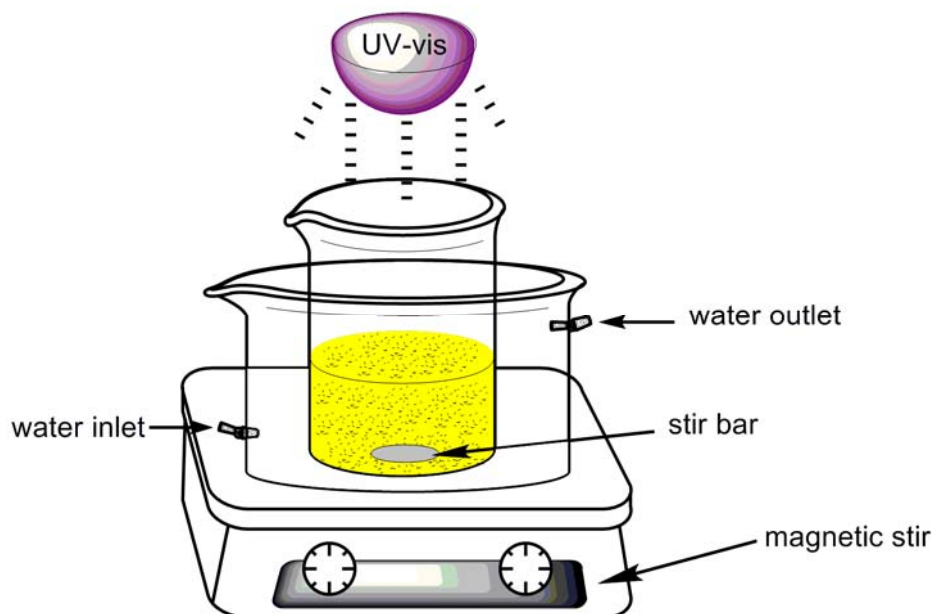
Figure 4.2 Schematics of UV-visible photocatalytic reactor.

Fe in the final precursor was fixed at 0.1M. Subsequently, the mixture was vigorously stirred at room temperature for 30 min under nitrogen atmosphere. The final suspension was transferred to 120 ml Teflon-line autoclave and heated at 180°C for 10 hours. When the reaction was completed, the nanoparticles with solution were filtered and washed by using ethanol and de-ionized water, respectively. The as-obtained products have a red color and were characterized without any size or shape selection process.

4.3   Evaluation of Photocatalytic Activity

Photocatalytic activity of iron oxide was evaluated in a 250 mL homemade photoreactor under an ultraviolet A (UVA) illumination with peak wavelength, $\lambda \sim 365$ nm, as shown in Figure 4.2. The light irradiation was provided by a 200 W high-pressure mercury lamp which was placed 10 cm above the slurry surface. The temperature of the suspension was maintained at 20°C by using a circulated water to eliminate the heating effect of light irradiation. The MO solution after adding iron oxide powders was magnetically stirred in the dark for 30 min to establish the adsorption-desorption equilibrium prior the photoreaction. Magnetic stirring was kept during the reaction process. The color of the suspension faded along with the illumination
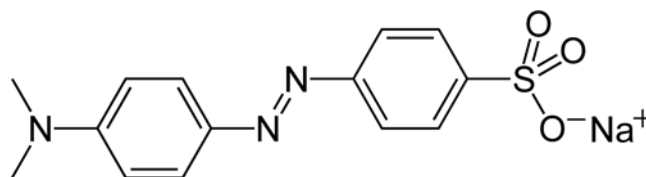

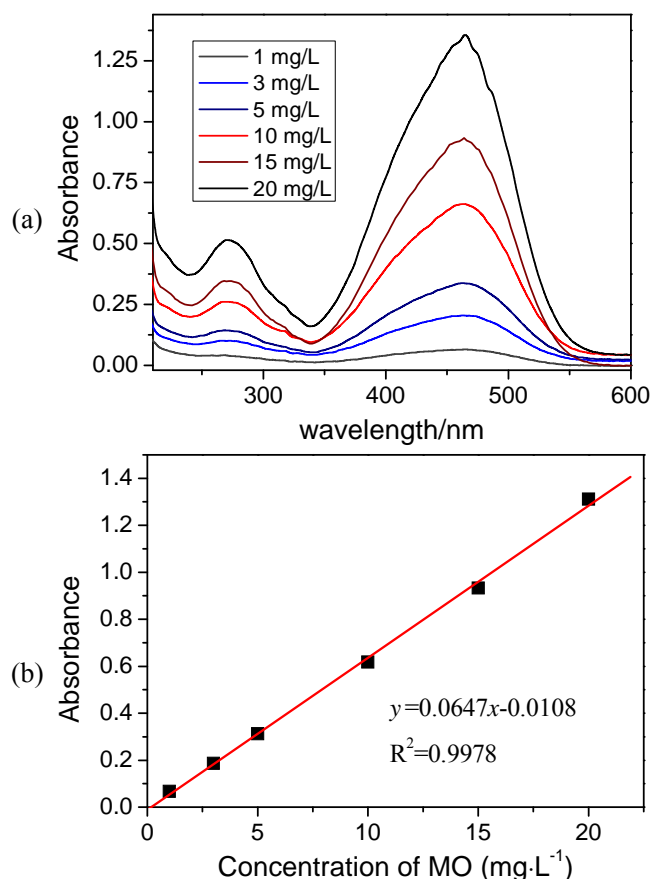Figure 4.1 Molecular structure of methyl orange dye used in this study.

Figure 4.3 The standard calibration curve of methyl orange solutions used to evaluate its degradation rate in this study: (a) UV-vis spectrum of MO aqueous solutions at different concentrations, (b) MO concentration dependence on absorbance at 464 nm.

time.

Methyl orange (MO, Figure 4.1), a representative azo dye contaminant in textile industry, was used as a probe molecule to evaluate the photocatalytic activity of iron oxide. The degradation of MO and the decolorization of the solution were determined by a UV-vis spectrometry. The characteristic wavelength of MO in the UV-vis adsorption spectrum is at 464 nm which was used to calculate the concentration of MO solution by Lambert-Beer's law. In order to get concentration data from the spectrum, standard calibration curve was firstly setup for MO solutions with concentration lower than 20 mg·L^{-1}. The results depicted in Figure 4.3 shows that the linear relationship between absorbance and concentration of the MO solutions. The fitting equation between the two parameters is:

$$A = 0.0647C - 0.0108 \qquad R^2 = 0.9978 \qquad\qquad 4.1$$

The fitting equation proved the applicability of the Lambert-Beer's law. The decomposition ratio can be calculated by the following:
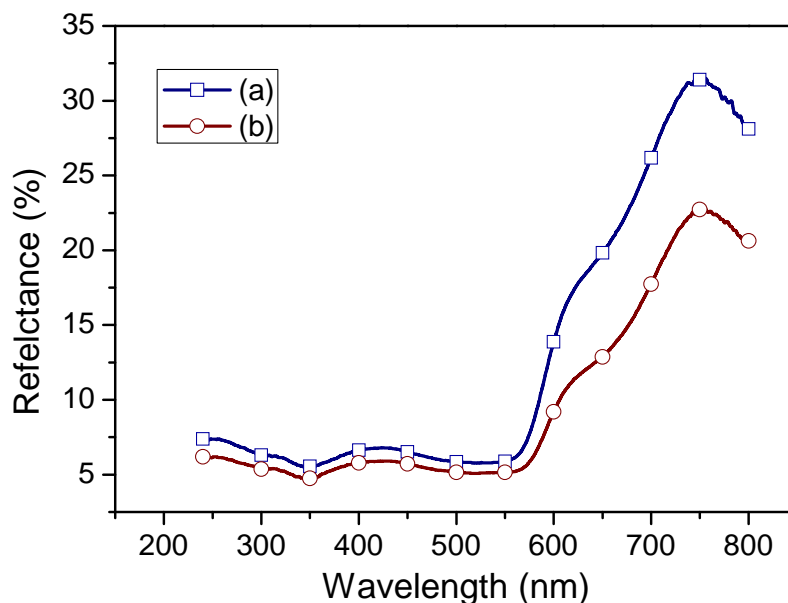
Figure 4.4 Absorption spectra of hydrothermally synthesized hematite nanoparticles prepared in the presence of (a) urea and (b) 3-aminopropanol.

$$r = \frac{C_0 - C_t}{C_0} \times 100\% \qquad 4.2$$

in which C_0 and C_t represent the concentration of the MO solution after illumination for 0 min and t min.

4.4   Optoelectronic Properties of Hematite

The optical of Fe_2O_3 nanocrystals were examined by UV-vis absorption spectroscopy. Diffuse reflectance spectra were recorded on a UV-vis-NIR spectrometer (Lambda 600, Perkin-Elmer, MA) using $BaSO_4$ as reference. Figure 4.4 shows the measured reflectance spectra of hematite nanoparticles synthesized by hydrothermal technology in the presence of urea and 3-aminopropanol. Absorption spectra that are dominated by strong light scattering bands are observed and can be attributed to the relatively large sizes of the particles.[16] Furthermore, it can be seen that polyhedral particles show higher reflectance than platelet in the UV-visible light range. And the reflectance difference is increased when the wavelength exceeds 625 nm.

Measuring the diffuse reflectance spectrum is also the most direct and simplest way to determine the band gap of semiconductors. The Kubelka-Munk equation can be used to determine the absorption coefficient[17]:
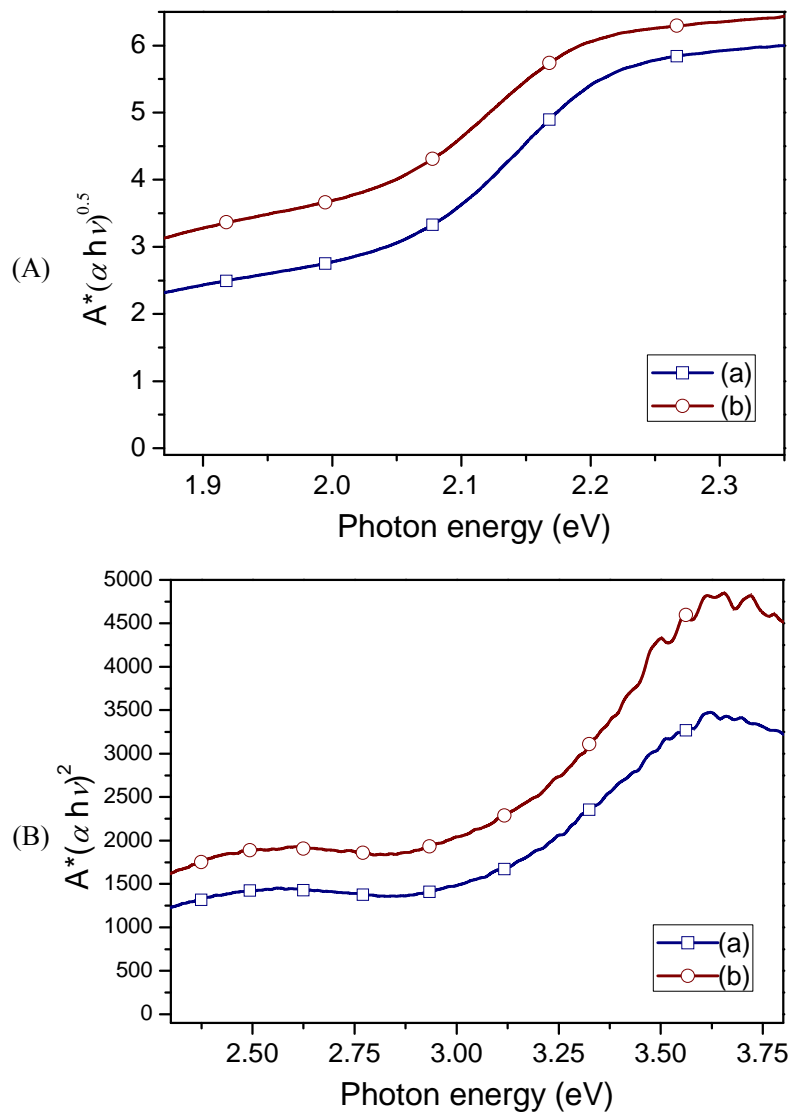
$$\frac{(1-R)^2}{R} = \alpha \qquad 4.3$$

Figure 4.5 Calculation of (A) indirect and (B) direct electronic transition. (a) hematite synthesized with urea, (b) synthesized with aminopropanol.

In the light absorption process, a photon of a known energy excites an electron from a lower energy valance band to a higher-energy conduction band. For allowed direct transitions, the lowest position in conduction band is normal to the peak position of valance band. Vertical direct transition may occur after absorbance of photos with energy $hv > E_g$. In this case, the absorption coefficient is determined by:[76, 19]

$$\alpha = A * \frac{(hv - E_g)^{1/2}}{hv} \qquad 4.4$$

in which $A*$ is a parameter related with efficient mass of electron and hole, and is given by[19]:

Table 4.1 Optical bandgap and absorption edge wavelength of hematite of different shapes.

	indirect band gap (eV)	corresponding wavelength (nm)	direct band gap (eV)	corresponding wavelength (nm)
polyhedron	1.85	673.7	2.61	477.6
plate-like	1.92	649.2	2.74	454.9
Calculation[79]	2.0	623.0	3.50	356.1

$$A^* \approx \frac{q^2 \left(2\frac{m_h^* m_e^*}{m_h^* + m_e^*} \right)^{3/2}}{nch^2 m_e^*} \qquad 4.5$$

For indirect transition, the energy surface of conduction band shift relative to that of valance band. Absorption and emission transition of phonons occur along with the transition of electrons from basic states to excited states. In this case, the absorption coefficient can be determined by the following,[76, 19]

$$\alpha = B\frac{(h\nu - E_g)^2}{h\nu} \qquad 4.6$$

where B is the absorption constant. The formula above can be used to estimate the band gap and onset of the electronic transitions. Figure 4.5 shows the converted plots of the absorption spectra of iron oxide according to Eq. 4.4 and 4.6. The direct allowed and indirect forbidden band gaps were calculated from the plots and were illustrated in Table 4.1. From the table one can see that hematite of the polyhedron and plate-like exhibit an indirect transition below 2 eV and direct transition at about 2.6 eV. The values are smaller than existing reported ones.[79] It has been proposed that the indirect transition corresponds to a spin-forbidden Fe^{3+} $3d \rightarrow 3d$ excitation. While the direct transition is due to the O^{2-} $2p \rightarrow Fe^{3+}$ $3d$ charge transfer.[76, 79] It is worthy to note that the indirect band gap of polyhedrons is slightly smaller that that plate-like hematite nanoparticles.

4.5 Photocatalytic Results and Discussions

4.5.1 Hematite Dosage Optimization

Photocatalysts and organic contaminant solutions form dispersed suspensions. Degradation of organic pollutants will generally increase with catalyst dosage due to a higher surface catalytic area which is available for adsorption and degradation of the organics over the semiconductor surface. However, the presence of excessive photocatalyst may reduce the light pene-
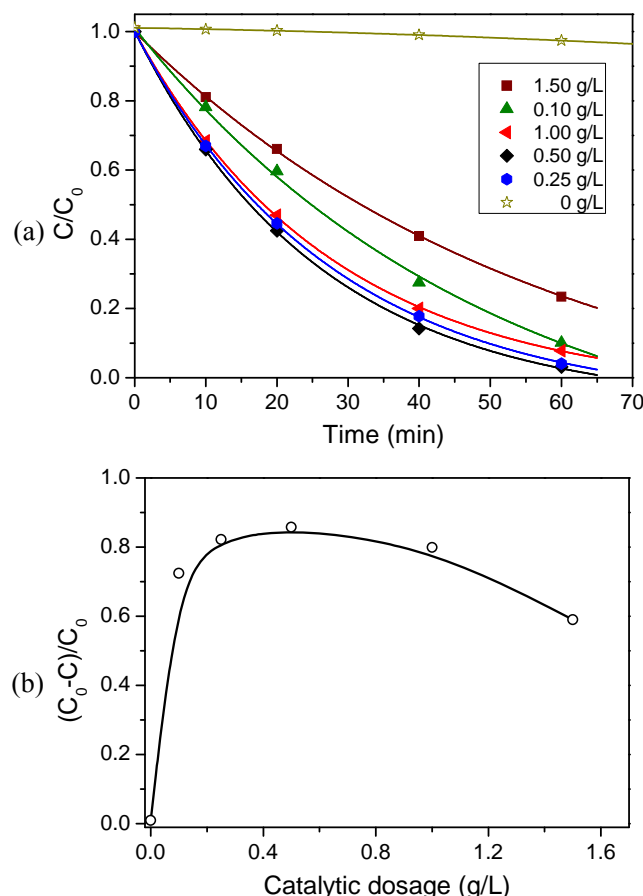
Figure 4.6 (a) Concentration changes of MO molecules under UV-vis irradiation in dispersion with different photocatalyst dosage. (b) The degradation efficiency in relation to the catalyst dosage after catalyzed for 40 min. C_0=15 mg·L^{-1}.

tration in the solution and cause a consequent rate decrease. The catalyst dosage was optimized to facilitate the successive research.

As shown in Figure 4.6(a), the curve assigned by ★ represents the dependence of MO concentration on illumination time in the absence of iron oxide. It shows that the photolysis of MO molecules is slow under 365 nm light irradiation which is in agreement with previous reported results.[10] In the experiments, the dosage of hematite was 0.1, 0.25, 0.5, 1.0 and 1.5 g·L respectively. When the dosage of hematite increased from 0.1 g·L to 0.5 g·L, the rate of MO degradation became higher. However, the degradation rate lowers if more catalyst powders were added into the reaction system.

Figure 4.6(b) gives the degradation efficiency of dye molecules after catalyzed for 40 min with different hematite dosage. The dependence of reaction efficiency on catalyst dosage clearly shows that there is an optimized dosage. This can be explained as the follows. When concentration of photocatalyst in slurry is low, the surface area of iron oxide and active sites can be increased as a result of adding more catalysts. However, excessive dosage of iron oxide
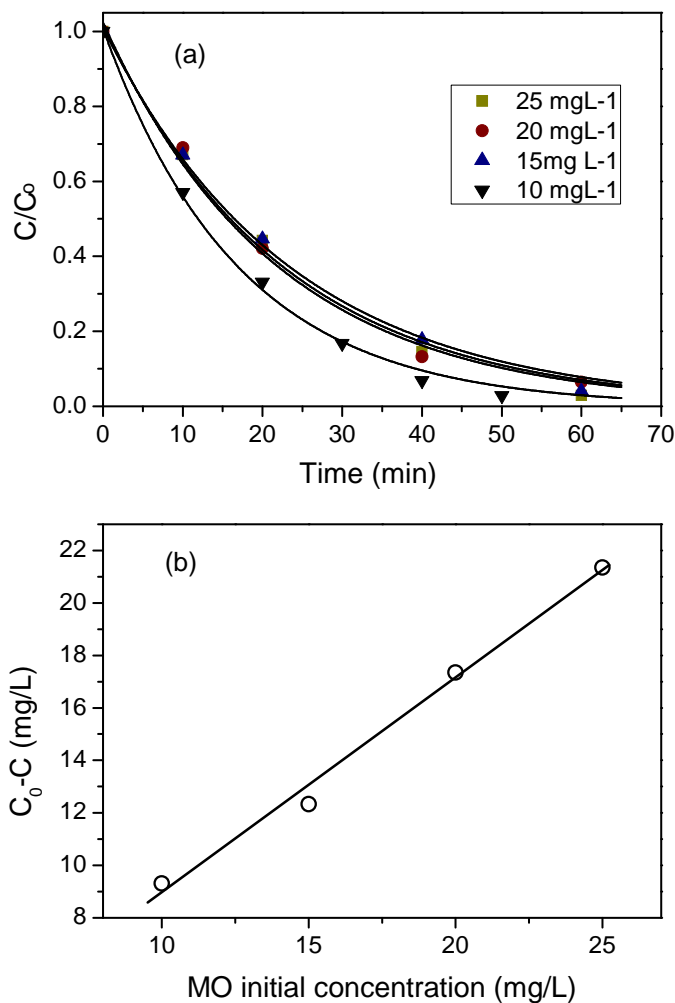
Figure 4.7 (a) The effect of initial concentration of MO on its photocatalytic decomposition. (b) The relationship between concentration variation after 40 min irradiation and initial concentration of MO.

could also limit the penetration of incident light in the slurry and result in quick decay of the light intensity. As a result, 0.5 g·L was selected as the optimal dose to reduce the light scattering and reflection in the dispersion.

4.5.2 Influence of initial concentration of dyes

It is agreed that the essence of photodecomposition of organic contaminants by semiconductors is of charge transfer reactions between adsorbed species and photo-induced free radicals (e.g. holes, $HO^{\bullet}$ and $O_2^{\bullet}$). Therefore, the coverage of contaminants molecules on surface of semiconductors affects the reaction rate. To investigate the influence of initial methyl orange concentration, experiments on the photocatalytic oxidation of MO were conducted for solutions with various MO concentrations: 10 mg·L , 15 mg·L , 20 mg·L and 25 mg·L over hematite nanoparticles synthesized in Chapter 2. Figure 4.7 shows the total concentration of MO as a

function of irradiation time, measured with different initial MO concentration at a natural pH. In all cases, the dye concentration has an exponential relationship with irradiation time, suggesting that the reactions follow first order kinetics. Thus the variation of MO concentration along with time can be written as follows:

$$\ln(C_0 / C_t) = kt \qquad\qquad 4.7$$

where k is apparent rate constant. The first order kinetic equations, apparent rate constant, as well as half-concentration time $t_{0.5}$ of reactions with different initial MO concentration can be derived by fitting $C_t / C_0 \sim t$ using the above equation. The results are shown in Table 4.2.

From the calculation results in Table 4.2, one can see that the apparent reaction rate constant k decreases from 0.0589 to 0.0427 when the MO concentration varies from 10 mg·L to 15 mg·L. Noticed that the increasing aliquots of photons were adsorbed by methyl orange molecules at higher MO concentration, some researchers attribute the decrease of the rate constant with the increase of initial dye concentration to the significant adsorption of light by the substrate in the same wavelength range of the catalysts excitation.[28] While in this situation, the decreasing of rate constant k would keep going with even higher initial MO concentrations. However, a saturation phenomenon of reaction rate constant over MO concentration was observed since the constant k remains almost the same value at initial concentrations higher than 10 mg·L.

Here we propose a different explanation. In slurry photocatalytic system, the degradation of organic molecules is achieved mainly through two routes, namely, the decomposition at the photocatalyst surface and by attack of reactive radicals (such as $\cdot$OH and $\cdot HO_2$). For the former one, the pollutant molecules must reach the surface of the catalyst to be oxidized. Whereas in the later process, reactive radicals, carrying the photogenerated charges, swim in the solution and transport the charges to organic molecules. In both cases, the rate of charge transfer from the catalyst or radical to organics is much faster than the diffusion of organics or the radicals in the solution.

Firstly, we discuss the diffusion of the methyl orange in solutions. From the viewpoint of kinetics, only organic molecules that have pre-adsorbed on the surface of solid can be oxidized by the surface charges. For photocatalysts in slurry system, the active surface sites are determined by the dosage of the catalysts. We believe that most of MO molecules have been adsorbed on the surface of α-Fe_2O_3 during the mixture process before light illumination if their concentration is low ($C_0 \leq 10$ mg·L^{-1}). When this system is exposed to light illumination, dye molecules are oxidized immediately, thus demonstrating a high reaction rate. On the other hand,

when the initial concentration is high, many methyl orange molecules scatter in the solution except some adsorbed ones on the surface of solid. Several layers of adsorbed dye molecules form on the hematite surface. Only after the surface molecules have been photocatalytic decomposed, can the molecules in solution be adsorbed and oxidized on the surface of hematite. Thus, the kinetic equilibrium is setup between consuming of molecules on solid surface and diffusion of molecules from solution to catalyst surface. And the diffusion of MO in solution is the rate controlling step because the diffusion rate is lower than the decomposition process on hematite surface.

For dye molecules decomposed by photocatalytic radicals, the degradation rate is proportional to the collision probability between the radicals and molecules. Obviously, at higher concentrations, the collision probability increases, resulting in more molecules to be oxidized in the unit time interval.

To further elucidate this point, we investigated the dependence of concentration variation on initial concentration of methyl orange. As an example, data at time interval 40 min were depicted in Figure 4.7 (b). Interestingly, a linear relationship between the concentration and the decrease in concentration was found. The results suggest that more dye molecules were oxidized in a time unit at higher initial concentrations, although the reaction rate constant remains unchanged. This is because the diffusion rate of MO and the collision probability of radicals and organic molecules are proportional to the concentration from the solution to the surface of photocatalyst. Worked by the dual functions, more dye molecules are decomposed at a higher concentration in a fixed time interval.

Table 4.2 Kinetic equations for photocatalytic reactions at different initial MO concentration and related parameters

C_0 (mg·L^{-1})	First order kinetic equation	k	$t_{0.5}$ * (min)	r_0
10	$\ln(C_t / C_0) = -0.0589t + 0.0078$	0.0589	11.90	0.5936
15	$\ln(C_t / C_0) = -0.0427t + 0.0102$	0.0427	16.47	0.6471
20	$\ln(C_t / C_0) = -0.0461t + 0.0238$	0.0461	15.52	0.9442
25	$\ln(C_t / C_0) = -0.0445t + 0.0163$	0.0445	15.94	1.1308

* Time required for 50% decolorization of initial methyl orange concentration.

The initial rate of MO decomposition r_0 can be obtained by derivation of first order equations in Table 4.2 at $t = 0$. Figure 4.8(a) shows that r_0 increases with increasing initial MO concentrations from 10 mg·L to 25 mg·L, suggesting that the degradation of MO occurs on the surface of α - Fe_2O_3 and reaction rate is proportional to the surface adsorption of MO molecules. In 1998, G. Pan and P. Liss proposed the metastable-equilibrium adsorption theory (MEAT) which states that the adsorption density of organics on solid surface is not a state variable.[22] According to Pan's theory, the adsorption density is determined by binding energy and adsorption configuration, and could reach equilibrium with the concentration of species in solution. In this experiment, the coverage of MO on surface of α - Fe_2O_3 increases with concentration of MO in solution, thus the efficiency of charge carriers transfer from solid to MO molecules may get enhanced, leading to a raise in r_0.

As proved by many works,[38, 12-26] the reaction kinetics of decomposing organics by photocatalysis on oxide semiconductors can be described by Langmuir-Hinshelwood model:

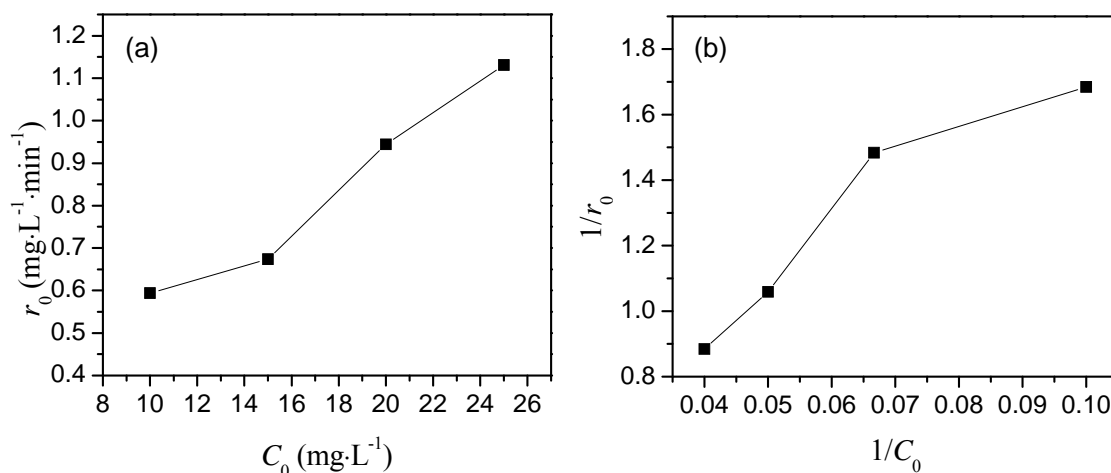$$r = \frac{kKC}{1 + KC}$$ 4.8 (a)

Figure 4.8 (a) The initial reaction rate r_0 as a function of MO initial concentration C_0; (b) The relationship between $1/r_0$ and $1/C_0$.

$$\frac{1}{r_0} = \frac{1}{kK}\frac{1}{C_0} + \frac{1}{k}$$ 4.8 (b)

in which: C — concentration of organics;

k — apparent reaction rate constant;

K — apparent adsorption equilibrium constant;

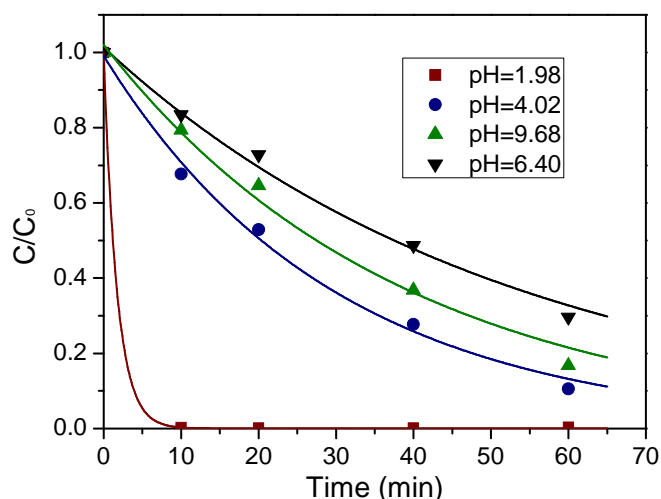C_0 — initial concentration of organics.

Figure 4.9 The decay curves for methyl orange at different pH. C_0=15 mg·L^{-1}.

Studies on kinetics of photocatalytic reactions show that adsorption of organic molecules on surface of photocatalyst is the precondition of application of Langmuir-Hinshelwood equations[10, 27]. However, people have different opinions on the mechanism of degradation of organic photocatalyzed by α-Fe$_2$O$_3$ for a long time. Some argued that the photoreactions occurring at the solid-liquid interface are photoinduced ligand-to-metal charge transfer process[28]. Recent research works have more supports for semiconductor photocatalysis process[29, 30]. Xu *et al.* investigated the relationship between the amount of adsorption and reaction rate of orange II over iron oxide, and also confirmed that the reaction occurs on the catalyst surface[38]. Therefore, the Langmuir-Hinshelwood modal can be applied to study the kinetics of photocatalytic reactions using hematite as catalyst. Figure 4.8 shows the relationship between $1/C_0$ and $1/r_0$. The linear relationship when the initial concentration $C_0 \geq 15 \, \text{g} \cdot \text{L}^{-1}$ suggests the applicability of the Langmuir-Hinshelwood equation and provides further support on insufficient coverage of hematite surface at concentrations lower than 10 mg·L .

4.5.3 Effect of pH on Photodegradation of MO

The heterogeneous photocatalysis has been found to be pH dependent due to the following reasons: 1) the surface charge properties of photocatalyst (especially for oxide semiconductors) could be altered by pH of solutions, as a result, the adsorption performance of organic molecules on catalyst surface could be changed. 2) the active radicals which are important for photocatalytic reactions, such as ·OH and ·HO$_2$, may be generated from H$^+$ or OH$^-$ in solution by scavenging the photo-induced charge carriers. 3) in some cases, the molecular structure of contaminants may be different when pH of solution changes, and becomes easier to decompose. By now, the effect of pH on degradation of the pollutants is explored mainly based
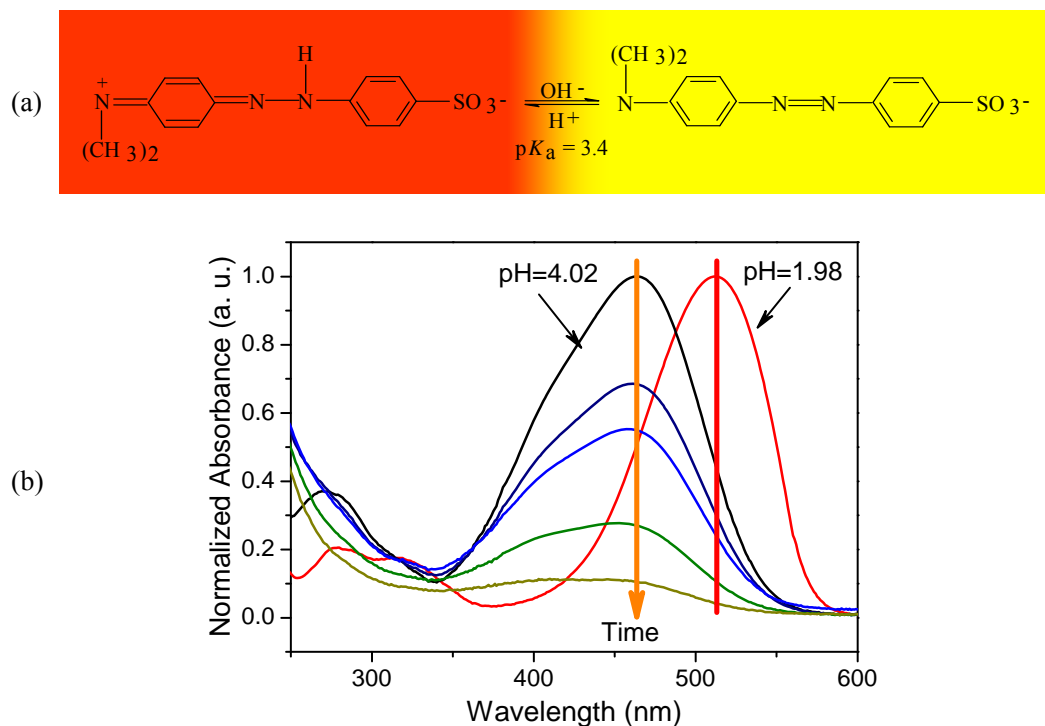
Figure 4.10 (a) Schematic diagram of conjugated structure of methyl orange at different pH in solutions. The red quinonoid form converts into yellow alkaline azo formula at pH of 3.4. (b) UV-vis spectra of MO solutions at pH=1.98 and at pH=4.02 after photocatalytic decay over hematite for 0, 10, 20, 40, and 60 min.

on TiO$_2$ and the results are variable and controversial.[28, 30] To make clear the mechanism of dye degradation photocatalyzed by hematite, the degradation kinetics of MO was investigated at different pH values.

Figure 4.9 shows the normalized concentration of methyl orange as a function of irradiation time, measured at pH of 1.98, 4.02, 6.40 and 9.68. Fastest decay of methyl orange was obtained at pH=1.98 and followed by pH=4.02, 9.68 and 6.40. Since the point of zero charge of hematite is at pH=6.5,[31] the surface of hematite is covered by OH$^-$ under basic environment. Active radical $\cdot$OH can be generated on the surface when the catalyst is illuminated by light. The process can be expressed by

$$Fe^{III} - OH^- + h^+ \rightarrow Fe^{III} + \cdot OH^- \qquad 4.9$$

Although there is no exact explanation about how $\cdot$OH leaves the surface of solid and swims into the solution to attack the organics, it has been widely recognized that the product of $\cdot$OH is in favor of the photocatalytic reactions.[28, 25, 30]

Surface hydroxylation induced by increasing the pH of the solution is not the only cause that affects the reaction kinetics. As shown in Figure 4.10(b), the peaks of absorbance spectra shift
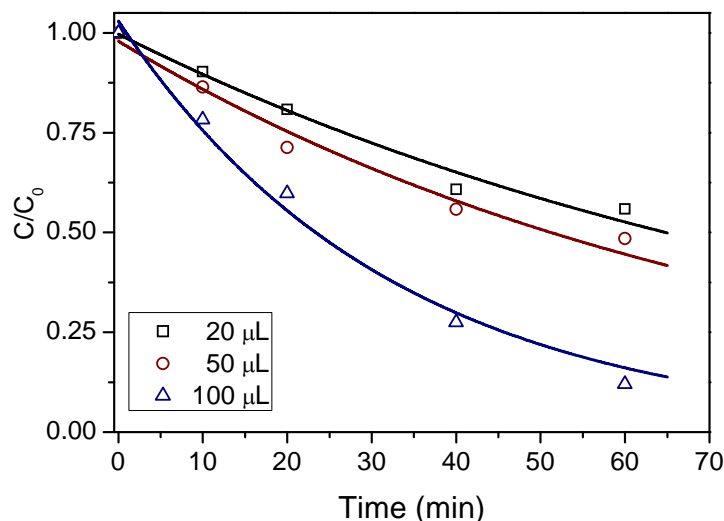
Figure 4.11 The effect of H_2O_2 on the photocatalytic activity of hematite. The net volume of the reaction solution is 100 ml.

from 466 nm at pH=4.02 to 510 nm at pH=1.98, implying the structure variation caused by pH. This can be explained by a reversible structure transformation between yellow alkaline azo formula and red quinonoid mode at pH=3.4 (Figure 4.10(a)). Because the binding energy of N=N is much higher than that of N-N bond, the quinonoid structure is easier than azo structure to be decolorized by photocatalytic reactions on α-Fe_2O_3.
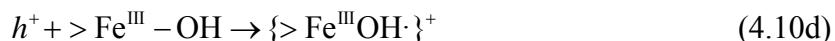
In summary, the structure conversion to quinonoid form is the main cause for high degradation rate of MO at low pH. While the photocatalytic activity improvement in high pH is attributed to the increase of amount of free $\cdot OH$ radicals formed from surface OH^-. Co-driven by the above two factors, the lowest catalytic efficiency is obtained at pH=6.40.

4.5.4 Influence of concentration of H_2O_2

The role of the strong oxidant species additives (such as H_2O_2) has been in some case controversial. The improvement effect of H_2O_2 on photocatalytic activity of semiconductors is attributed to fact that the resulting radicals $OH^{\bullet}$ produced from H_2O_2 is capable of attacking other organic molecules or in some case could act as an alternative of the surface bound hydroxyl radicals. In addition, H_2O_2 can also serve as electron scavengers, thus the electron-hole recombination at the semiconductor surface is inhibited. In Figure 4.11, the decay of the concentration of methyl orange in the oxidation runs carried out at varying the H_2O_2 additives (from 20 μl to 100 μl) at neutral pH. As expected, when the H_2O_2 addition was increased, the rate of MO degradation was increased.

4.5.5 Mechanism of photocatalytic degradation of MO by α-Fe$_2$O$_3$

Based on discussions above, a possible mechanism on photocatalytic process of hematite to decompose pollutants is proposed. The sequence of reaction steps representing the proposed mechanism is as follows

$$Fe_2O_3 + h\nu \rightarrow Fe_2O_3(e^- + h^+) \tag{4.10a}$$

$$2H_2O + 2h^+ \rightarrow H_2O_2 + 2H^+ \tag{4.10b}$$

$$O_2 + 2e^- + H^+ \rightarrow H_2O_2 \tag{4.10c}$$

$$h^+ + > Fe^{III} - OH \rightarrow \{> Fe^{III}OH\cdot\}^+ \tag{4.10d}$$

$$h^+ + Fe^{III} - OH^- \rightarrow Fe^{III} + \cdot OH^- \tag{4.10e}$$

$$e^- + > Fe^{III}OH \leftrightarrow \{> Fe^{II}OH\} \tag{4.10f}$$

$$> Fe^{II}OH + O_{2,ad} \rightarrow Fe^{III}_{aq} + \cdot O_2^- \tag{4.10g}$$
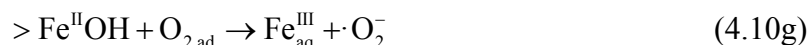
in which $>$ Fe stands for the iron ions on surface of catalyst. According to the semiconductor properties, the oxidative holes and reductive electrons are produced inside iron oxide after being irradiated by incident photons, and are captured by H_2O or dissolved O_2 in water. Reactive $\cdot OH$ radicals could be formed during the photocatalytic process at the hematite surface as the result of the interaction of H_2O or surface hydroxyl with positive holes. MO molecules decompose as a result of the attack by radicals like $\cdot OH$ or direct oxidation by surface holes.

4.5.6 The photocatalytic activities of hematite of various morphologies

The photocatalytic performance of hydrothermally synthesized hematite of different morphologies were evaluated by photodegradation of methyl orange under UV-visible light irradiation ($\lambda = 365$ nm).

- *Effect of hydrothermal temperature and treatment period*

In the growth of iron oxide nanoparticles *via* hydrothermal route, temperature and time period are two crucial factors in the hematite growth process. Varying the temperature and period can change the crystallinity and surface structure of iron oxide nanoparticles which are significant for high photocatalytic activity of hematite. Nanoparticles were grown by hydrothermal treatment of iron oxide gels with 3-aminopropanol and urea as stabilizer at temperatures from 100~160°C for different periods. Their photocatalytic activities to decompose methyl orange are given in Figure 4.12. The initial reaction rate r_0 were determined by applying Formula 4.8 and were depicted in Figure 4.13.
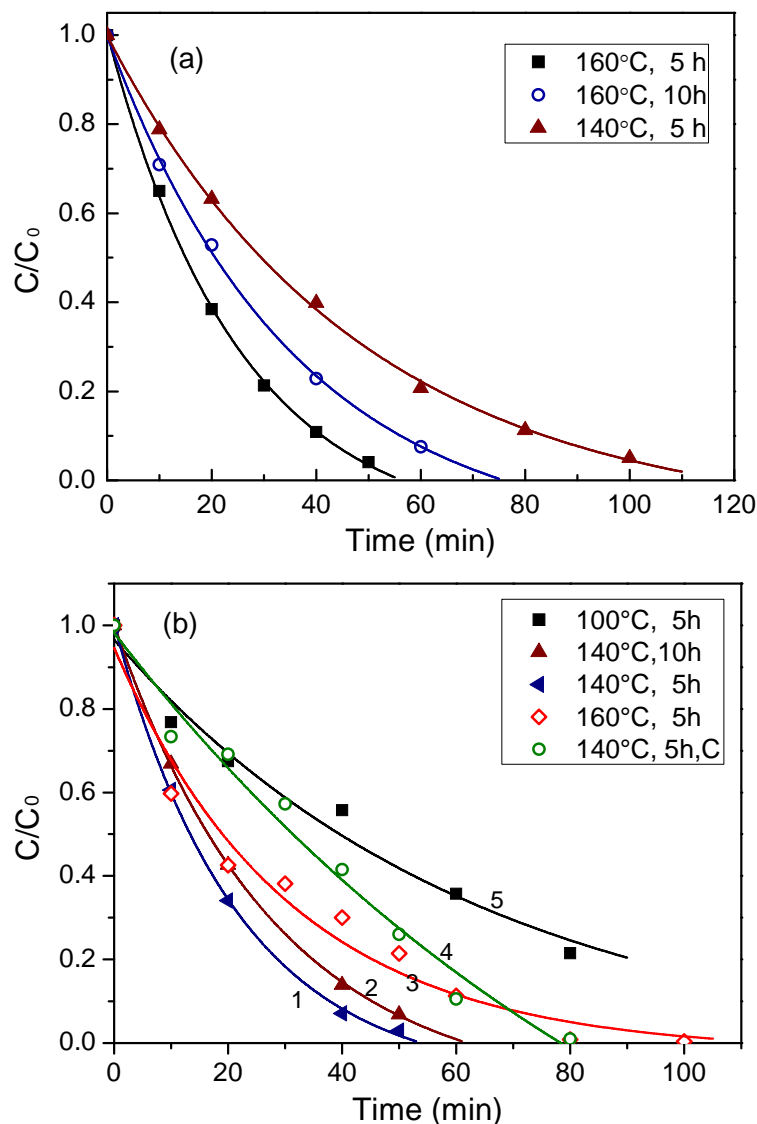
Figure 4.12 The effect of hydrothermal conditions for synthesis of hematite nanoparticles on the photocatalytic decay kinetics of methyl orange. The hematite was synthesized using (a) 3-aminipropanol and (b) urea as stabilizers. Curve 4 in (b) corresponds to hematite calcined at 500°C for 1h after hydrothermally synthesized at 140°C for 5 h. C_0=15 mg/L.

As summarized in Figure 4.13, the initial reaction rate (r_0), which is determined from the kinetics equations of methyl orange degradation over α-Fe_2O_3 nanoparticles synthesized under different conditions, is dependent on the hydrothermal temperature and period. For hematite synthesized with urea, r_0 increased in the order of (100°C, 5 h) < (160°C, 5 h) < (140°C, 10 h) < (140°C, 5 h). Notably, the photocatalytic activity variation is less relative with particle surface area, because the particle morphology changes are very small, as shown in Figure 4.15. It is well-known that the crystallinity of iron oxide plays an important role in improving the photocatalytic activities of hematite and is more important than surface area[22]. In
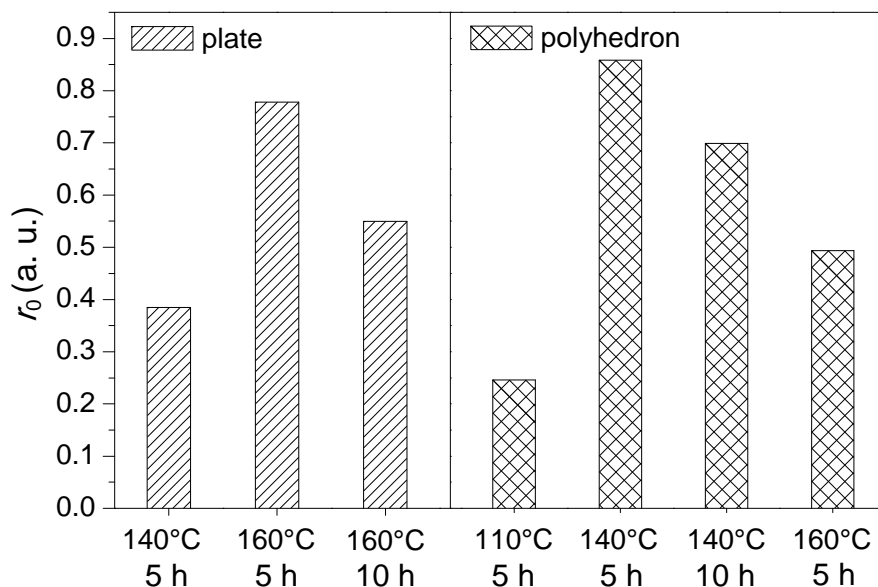
Figure 4.13 The initial rate constant r_0 of photocatalytic reactions over hematite of two morphologies fabricated under different conditions.

comparison with other synthesis routes, such as sol-gel method, microemulsion, the advantage of hydrothermal method is the product has a high crystallinity even without further sintering.

The catalytic performance enhancement may be partially due to the improvement in crystallinity of the hematite nanoparticles. From the decolorization curve of MO in Figure 4.12, one can see that the iron oxide synthesized at 100°C has the lowest catalytic activity. α-Fe_2O_3 nanoparticles synthesized at 140°C for 5 h with urea as stabilizer exhibit the highest photocatalytic activity. However, it should be noted that when prolonging the treatment period or further increasing the hydrothermal temperature, the photocatalytic properties get deteriorated, which can be attributed to the decrease of number of surface active sites[34].

For nanoparticles fabricated with 3-aminopropanol as stabilizer, the shape of the nanoparticles changes from polyhedron into plate-like. Relevant trend of photocatalytic property dependence on hydrothermal temperature and time period has been observed, as shown in Figure 4.12 and Figure 4.13. The catalytic activity decreased in the order of (160°C, 5 h) > (160°C, 10 h) > (140°C, 5 h).

To further investigate the relationship between the crystallinity and surface activity of hematite, nanoparticles related with curve 1 in Figure 4.12(b) were sintered in air at 500°C for 1 hour. The kinetics to decompose methyl orange molecules over the sintered powders was also given in Figure 4.12(b) which clearly shows that the photocatalytic performance is deteriorated after sintering. The deterioration can be assigned to the diminishment of surface active site by sintering, although the crystallinity was improved.
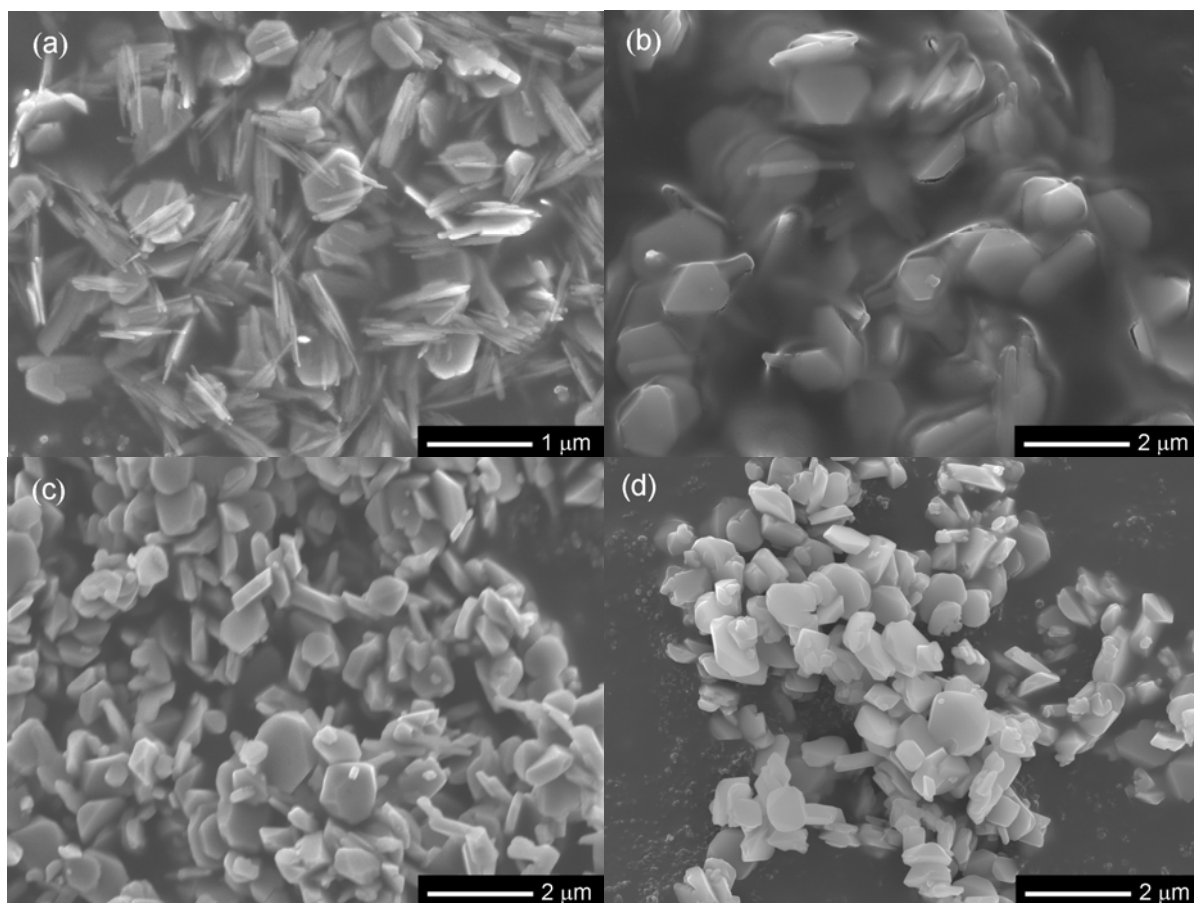
Figure 4.14 SEM morphologies of hydrothermally synthesized hematite using 3-aminopropanol as stabilizer. (a) 100°C, 5 h; (b) 140°C, 5 h; (c) 160°C, 5 h; (d) 160°C, 10 h.

Also, one can tell that the effect of stabilizer molecules on the crystallization process and surface properties of $\alpha\text{-}Fe_2O_3$ is dependent on the categories of capping groups[35]. When synthesized with 3-aminopropanol as stabilizer, hematite obtained at 160°C, 5 h exhibited higher catalytic activity than that obtained at 140°C, 5 h. However, the opposite situations occurred if urea was used as stabilizer.

The photocatalytic activities of oxide semiconductors are reported to be influenced by many factors, such as crystal structure, surface area, size distribution, as well as band structure and surface hydroxyl density.[34, 5, 19-39] Because of the semiconductor essence of hematite as a photocatalyst, crystal structure and morphology are two critical factors that can influence the others. The shape of faceted nanoparticles is determined by their exposed facets.[40] Theoretical and experimental research on surface of single crystals revealed that the catalytic efficiency of heterogeneous catalyst strongly depends on the crystallography index of surface plane, coordination of surface atoms and electronic structure, etc. Simply, the influence of shapes of hematite nanoparticles on their catalytic properties originates from the variation of surface facet of the particles.
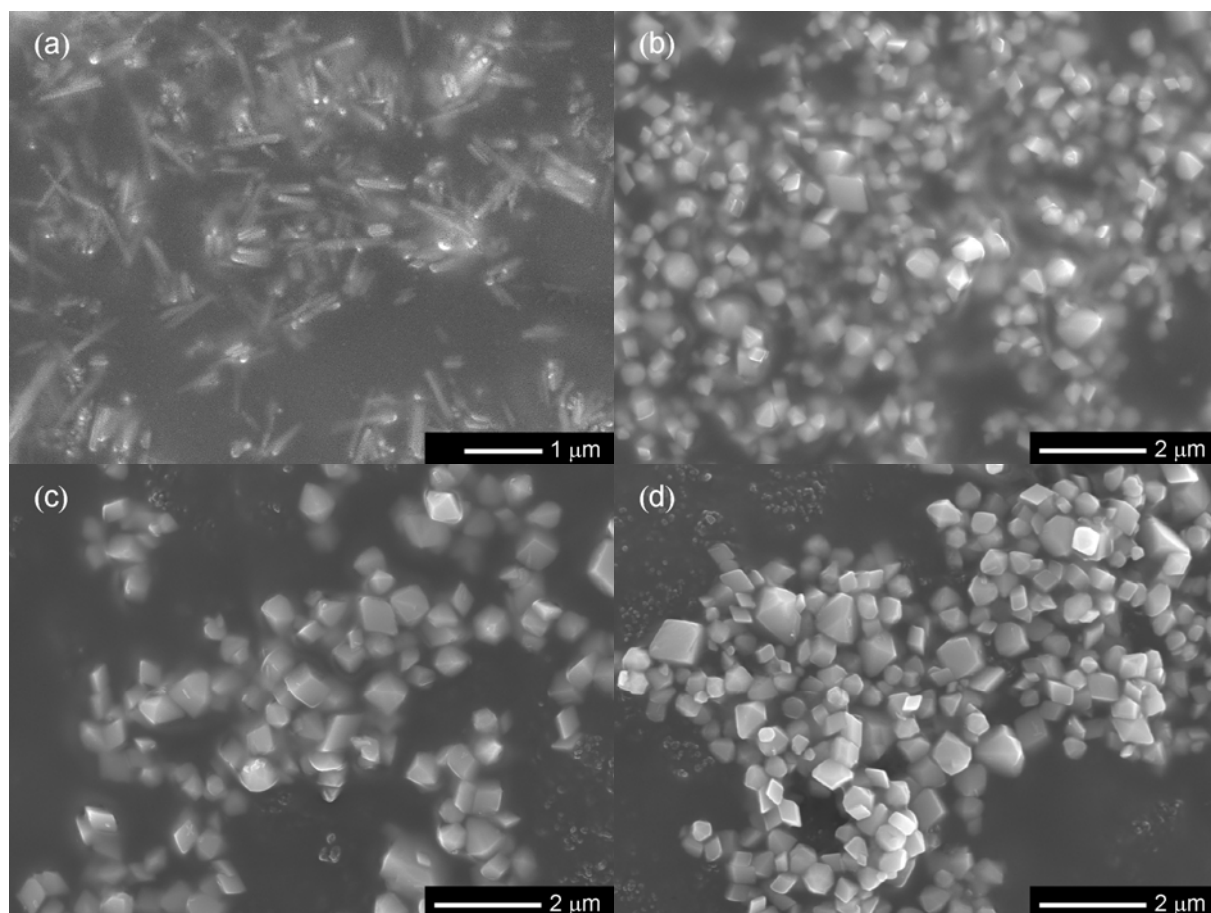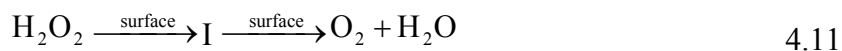
Figure 4.15 SEM morphologies of hydrothermally synthesized hematite using urea as stabilizer.
(a) 100°C, 5 h; (b) 140°C, 5 h; (c) 140°C, 10 h; (d) 160°C, 5 h.

Based on the discussion above on the photocatalytic reactions over hematite, the catalytic activity of hematite is related to the adsorption of methyl orange molecules on their surfaces. By tailoring the temperature and period of hydrothermal treatment, the active site density of hematite surface can be tuned to improve the adsorption of MO and thus accelerate their degradation rate. The optimized preparation parameters to obtain hematite nanoparticles with urea and 3-aminopropanol as stabilizer is: 160°C, 5 h and 140°C, 5 h.

4.6　Photoactivity of α-FeOOH Nanorods

Various organic pollutants could be oxidized by hydrogen peroxide in the presence of iron hydroxide. Proposed photodegradation mechanism ranges from intermediate radical formation on the surface of catalyst to oxidation of target pollutant molecules,[41] as shown in the following:
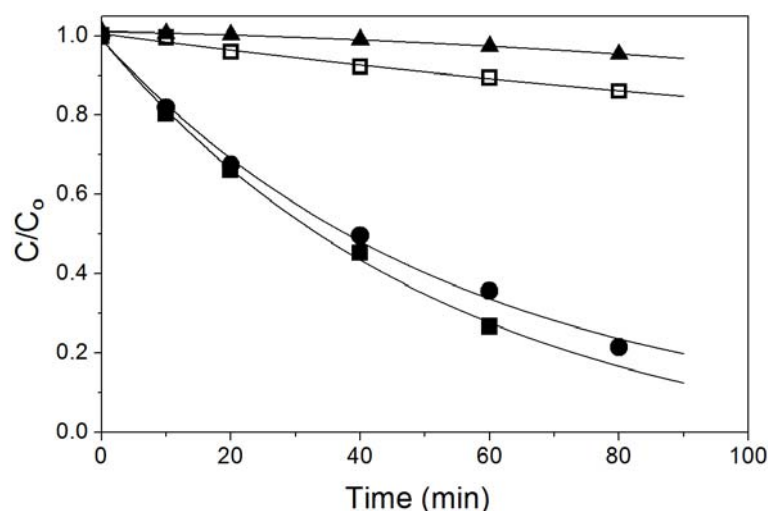
$$H_2O_2 \xrightarrow{\text{surface}} I \xrightarrow{\text{surface}} O_2 + H_2O \qquad 4.11$$

$$I + Organics \xrightarrow{\text{solution}} Products \qquad 4.12$$

Figure 4.16 The photodegradation of MO under different conditions: ▲, no catalyst; □, without H$_2$O$_2$ in reaction system; ●, goethite obtained from equimolar ferric and ferrous salts as catalyst; ■, goethite synthesized by only ferric salts.

where I are intermediates, such as •OH or O$_2^-$.

Goethite nanorods synthesized in Chapter 2 were used as photocatalyst. Figure 4.16 shows the concentration of MO as a function of UV-visible light irradiation time. The results showed that MO is stable under UV-visible irradiation when there is no catalyst in the reaction system. And the photocatalytic degradation rate of MO is low if no H$_2$O$_2$ is involved. When H$_2$O$_2$ added into the reaction system at the beginning of light irradiation, both goethite nanorods synthesized from different routes showed high efficiency for photodegradation of MO. It is well known that the adsorption on the surface of catalyst of target molecules plays a key role in photocatalysis. MO molecules may adsorb on the surface of goethite by chelation of electron-donator groups with active sites of goethite, similar with that aminophenol on goethite surface.[25] The percentage of active sites of catalyst depends on the outer crystallographic facet. Therefore, the formation of one-dimensional structure of goethite may increase the active sites of surface and improve the catalytic performance. H$_2$O$_2$ can release intermediate radicals on goethite surface under UV-visible irradiation, as described in Equation 4.11. The improvement of degradation rate of methyl orange can thus be attributed to the direct oxidation of ≡Fe-MO complex on the surface of goethite nanorods under irradiation. This result is in agreement with the reported positive effect of H$_2$O$_2$ on photolysis of orange II by iron oxide.[38]

4.7 Conclusions

To probe the mechanism of photodegradation of methyl orange over illuminated iron oxide, the effects of catalyst dosage, solution pH, and initial concentration of MO, O$_2$ flow, as well as

hydrothermal synthesis conditions and morphology on their photoactivities were investigated. It was found that:

1. The photodegradation of MO over hematite follows a first order kinetics and can be described by L-H equation. There is an optimized catalyst dosage for slurry photo-catalytic reactions.

2. A saturation effect of photocatalytic reaction dependence on initial MO concentration was observed. This effect is caused by limited diffusion rate of MO molecules and photocatalytic radicals in the solution.

3. The photodegradation of MO is highly dependent on pH of solution, which can be ascribed to both surface hydroxyl radical configuration and structure conversion of MO molecule. Adding H_2O_2 as electron scavengers can increase the photocatalytic efficiency of both hematite and goethite.

4. Hydrothermal condition for synthesized hematite, including temperature and time duration has great influence on the oxidation efficiency of methyl orange on hematite nanoparticles. The influences are caused by crystallinity and surface structure. For faceted hematite, a high temperature and longer hydrothermal duration is unfavorable for their photocatalytic properties. And the photocatalytic performance is optimized at 140°C, 5 h for hematite synthesized with urea and 160°C, 5 h for using 3-aminopropanol as stabilizer.

Reference

[1] Albu, S. P.; Ghicov, A.; Macak, J. M.; Hahn, R.; Schmuki, P. *Nano Lett.* **2007**, *7*(5), 1286–1289.

[2] Tian, N.; Zhou, Z.-Y.; Sun, S.-G.; Ding, Y.; Wang, Z. L. *Science* **2007**, *316*(5825), 732–735.

[3] Xiong, Y.; Wiley, B. J.; Xia, Y. *Angew. Chem. Int. Ed.* **2007**, *46*, 7157–7159.

[4] Du, W.; Xu, Y.; Wang, Y. *Langmuir* **2008**, *24*, 175–181.

[5] Bandara, J.; Tennakone, K.; Kiwi, J. *Langmuir* **2001**, *17*, 3964–3969.

[6] Faust, B. C.; Hoffmann, M. R.; Bahnemann, D. W. *J. Phys. Chem.* **1989**, *93*, 6371–6381.

[7] Alfano, O. M.; Cabrera, M. I.; Cassano, A. E. *J. Catal.* **1997**, *172*(2), 370–379.

[8] Arrouvel, C.; Digne, M.; Breysse, M.; Toulhoat, H.; Raybaud, P. *J. Catal.* **2004**, *222*(1), 152–166.

[9] Barrón, V.; Torrent, J. *J. Colloid Interface Sci.* **1996**, *177*, 407–410.

[10] Gao, F.; Chen, X.; Yin, K.; Dong, S.; Ren, Z.; Yuan, F.; Yu, T.; Zou, Z.; Liu, J. M. *Adv. Mater.* **2007**, *19*(19), 2889–2892.

[11] Asahi, R.; Morikawa, T.; Ohwaki, T.; Aoki, K.; Taga, Y. *Science* **2001**, *293*, 269–271.

[12] Lindgren, T.; Wang, H.; Beermann, N.; Vayssieres, L.; Hagfeldt, A.; Lindquist, S. E. *Sol. Energy Mater. Sol. Cells* **2002**, *71*(2), 231–243.

[13] Kay, A.; Cesar, I.; Grätzel, M. *J. Am. Chem. Soc.* **2006**, *128*, 15714–15721.

[14] Yanina, S. V.; Rosso, K. M. *Science* **2008**, *320*, 218–222.

[15] Eggleston, C. *Science* **2008**, *320*, 184–185.

[16] Kuo, C.-H.; Chen, C.-H.; Huang, M. H. *Adv. Funct. Mater.* **2007**, *17*(18), 3773–3780.

[17] Khan, M. A.; Han, D. H.; Yang, O.-B. *Appl. Surf. Sci.* **2009**, *255*(6), 3687 – 3690.

[18] Duret, A.; Grätzel, M. *J. Phys. Chem. B* **2005**, *109*(36), 17184–17191.

[19] Pankove, J. I. *Optical Processes in Semiconductors;* Courier Dover Publications, 2 ed., 1975.

[20] Matsumoto, Y. November **1996**, *126*(2), 227–234.

[21] Yao, W. F.; Xu, X. H.; Wang, H.; Zhou, J. T.; Yang, X. N.; Zhang, Y.; Shang, S. X.; Huang, B. B. *Appl. Catal. B* **2004**, *52*(2), 109–116.

[22] Pan, G.; Liss, P. S. *J. Colloid Interface Sci.* **1998**, *201*(1), 71 – 76.

[23] Hoffmann, M. R.; Martin, S. T.; Choi, W.; Bahnemann, D. W. *Chem. Rev.* **1995**, *95*(1), 69–96.

[24] Houas, A.; Lachheb, H.; Ksibi, M.; Elaloui, E.; Guillard, C.; Herrmann, J.-M. *Appl. Catal. B* **2001**, *31*, 145–157.

[25] Andreozzi, R.; Caprio, V.; Marotta, R. *Water Res.* **2003**, *37*, 3682–3688.

[26] Li, Y.; Sun, S.; Ma, M.; Ouyang, Y.; Yan, W. *Chemical Engineering Journal* **2008**, *142*(2), 147 – 155.

[27] Turchi, C. S.; Ollis, D. F. *J. Catal.* **1990**, *122*(1), 178 – 192.

[28] Faust, B. C.; Hoffmann, M. R. *Environ. Sci. Technol.* **1986**, *20*(9), 943–948.

[29] Bandara, J.; Mielczarski, J.; Kiwi, J. *Langmuir* **1999**, *15*, 7670–7679.

[30] Bandara, J.; Mielczarski, J. A.; Lopez, A.; Kiwi, J. *Appl. Catal. B* **2001**, *34*, 321–333.

[31] Al-Qaradawi, S.; Salman, S. R. *J. Photochem. Photobiol. A* **2002**, *148*(1-3), 161–168.

[32] Pan, Z.; Somasundaran, P.; Turro, N. J.; Jockusch, S. *Colloids and Surfaces A: Physicochemical and Engineering Aspects* **2004**, *238*(1-3), 123 – 126.

[33] Hermanek, M.; Zboril, R.; Medrik, I.; Pechousek, J.; Gregor, C. *J. Am. Chem. Soc.* **2007**, *129*, 10929–10936.

[34] Herrera, F.; Lopez, A.; Mascolo, G.; Albers, P.; Kiwi, J. *Water Res.* **2001**, *35*, 750–760.

[35] Li, S.; Qin, G. W.; Pei, W.; Ren, Y.; Zhang, Y.; Esling, C.; Zuo, L. *J. Am. Ceram. Soc.* **2009**, *92*(3), 631–635.

[36] Nakamura, I.; Negishi, N.; Kutsuna, S.; Ihara, T.; Sugihara, S.; Takeuchi, K. *J. Mol. Catal. A: Chem.* **2000**, *161*(1-2), 205–212.

[37] Mills, A.; Le Hunte, S. *J. Photochem. Photobiol. A* **1997**, *108*(1), 1–35.

[38] Carp, O.; Huisman, C. L.; Reller, A. *Prog. Solid State Chem.* **2004**, *32*(1-2), 33–177.

[39] Beydoun, D.; Amal, R.; Low, G.; McEvoy, S. *J. Nanoparticle Res.* **1999**, *1*, 439–458.

[40] Li, S.; Zhang, Y.; Esling, C.; Muller, J.; Lecomte, J.-S.; Qin, G. W.; Zhao, X.; Zuo, L. *J. Appl. Cryst.* **2009**, *42*, 519–524.

[41] Huang, H.; Lu, M.; Chen, J. *Water Res.* **2001**, *35*, 2291–2299.

Chapter 5   Modified Iron Oxide Nanostructures

5.1   Introduction

Compared to TiO$_2$ or ZnO, iron oxide (α-Fe$_2$O$_3$) has the advantage that its band gap is ~2.1 eV, which lies in the visible region of solar spectrum and allows the absorption of roughly 40% of incident solar radiation. And it is stable against photo-corrosion in aqueous solution with proper pH.[45] Furthermore, combined with its suitable valence band position, large abundance, low cost, as well as environmental compatibility, hematite has attracted special scientific attention as a photocatalyst.[39] Thus attempts have been made to synthesize nanostructured hematite towards photocatalysts, in potential applications such as water splitting for H$_2$ generation [45, 76, 13] and catalytic oxidation of toxic organics.[5-41]

Despite the above seemingly advantages of hematite as a semiconductor material for photocatalyst purposes, the photocatalytic performance of illuminated hematite has been reported to be limited. For example, in photocatalytic water splitting investigations, the maximum experimental solar-to-chemical efficiency reported in the literature is less than 3% under AM 1.5 illumination.[45] The low efficiency was attributed to several reasons: (1) short life time of photo-induced minority carries of α-Fe$_2$O$_3$ causing high electron-hole recombination rates.[9] A diffusion length of the holes to only 2-4 nm has been reported, which is about 100 times lower than that of many other oxides,[10] demonstrating the poor charge charier transport characteristics of hematite. (2) Low electron mobility limiting the electron collection efficiency. The electron mobility in hematite is about 0.1 cm^{-2}V^{-1}s^{-1} .[45] (3) Anisotropic conductivity,[60] which is 4 orders magnitude higher within the (001) plane than parallel to [001].

On the other hand, from the viewpoint of band gap excitation, both oxidation and reduction reaction processes initiated by light irradiated metal oxide semiconductors occur on their surface. The overall quantum efficiency for interfacial charge transfer is determined by the competition between two processes, *i.e.*, the recombination of the photoactivated carriers and the interfacial charge transfer with the pre-adsorbed species. It was reported that up to 90% of the generated carriers are lost within a nanosecond of their photo-induced generation as a result of hole-electron pair recombination, leading to a low photoactivity of many metal oxide photocatalysts.[39, 10]

Therefore, in order to improve the photoactivity of the colloidal iron oxide particles, charge separation improvement and inhibition of charge carrier recombination are very advantageous to increase the overall quantum efficiency for interfacial charge transfer. Noble metal nanoparticle deposited on hematite is expected to fulfill the requirements by improving the charge separation under band gap excitation as a result of formation of a space-charge layer at the semiconductor-metal interface. In this chapter, we investigated the influence of Au and Ag nanoparticle loading on the photocatalytic activity of hematite nanoparticles.

For practical applications, the recovering of the photocatalysts is a major concern. The arrangement of the ordered nanorods array perpendicular to the substrate surface permits easy recovering of the photocatalyst and facile charge transfer from the interior of nanorod to the surface. Accordingly, a simple process was proposed to fabricate films of compact and aligned iron oxyhydroxide nanorod arrays grown on glass substrate. A seed layer was pre-coated on glass substrate by drop-coating and post thermal decomposition of ferric salt to drive the anisotropic growth of vertical nanorod arrays from the seed layer in aqueous solution. Effects of various growth parameters, such as seed density, growth time, as well as heat treatment temperature on the growth and alignment of the nanorods were investigated and optimized. The results showed that the seed layer played a critical role in fabrication the aligned nanorod arrays on glass substrate.

5.2   Effect of Noble Metal Loading on Hematite Photoactivity

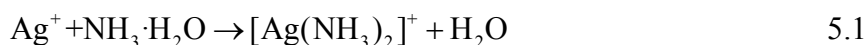## 5.2.1 Preparation of Au and Ag nanoparticles over hematite

(a) *loading Au nanoparticles by a glucose reduction method*

Au nanoparticles were deposited on surface of hematite according to method reported in literature,[13] in which β-D-glucose was used to reduce $HAuCl_4$ (99.9% in purity) in an alkaline solution. This process involves formation of gold through the reduction of $HAuCl_4$ and adhesions at the hematite surface. The molecules of β-D-glucose act as both reducing and capping agents. The deposition process is as follows:

1. Prepare 10 mM $HAuCl_4$ solution (0.0985 g in 25 mL of H_2O).
2. Add 20 mL of the 10 mM $HAuCl_4$ solution dropwise with vigorous stirring into 20 mL solution containing 2.20 g iron oxide.
3. Add β-D-glucose solution in water (0.05 M) dropwise with vigorous stirring until a color change from pale yellow to dark purple occurs (only the aqueous solution).
4. The powders are collected by centrifugation and washed several times and then dried in air at 50°C.

(b) *deposit Ag nanoparticle on hematite surface via a two-step method*

Silver mirror reaction has been known for many years to be a simple and convenient method to deposit the small and uniform-distributed spherical silver nanoparticles over semiconductors. Take the preparation of the 1.0 wt % Ag/α-Fe$_2$O$_3$ as an example: firstly, 0.0847 g AgNO$_3$ was dissolved in 5.0 g deionized water, and then 2.5% ammonia was added dropwise into the silver nitrate solution under vigorous shaking until the brown precipitation was dissolved again. Subsequently, 1.0 g of α-Fe$_2$O$_3$ was added into the silver-ammonia solution under stir for 20 min. And then 1.5 ml 5% glucose solution was added dropwise into the mixture and the stir was maintained for another 30 min. The reaction procedure is generalized into two main reactions as follows:

$$Ag^+ + NH_3 \cdot H_2O \rightarrow [Ag(NH_3)_2]^+ + H_2O \qquad 5.1$$

$$CH_2OH(CHOH)_4CHO + [Ag(NH_3)_2]^+ \xrightarrow{\Delta} CH_2OH(CHOH)_4COONH_4 + Ag + NH_3 + H_2O \quad 5.2$$

The metal-semiconductor nanocomposite was recovered by centrifugation, then washed with water and ethanol for three times to remove the residues on the surface, and finally then dried in an oven at 50°C.

(c) *one-pot synthesis of Ag-Fe$_2$O$_3$*

To investigate the influence of synthesis method on photocatalytic activity of nanocomposite, a one-pot hydrothermal synthesis method was used to prepare Ag-Fe$_2$O$_3$ nanocomposite. In a typical synthesis, 0.5061 g PEG 20k, 0.3605 g urea and 18 ml$\times$0.112 M iron (III) nitrate were added into 95 ml deionized water. After magnetically stirred for 15 min, 2 ml 0.02 M silver nitrate solution and subsequently 2 ml 5% glucose solution were added dropwise. The obtained mixture was stirred for another 20 min and sealed in Teflon-lined stainless steel autoclave, followed by successive thermal treatment at 160°C for 2 h. By doing so, an Ag-Fe$_2$O$_3$ nano-composite material was produced in one pot process. The theoretical Ag content in the nano-composite is 2.6 wt %.

5.2.2 Photocatalytic reaction evaluation

The photocatalytic activities of metal-loaded hematite were evaluated by measuring the photodegradation rate of methyl orange, a representative azo dye and also a common industrial pollutant which comes from textile industry. The illumination source was a 200 W high-pressure mercury lamp with the main emission at 365 nm. All the irradiation experiments were carried out in 250 mL beakers that were placed under the center of the light source and a magnetic stirrer was used to ensure the full suspension. The temperature of the beaker was

maintained at 20-25°C by water flow circuit. The reaction suspension was prepared by adding 0.050 g hematite powders into 100 mL MO solution (15 $mg \cdot L^{-1}$) and was stirred in dark for 30 min to set up the adsorption-desorption equilibrium. 3 mL of 1% H_2O_2 was added into the suspension just before the irradiation. At specific time intervals, a small quantity of the samples were withdrawn from the reaction system and centrifuged at 4000 $rpm \cdot min^{-1}$ for 5 min. The residual concentrations of MO in the solutions were determined by the light absorption at 464 nm, which were measured on a UV-vis spectrophotometer (Perkin-Elmer Lambda 750).

5.2.3 Results and discussion

Methyl orange was selected as a representative organic pollutant to evaluate the photocatalytic performance of the Ag (or Au) deposited hematite nanoparticles prepared from different routes. The decolorization process of methyl orange molecules was monitored by the UV-vis spectra. As an example, time dependent absorbance spectra of the MO dye solution are shown in Figure 5.1 in the presence of Ag 2.5 wt %/Fe_2O_3, Ag 2.6 wt %/Fe_2O_3, and hematite. The nanocomposite Ag 2.5 wt %/Fe_2O_3 was obtained by two-step method and the composite Ag 2.6 wt %/Fe_2O_3 was prepared by one-pot hydrothermal method, as described in the experimental
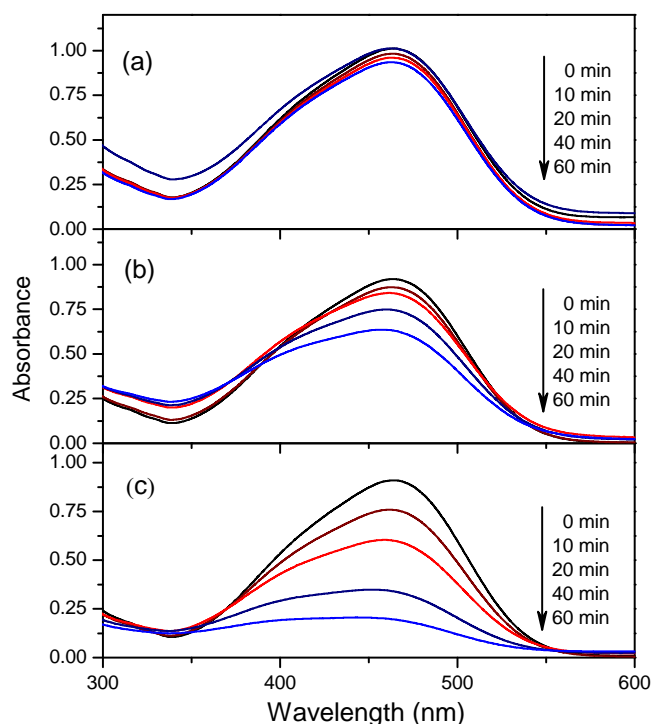
Figure 5.1 Comparison of the photodegradation of methyl orange at neutral pH in the presence of (a) Ag 2.5 wt %-Fe_2O_3 synthesized by two-step method; (b) Ag 2.6 wt %-Fe_2O_3 synthesized by one-pot method; (c) a-Fe_2O_3. The arrows indicate the direction of change of the absorbance as a result of photocatalytic reaction.
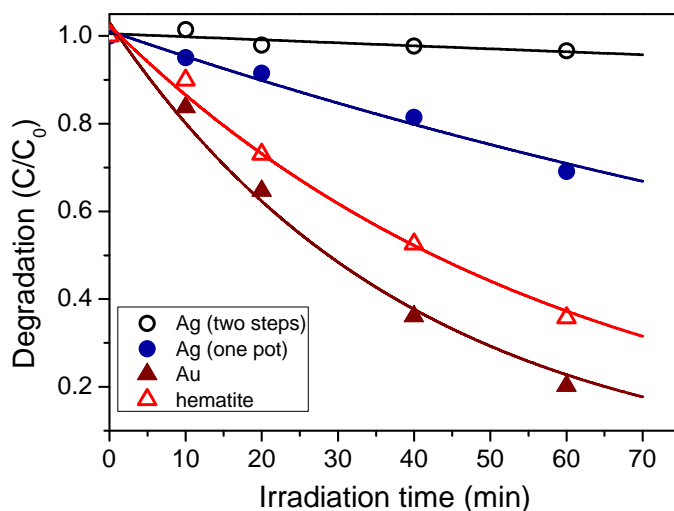
Figure 5.2 Extent of photodegradation of methyl orange molecules (monitored at 460 nm) as a function of the irradiation time for the Ag 2.5 wt %, Ag 2.6 wt %, Au nanoparticles loaded hematite nanocomposite and hematite.

section above. From Figure 5.1, one can see that the photocatalytic activity of hematite is deteriorated by loading Ag nanoparticles, and the extent is influenced by the synthesis method. As shown in Figure 5.3, the work function ϕ_m of Ag is 4.26 eV, which is lower than both the work function of hematite 5.4 eV[14] and the first electron affinity of hematite 4.71 eV.[15] Therefore, when Ag nanoparticles are in contact with hematite, electrons would migrate from Ag to hematite until a thermodynamic equilibrium is reached by forming the new Fermi energy.[65]

Under light irradiation, those imported electrons are inclined to combine with photogenerated holes, resulting in a decreased photocatalytic quantum efficiency of hematite. On the other hand, the coverage of metal nanoparticles on the surface of hematite decreases the illuminated area of the semiconductor. This is another unfavorable factor for photocatalytic activity. When Ag/Fe$_2$O$_3$ nanocomposite is prepared by one-pot hydrothermal synthesis method, some Ag particles are imbedded inside the hematite particle. In comparison, all Ag nanoparticles distribute on the surface of hematite when two-step synthesis method is applied. Thus, the difference in extent of photoactivity deterioration originates from the surface coverage percentage.

The photocatalytic experimental data can be converted into exponential pattern using a pseudofirst kinetics model and the results are shown in Figure 5.2. A photocatalytic reference, hematite without noble metal deposition was used to evaluate the activity of metal-semiconductor composites, qualitatively. It can be seen from Figure 5.2 that the photocatalytic performance of α-Fe$_2$O$_3$ can be improved by depositing an appropriate amount of Au nanoparticles, or be deteriorated by depositing Ag nanoparticles, regardless the preparation method. The positive effect of Au deposits is commonly regarded as a result of the fact that Au
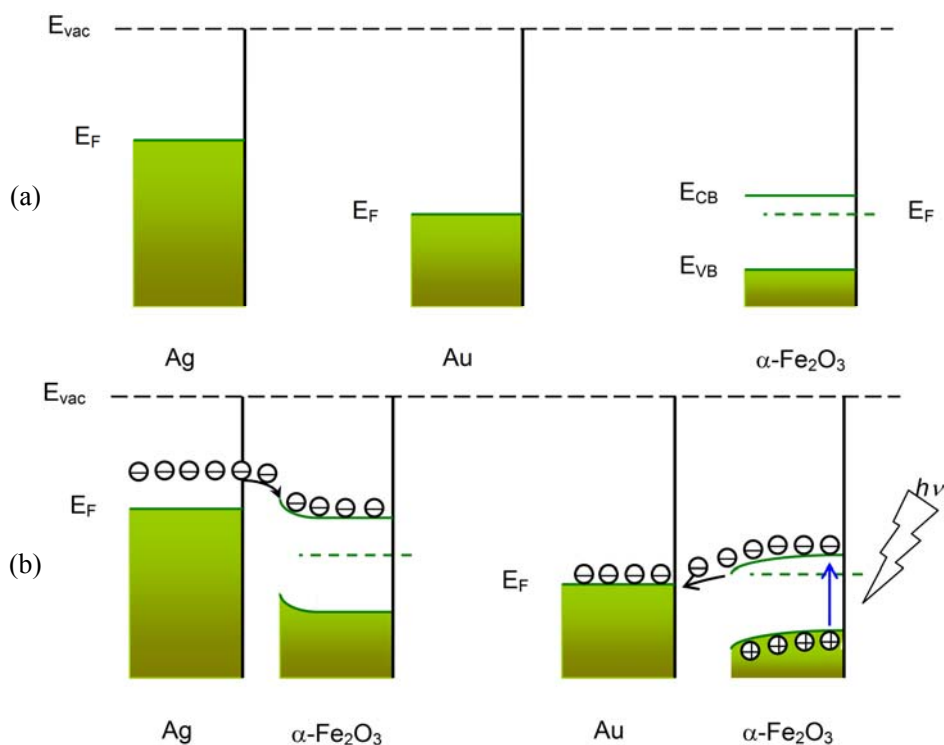
Figure 5.3 The band structure and Fermi energy level equilibrium of (a) Ag, Au and α-Fe$_2$O$_3$ and (b) their junctions. The Fermi energy level of α-Fe$_2$O$_3$ is lower than that of Ag and is higher than that of Au. (b) also gives the proposed charge separation process at the metal-semiconductor junction interface. Due to the Fermi energy level difference, the electrons are transferred from Ag to α-Fe$_2$O$_3$ until the two system setup equilibrium. And the photo-activated electrons flow from α-Fe$_2$O$_3$ to the metallic Au.

nanoparticles on the iron oxide surface behave like electron sinks, which provide sites for the accumulation of photogenerated electrons and then improve the separation of the photogenerated electrons and holes.[63, 62]

The different effects of Ag and Au deposits, *i.e.*, the positive effect of Au and negative of Ag nanoparticles, originate from the charge distribution between semiconductor and noble metal nanoparticles, which can be understood based on the proposed charged separation of Au/α-Fe$_2$O$_3$ and Ag/α-Fe$_2$O$_3$ under UV-visible light irradiation as shown in Figure 5.3. Although the work function ϕ_m of Au, which is 5.1 eV, is lower than that of hematite, the value is larger than the first electron affinity of hematite (4.71 eV[15]). Thus, the Fermi energy level of α-Fe$_2$O$_3$ is lower than that of Au because of the larger work function of hematite. Therefore, electrons would flow from Au to hematite.

However, the bottom of conduction band of hematite is higher than Fermi energy level of Au. This is a different point with that in case of Ag depositing. When Au/Fe$_2$O$_3$ is under illumination, the electrons are stimulated from valence band to conduction band of hematite and then transfer to contacting Au nanoparticles, as shown in Figure 5.3(b), until the two systems attain

the thermodynamic equilibrium. At this time, the two new Fermi levels are equal. The energy bands of hematite bend upward toward the surface. A space charge layer, so called "depletion region" is thus formed at the Au-Fe$_2$O$_3$ interface. In an ideal Schottky junction, the barrier height (ϕ_b) is the energy difference between the work function of the metal (ϕ_m) and the electron affinity of the semiconductor (ϕ_s):

$$\phi_b = \phi_m - \phi_s \qquad\qquad 5.3$$

Under the effect of Schottky barrier, the photogenerated electrons could migrate across the interface and initiate a reduction reaction at the Au particle surface, and thus the recombination is effectively suppressed. The photogenerated holes, on the other hand, are free to diffuse to the hematite surface and can initiate an oxidation of methyl orange molecules there. This electron transfer can greatly increase the charge separation and enhance the photocatalytic efficiency.

Furthermore, the electron accumulation (caused by charge flow from Au particle) within the hematite nanoparticles influences the position of the Fermi energy level that lies between the conduction and valance band. The Fermi energy level of an *n*-type semiconductor can be determined by:

$$E_F = E_{CB} + kT\ln\frac{n_{CB}}{N_{CB}} \qquad\qquad 5.4$$

in which E_{CB} is the conduction band bottom energy level, n_{CB} is the density of accumulated electrons, and N_{CB} is the effective density of conduction band states. From equation 5.4, one can see that the Fermi energy of hematite can shift toward the conduction band edge as a result of charge flow since the n_{CB} is always smaller than N_{CB}. For example, if we consider $N_{CB} \approx 10^{21}$ cm^{-3} in hematite* and $n_{CB} \approx 10^{17}$ cm^{-3}, then the potential difference between conduction band bottom and Fermi energy level $E_{CB} - E_F$ corresponds to 0.23 eV. And when Au/Fe$_2$O$_3$ nanocomposite is exposed to light irradiation, the electrons are excited by incident photons into the conduction band, which further increase n_{CB}. As a result, Fermi energy level of hematite shifts further.

5.3   Synthesis of Iron Oxide Nanorods Array

One-dimensional (1D) nanostructure materials, such as nanowires, nanorods, and nanotubes, have been shown to possess unique optical, catalytic and magnetic properties compared with their bulk form, and thus aroused great scientific interest.[13, 19-21] From viewpoint of practical

---

* According to *Landolt-Börnstein - Group III Condensed Matter*, Vol. 41, *pp* 1-6, the intrinsic carrier concentration inside hematite $n_i = 3.95\cdot10^{22}\exp(-1.8 eV/2kT)$ cm^{-3}.
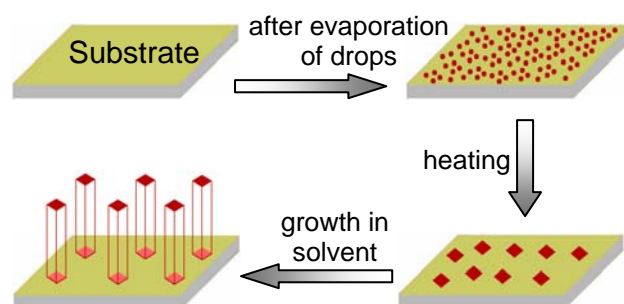
Figure 5.4 Schematic illustration of the procedure and possible growth mechanism for the synthesis of vertically aligned nanorod array of iron oxide on glass substrate.

applications, integrating nanowires and nanorods into devices requires theses 1D nanostructures to be grown on substrate to form vertically aligned arrays. In addition, films of ordered 1D nanostructure arrays show interesting magnetic properties[22] or improved quantum efficiency.[23-25] Particularly, 1D nanostructure arrays of iron (oxyhydr)oxide is receiving much attention due to their potential to serve as template to prepare arrays of metallic iron[26] and wide applications in solar cells, gas sensors, catalysts/photocatalysts, as well as cathodes for lithium-ion batteries.[27-30]

Direct thermal oxidation of iron foils[22, 31, 32] and metal-organic chemical vapor deposition process[33, 34] are two principal technologies to fabricate ordered aligned nanorod arrays of iron (oxyhydr)oxide. Although these approaches can produce aligned nanorod arrays but the density
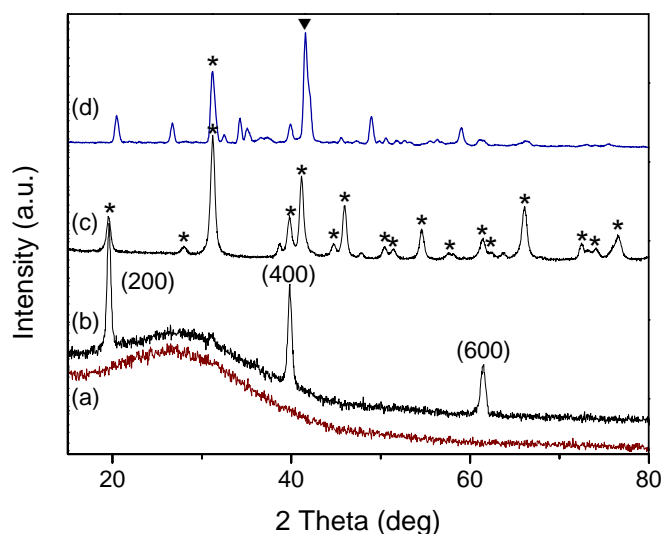
Figure 5.5 XRD patterns for (a) iron oxide seed layer; (b) β-FeOOH nanorod array film on glass substrate; (c) powders grown from ferric salts solution at 95°C for 10h; (d) products of iron acetate after heating at 250°C for 30 min. The asterisk (*) and triangle (▼) represent the phase of β-FeOOH and hematite, respectively.

is low, and high temperature and vacuum are required, making the technique energy consuming and complicated. Recently, Vayssieres L. proposed a low cost, moderate aqueous chemical route to produce transition metal oxide nanorods arrays.[92, 36] Using this method, films of ordered nanorod array of β-FeOOH, ZnO and α-Cr$_2$O$_3$ have been successfully grown by controlling the interfacial thermodynamics and kinetics of nucleation and growth on substrate. However, epitaxial substrate, such as α-Al$_2$O$_3$ or transparent conductive oxide, is required to reduce the interfacial tension and lattice mismatch. In this letter we describe a simple and efficient method to synthesize vertical nanorod arrays of iron oxyhydroxide in large area on glass substrate at relatively low temperature. An iron oxide thin layer obtained from thermal decomposition of drop-coating of ferric salt solvent on a glass substrate was served as seed layer to induce the anisotropic growth of iron oxyhydroxide from substrate.

5.3.1 Synthesis procedure

The detailed processes to grow β-FeOOH nanorod array on seeded substrate are as shown in Figure 5.4. First, iron salt was dissolved in ethanol (0.01 mol·L^{-1}) at room temperature. The cleaned glass surface was then wetted by a drop of the ferric acetate solution before rinsed with ethanol and dried in air. The above coating procedure was repeated for three times. Subsequently, the dried coated glass was heat treated at 250°C in air for 30 min to oxidize the iron acetate into iron oxide nanoclusters. After that, iron oxyhydroxide (β-FeOOH) nanorods films were grown on seeded glass by immerging the substrate in ferric chloride solution (0.10 mol·L^{-1}) at 95°C for 10 hours. Finally, the films were thoroughly washed with distilled water to eliminate residual salts, and were dried in air at 50°C. The fabrication procedure has been illustrated schematically.

5.3.2 Results and discussion

Figure 5.6(a) and 1(b) show typical SEM images of the as-synthesized nanorod array grown in solution on seeded glass substrate. The images reveal that a densely packed array of nanorods in large area was grown almost vertically on the substrate. The morphological parameters obtained from SEM images are the average diameter of the nanorods 70 nm, the nanorod length about 250 nm. Recently, the growth of vertically grown ZnO nanorod arrays has been demonstrated successfully in aqueous solution by using substrate with Zn metal seed layer[37] or textured ZnO seed layer [38]. Moreover, the same authors in Ref. [38] proposed that the anisotropic growth of ZnO may result from particular decomposition kinetics of zinc acetate, which was used to prepare the textured seed layer. Similarly, in our case, we believe that seed layer of iron
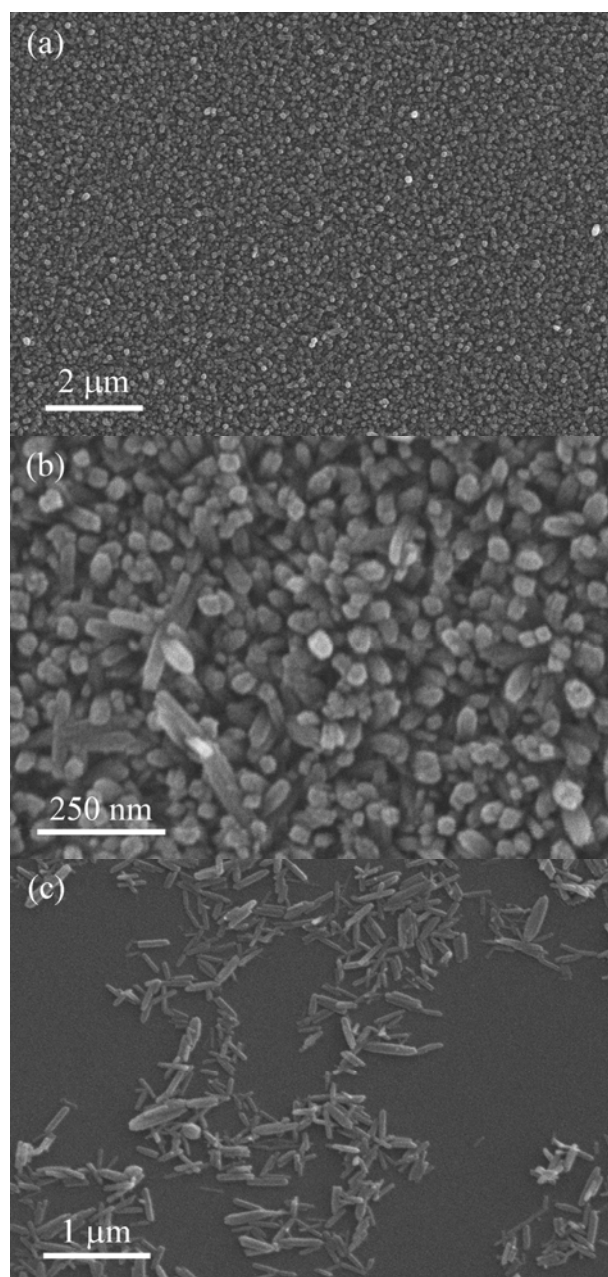
Figure 5.6 (a, b) low-magnification and high-magnification SEM images of the iron oxide array grew from an iron oxide seed layer on substrate; (c) SEM image of iron oxide nanorods grown on substrate without seed layer. The inset in (a) shows the cross-sectional SEM image of the same sample. All the nanorods were grown at 95°C for 10 h.

oxide synthesized from decomposition of iron acetate played critical role to induce the subsequent nucleation and anisotropic growth of β-FeOOH from the seed layer when the substrate was immersed into the reaction solvent. To make clear the role of the seed layer, glass plate without pre-coated seed layer was used as substrate to grow β-FeOOH in the same synthesis condition. As shown in Figure 5.6(c), no nanorod can grow vertically from substrate except some nanorods scatter on the surface of the substrate.
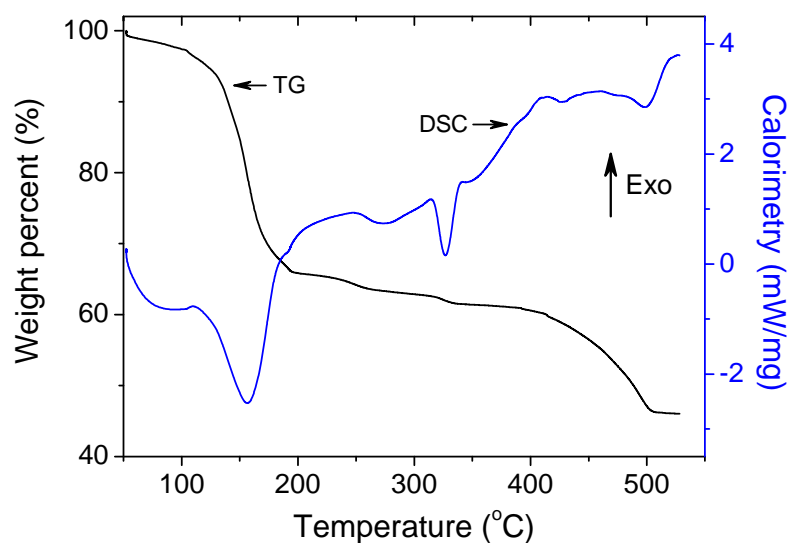
Figure 5.7 TG-DSC curves of iron salt (heating rate of 5°C·min^{-1}).

The crystalline structure of nanorods array sample was determined by XRD spectrum in Figure 5.5(b). As a reference, the XRD pattern of the corresponding powders produced in solution along with the growth of the nanorod array film was also given in Figure 5.5(c). All peaks in both spectra can be assigned as β-FeOOH. The XRD pattern of nanorod array with just three primary peaks at β-FeOOH (200), (400), and (600) suggests that the β-FeOOH (100) planes are oriented parallel to the basal plane of the glass substrate. These results indicate that the vertically aligned β-FeOOH nanorods were grown from the seed layer along [100] direction.

Seed layer of iron (oxyhydr)oxide were deposited on glass substrates via drop-coating and heating at 250°C for 10 min in air (in step c in Figure 5.4). The formation of the seed layer can be understood from thermal decomposition kinetics of ferric acetate. To achieve this, thermogravimetry-differential scanning calorimetry (TG-DSC) analysis of iron salt was performed. Thermal analysis of iron salt showed that the decomposition occurs at temperature above 160°C (Figure 5.7), which is 20°C lower than reported in literature.[39] As marked in Figure 5.5(d), XRD analysis of thermal decomposition products of ferric acetate at 250°C for 30 min indicates that the product sample is mainly composed of two crystalline phases: α-Fe$_2$O$_3$ and β-FeOOH (JCPDS card 73-603 and 34-1266). Some other minor peaks may be attributed to some iron oxide Fe$_x$O$_y$. XRD measurement was also carried out to characterize the seed layer on glass substrate. However, as shown in Figure 5.5(a), the seed layer was too thin for XRD measurement to detect any obvious peaks related to iron containing compounds.
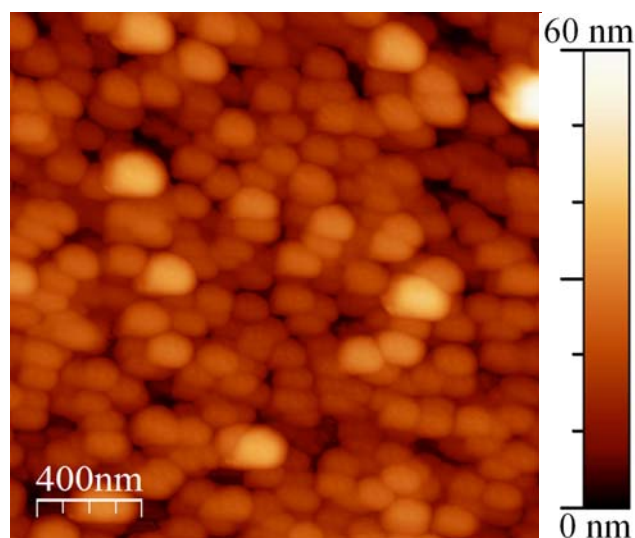
Figure 5.8. AFM image of iron oxide seed layer on glass substrate after heating at 250°C for 10 min.
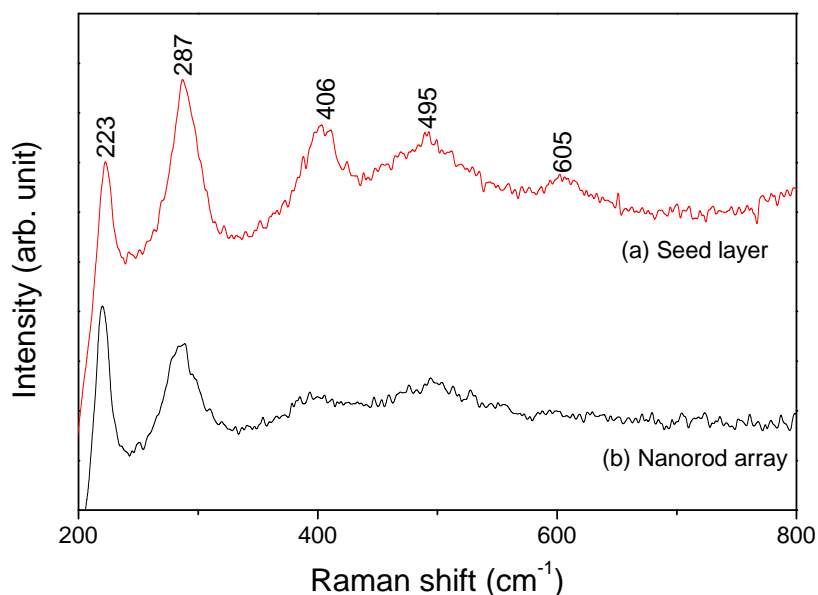

Figure 5.9. Raman spectra of films of (a) seed layer and (b) nanorod array on glass substrate.

Figure 5.8 shows a typical AFM image (processed with free software WSxM[©][40]) of the as-deposited seed layer on glass substrate, from which one can see that a layer of nanoparticles with average diameter of about 150 nm was formed after heating in air. In the framework of nucleation-growth theory, crystal growth can be promoted by providing nucleation sites with similar lattice match. In contrast to uncovered glass substrate, the seed layer can serve as nucleation sites for the growth of β-FeOOH nanorods by reducing the interface energy between the nucleus and the substrate. Furthermore, we speculate that the seed nanoparticle may have β-FeOOH (100) faces parallel to the basal plane of the substrate as a result of surface energy

minimization. Thus, these nanoparticle seeds can develop into 1D nanostructures by addition of soluble β-FeOOH species at the top of the nanorods along [100] directions.

5.4   Conclusion

In this chapter the iron oxide was modified by loading noble metals and fabricating nanorod arrays. The following conclusions have been reached.

The charge distribution between noble metal nanoparticles and semiconductor plays an important role in the photocatalytic activities of hematite. The distribution is determined by the comparison between the Fermi level of metals (Ag and Au) and hematite. If the Fermi level of the metal is higher than that of iron oxide, *e.g.*, in case of Ag deposit, charges flow from metal to semiconductor, forming a charge barrier at the junction interface and increasing the probability of carrier recombination. If the Fermi level of the metal is reduced below the Fermi level of the semiconductor, photogenerated charges would flow in the reverse direction, *i.e.*, from the conduction band to noble metals. The positive effect of Au deposit is the outcome of Schottky barrier formed at the Au-Fe_2O_3 interface.

A simple seeding-assisted aqueous solution method for producing films of densely aligned iron oxide nanorod arrays on glass substrate has been developed in this communication. Thin layer of iron oxide nanoparticles can be formed on substrate after evaporation and heating the glass wetted by iron salt solvent. Interestingly, structural characterization suggests that the phase of the film is different from that of corresponding powders as hydrolysis products of ferric slats in solution, resulting from epitaxial nucleation and anisotropic crystal growth from seed layer of iron oxide. Research on photocatalytic and other chemical properties of this iron oxide nanorods array is in progress.

Reference

[1] Kleiman-Shwarsctein, A.; Hu, Y.-S.; Forman, A. J.; Stucky, G. D.; McFarland, E. W. *J. Phys. Chem. C* **2008**, *112*, 15900–15907.

[2] Beydoun, D.; Amal, R.; Low, G.; McEvoy, S. *J. Nanoparticle Res.* **1999**, *1*, 439–458.

[3] Duret, A.; Grätzel, M. *J. Phys. Chem. B* **2005**, *109*(36), 17184–17191.

[4] Kay, A.; Cesar, I.; Grätzel, M. *J. Am. Chem. Soc.* **2006**, *128*, 15714–15721.

[5] Li, F. B.; Li, X. Z.; Li, X. M.; Liu, T. X.; Dong, J. *J. Colloid Interface Sci.* **2007**, *311*, 481–490.

[6] Du, W.; Xu, Y.; Wang, Y. *Langmuir* **2008**, *24*, 175–181.

[7] Wang, Y.; Du, W.; Xu, Y. *Langmuir* **2009**, *25*, 2895–2899.

[8] Yamada, K.-i.; Mukaihata, N.; Kawahara, T.; Tada, H. *Langmuir* **2007**, *23*, 8593–8596.

[9] Cherepy, N.; Liston, D.; Lovejoy, J.; Deng, H.; Zhang, J. *J. Phys. Chem. B* **1998**, *102*, 770–776.

[10] Kennedy, J. H.; Karl W. Frese, J. *J. Electrochem. Soc.* **1978**, *125*, 709–714.

[11] Yanina, S. V.; Rosso, K. M. *Science* **2008**, *320*, 218–222.

[12] Alfano, O. M.; Cabrera, M. I.; Cassano, A. E. *J. Catal.* **1997**, *172*(2), 370–379.

[13] Qin, G. W.; Liu, J.; Balaji, T.; Xu, X.; Matsunaga, H.; Hakuta, Y.; Zuo, L.; Raveendran, P. *J. Phys. Chem. C* **2008**, *112*(28), 10352–10358.

[14] Lide, D. R. *CRC Handbook of Chemistry and Physics, 88th Edition;* CRC, 2007.

[15] Watanabe, A.; Kozuka, H. *J. Phys. Chem. B* **2003**, *107*(46), 12713–12720.

[16] Hirakawa, T.; Kamat, P. V. *J. Am. Chem. Soc.* **2005**, *127*(11), 3928–3934.

[17] Jakob, M.; Levanon, H.; Kamat, P. V. *Nano Lett.* **2003**, *3*(3), 353–358.

[18] Lu, W.; Liu, G.; Gao, S.; Xing, S.; Wang, J. *Nanotechnology* **2008**, *19*(44), 445711.

[19] Murphy, C. J.; Sau, T. K.; Gole, A. M.; Orendorff, C. J.; Gao, J.; Gou, L.; Hunyadi, S. E.; Li, T. *J. Phys. Chem. B* **2005**, *109*(29), 13857–13870.

[20] Sun, L.; Hao, Y.; Chien, C.-L.; Searson, P. C. *IBM J. Res. Dev.* **2005**, *49*, 79–102.

[21] Zhou, K.; Wang, X.; Sun, X.; Peng, Q.; Li, Y. *J. Catal.* **2005**, *229*(1), 206–212.

[22] Kim, C. H.; Chun, H. J.; Kim, D. S.; Kim, S. Y.; Park, J.; Moon, J. Y.; Lee, G.; Yoon, J.; Jo, Y.; Jung, M. H.; Jung, S. I.; Lee, C. J. *Appl. Phys. Lett.* **2006**, *89*(22), 223103.

[23] Feng, X.; Shankar, K.; Varghese, O. K.; Paulose, M.; Latempa, T. J.; Grimes, C. A. *Nano Lett.* **2008**, *8*, 3781–3786.

[24] Vayssieres, L.; Sathe, C.; Butorin, S. M.; Shuh, D. K.; Nordgren, J.; Guo, J. *Adv. Mater.* **2005**, *17*(19), 2320–2323.

[25] Wang, W.; Lin, H.; Li, J.; Wang, N. *J. Am. Ceram. Soc.* **2008**, *91*(2), 628–631.

[26] Vayssieres, L.; Rabenberg, L.; Manthiram, A. *Nano Lett.* **2002**, *2*(12), 1393–1395.

[27] Gapin, A. I.; Ye, X.-R.; Chen, L.-H.; Hong, D.; Jin, S. *IEEE T. Magn.* **2007**, *43*(6), 2151–2153.

[28] Hwang, S. O.; Kim, C. H.; Myung, Y.; Park, S.-H.; Park, J.; Kim, J.; Han, C.-S.; Kim, J.-Y. *J. Phys. Chem. C* **2008**, *112*, 13911–13916.

[29] Lindgren, T.; Wang, H.; Beermann, N.; Vayssieres, L.; Hagfeldt, A.; Lindquist, S. E. *Sol. Energy Mater. Sol. Cells* **2002**, *71*(2), 231–243.

[30] Poizot, P.; Laruelle, S.; Grugeon, S.; Dupont, L.; Tarascon, J.-M. *Nature* **2000**, *407*(6803), 496–499.

[31] Cvelbar, U.; Chen, Z.; Sunkara, M. K.; Mozetic, M. *Small* **2008**, *4*(10), 1610–1614.

[32] Wen, X. G.; Wang, S. H.; Ding, Y.; Wang, Z. L.; Yang, S. H. *J. Phys. Chem. B* **2005**, *109*(1), 215–220.

[33] Cha, H. G.; Kim, C. W.; Kim, Y. H.; Jung, M. H.; Ji, E. S.; Das, B. K.; Kim, J. C.; Kang, Y. S. *Thin Solid Films* **2008**, *517*, 1853–1856.

[34] Wu, J.-J.; Lee, Y.-L.; Chiang, H.-H.; Wong, D. K.-P. *J. Phys. Chem. B* **2006**, *110*(37), 18108–18111.

[35] Vayssieres, L. *Int. J. Nanotechnol.* **2004**, *1*(1), 1–41.

[36] Vayssieres, L.; Beermann, N.; Lindquist, S.-E.; Hagfeldt, A. *Chem. Mater.* **2001**, *13*(2), 233–235.

[37] Tak, Y.; Yong, K. *J. Phys. Chem. B* **2005**, *109*(41), 19263–19269.

[38] Greene, L. E.; Law, M.; Tan, D. H.; Montano, M.; Goldberger, J.; Somorjai, G.; Yang, P. *Nano Lett.* **2005**, *5*(7), 1231–1236.

[39] Jewur, S. S.; Kuriacose, J. C. *Thermochim. Acta* **1977**, *19*, 195–200.

[40] Horcas, I.; Fernández, R.; Gómez-Rodrguez, J. M.; Colchero, J.; Gómez-Herrero, J.; Baro, A. M. *Rev. Sci. Instrum.* **2007**, *78*(1), 013705.

Chapter 6   General Conclusions and Perspectives

Growing environmental concerns and increasing energy demands stimulate the research work in the field of photocatalysis. TiO_2 takes the central role in the development of photocatalyst. However, its several deficiencies restrict the wide applications. Although much modification work has been done, the improvement is limited. An alternative approach is to start with a material that has an intrinsically small bandgap. Iron oxide, fulfilling almost all the requirements as a good photocatalyst, becomes a potential candidate material. The objective of this dissertation is to develop and characterize iron oxide photocatalyst which is highly responsive to visible light. Special efforts have been made on the fabrication and characterization of iron oxide based nanostructures to achieve better photocatalytic properties for environmental remediation. The main conclusions drawn from this work are as follows.

6.1   Hydrothermal Synthesis of Iron Oxide with Different Morphologies

The ability to control the physical and chemical properties of inorganic nanocrystals *via* the overall control of their size and shape is of special importance. Hydrothermal methods, based on the use of simple organic molecules with different end-functional groups as capping agents, have been applied to synthesize the iron oxide of different polymorphs with tailored size and shape. The tuning of the chemistry at crystal-solution interface allows for the control of the size and the shape of iron oxide. In terms of chemical environment dependence of nanoparticle morphology, the results show that the interaction anisotropy between the functional group with different electronnegativity and the iron oxide facets plays a critical role. Due to the capability difference of capping agents and crystallographic planes of iron oxide, the growth competition among different planes could be changed.

Specifically, three representative molecules with different functional group of –NH_2, –OH, and =O were used as capping agents in synthesizing α-Fe_2O_3, Fe_3O_4, and α-FeOOH nanostructures. It was found that chelating between N atoms and iron cations on iron oxide surface promotes the growth of hematite into plate-like shape and confines the growth of Fe_3O_4 in all directions. Assisted by the N-Fe chelating, urea molecules adsorb symmetrically on crystal surface of α-Fe_2O_3, resulting in a polyhedral shape of hematite. For magnetite growth in the presence of urea, the shape of nanocrystals evolves from ellipsoidal into faceted (with more {111} planes exposed) with the prolonged hydrothermal duration. Due to the long chain

structure, PEG molecules are inclined to interact with each other to form 'cages templates' instead of to adsorb on the surface of iron oxides. Thus the growth of iron oxide nanoparticles could be confined by the cage templates. Through experimentation and characterization, a terrance-kink-step growth mechanism for these faceted nanostructures has been developed.

Nanorods of goethite have been grown by oriented aggregation from two wet chemical routes. Experimental results show that the existing Fe^{2+} cations in the reaction medium only have an acceleration effect on the first step of formation process of goethite, *i.e.*, the dissolution of ferrihydrite. BFDH calculation reveals that the anisotropic growth of goethite is intrinsic.

The development of size and shape control of iron oxide nanocrystals offers new ways to overcome fundamental barriers to the use of nanocrystals in applications, such as magnetic devices, electromagnetic therapy and catalysis.

6.2 Surface Crystallography Characterization of Faceted Nanoparticles

For faceted nanoparticles enclosed by specific crystallographic facets, the morphology is defined by the crystallographic planes of the surface. Also, chemical and catalytic properties could benefit from the synthesis of nanostructured materials not only through the preparation of nanoparticles with high surface to volume ratio and narrow size distribution, but also through the possibility to produce nanoparticle with well defined morphology and specified surface crystallography. Indeed, the precise characterization of surface index of faceted nanoparticles is of great importance. In this work we present a general TEM method that can be applied to determine the crystallographic plane of the surface of faceted nanoparticles without requiring the rigorous plane-on edge condition for the diffraction pattern, provided that the edges of the facets are visible under TEM imaging mode.

The core of the method is to determine the coordinates of the edges vectors in the TEM screen coordinate system. The orientation of the particle with respect to the sample holder is determined by acquiring and indexing the corresponding diffraction pattern (Spot or Kikuchi line pattern). The Miller indices of the surface planes and edges of the particle are calculated through coordinate transformation from the screen coordinate system to the crystal coordinate system. To illustrate the feasibility of the proposed method, the hydrothermally synthesized hematite was characterized by applying the technique, demonstrating that the method offers a general and systematic way of characterizing the surface crystallographic features of a nanoparticle and will facilitate the related studies in nanoscience.

6.3   Photocatalytic Activity of Iron Oxide Nanostructures

The iron oxide nanoparticles prepared in this work, mainly hematite and goethite have been exploited in the photocatalytic degradation of azo dye methyl orange as a model contaminant. An extensive study of the effect of the initial dye concentration, catalyst dosage, pH of the solution, as well as electron scavenger agents has been carried out. The photocatalytic activities of hematite samples synthesized under different hydrothermal conditions have also been investigated. Kinetics investigation of photodegradation MO showed that the reaction follows a first order equation and can be described by Langmuir-Hinshelwood equation.

A saturation effect of photocatalytic reaction on the initial methyl orange concentration was observed. The saturation effect was ascribed to the competition and equilibrium between the charge transfer process from hematite or photocatalytic radicals to methyl orange molecules and the process of MO molecule or radicals diffusion in the reaction solution. At higher concentrations, the diffusion rate of dye molecules and the probability of radical attacks increases, leading to more molecules oxidized in the unit time intervals.

The pH value is an important factor to affect the photodegradation of methyl orange, which is mostly caused by the structure conversion between the quinonoid form and alkaline azo formula at pH of 3.4. Due to the inclined decomposition of quinonoid form of methyl orange, the photocatalytic reaction is accelerated greatly at low pH. On the other hand, the surface hydroxylation could be induced by increasing the pH of the solution. The process is in favor of the photocatalytic reactions since the hydroxyl radical is the primary species that can capture the photogenerated carriers and initiate a redox reaction. Besides, the positive effects of oxygen flow or adding hydrogen peroxide on the photocatalytic efficiency of hematite were demonstrated. The effects were ascribed to the formation of hydroxyl radicals from H_2O_2 by capturing the photogenerated charge carriers.

The oxidation efficiency of methyl orange on as-synthesized faceted hematite nanoparticles was corresponding to the hydrothermal conditions, including temperature and time duration, suggesting a guideline on optimizing the photocatalytic activities of hematite. The influences are caused by crystallinity and surface structure. For both polyhedron and plate-like hematite nanoparticles fabricated with respective urea and 3-aminopropanol as stabilizer, a high temperature and longer hydrothermal duration is unfavorable for their photocatalytic properties. The photocatalytic performance is optimized at 140°C for 5 h with urea and 160°C for 5 h with 3-aminopropanol as stabilizer.

Based on the above experimental results, a semiconductor photocatalysis mechanism has been proposed to explain the degradation of the methyl orange on illuminated hematite. The mechanism of ligand-to-metal charge transfer (LMCT) within a surface complex has thus been excluded. The photodegradation process starts with photo-induced charge excitation, then the charge carriers transport to the hematite surface and finally the charges are captured by the surface where the redox reactions are initiated. Besides the reductive decolorization of azo dyes, a variety of organic compounds can be expanded to be mineralized by light irradiated iron oxide, demonstrating potential applications in the treatment of textile dye wastes and drainage water.

6.4   Noble Metal Loading of Hematite and Synthesis of Arrays

Despite of the advantages of iron oxide as a promising candidate for photocatalyst, the photocatalytic reaction efficiency is not high, especially compared with that of TiO_2 and/or ZnO. An attractive technique for optimizing the photocatalytic activity of iron oxide nanoparticles has been proposed. Two wet chemical routes, *i.e.*, post-treatment of hematite by reducing method or one-pot hydrothermal method, have been used to prepare the noble metal-Fe_2O_3 nanocomposite system. Au and Ag nanoparticles having different work function were deposited on the hematite surface. It was proposed that the charge carrier distribution between the noble metal nanoparticles and hematite plays an important role in the photocatalytic activities of hematite. This technique is potentially extendable to the deposit of other metals (or semiconductors and organic molecules) with larger work function.

Synthesis research for achieving aligned, densely packed one-dimensional nanorod arrays are desired due to the various advantages of the patterned structure, especially due to its improved charge transport features when adopted to the development of energy conversion applications. The growth of iron oxide on glass substrate is difficult. So far the arrays of iron oxide are grown using epitaxial technique. This technique is currently limited to expensive substrates or requires gas-phase preparation of the seed layer. In this work, a simple wet chemical route to synthesis arrays of iron oxide nanorods on glass substrate is worked out. By forming layers of aligned ZnO nanocrystals *in situ* on a flat substrate by thermal decomposing the iron salts, the growth of vertical iron oxide nanorod arrays could be directed when the substrate is immersed into the ferric solutions.

In addition, the fabricated iron oxide has a strong axial texture. The nanorods are inclined to oriented with the (200) plane parallel to the substrate. The preferred growth inherits from the seed nanoparticles, which may have (100) faces parallel to the basal plane of the substrate as a result of surface energy minimization. When iron oxide works as photocatalysts, one of trou-

blesome issue is the recovery of the photocatalyst. By fixing the iron oxide on substrate, the proposed method provides a solution for dealing the difficulty of recovery.

6.5   Perspectives

There are many possible ways to continue the work based on the research presented here. One way includes the expansion of the demonstrated shape control of iron oxide nanoparticles to other oxide materials by adopting similar molecules as capping agent in the hydrothermal synthesis. This will enable the exploitation of various oxide nanostructures for applications such as catalysis, gas sensors and biotechnology. The TEM characterization method for determining the precise shape of a faceted nanoparticle provides a facility for many structure-property investigations, especially for surface-related properties, such as catalytic, gas sensing. Methyl orange molecules were used as a model contaminant; actually the target can be expanded to many other organic pollutant molecules, in particular, the many wastes in underground water for deep purification of drinking water. Further studies in this direction would be in favor of the environmental remediation. Another area that iron oxide nanostructures can be applied is working as photoanode for harvesting solar energy in the field of photovoltaic and water splitting for hydrogen generation, if the iron oxide nanoparticles of various morphologies are incorporated with conducting glass in the form of film. Our proposed simple method for fabricating iron oxide nanorod arrays opens an avenue for the research. Besides, the arrays synthesis method can be easily applied to other metal oxide, for example, WO_3, ZnO etc. Researches in all of these areas will be important in advancing the field of nanoscience and light power harvesting.

Acknowledgment